

The fabrication and characterisation of nanoscale patterns
on surfaces

Maria-Victoria Meli

Department of Chemistry
McGill University
Montréal, Québec H3A 2K6
Canada

A thesis submitted to McGill University in partial fulfillment of the requirements of
the degree of

Doctor of Philosophy

September 2005

© Maria-Victoria Meli 2005



Library and
Archives Canada

Bibliothèque et
Archives Canada

Published Heritage
Branch

Direction du
Patrimoine de l'édition

395 Wellington Street
Ottawa ON K1A 0N4
Canada

395, rue Wellington
Ottawa ON K1A 0N4
Canada

Your file *Votre référence*
ISBN: 978-0-494-21675-0
Our file *Notre référence*
ISBN: 978-0-494-21675-0

NOTICE:

The author has granted a non-exclusive license allowing Library and Archives Canada to reproduce, publish, archive, preserve, conserve, communicate to the public by telecommunication or on the Internet, loan, distribute and sell theses worldwide, for commercial or non-commercial purposes, in microform, paper, electronic and/or any other formats.

The author retains copyright ownership and moral rights in this thesis. Neither the thesis nor substantial extracts from it may be printed or otherwise reproduced without the author's permission.

AVIS:

L'auteur a accordé une licence non exclusive permettant à la Bibliothèque et Archives Canada de reproduire, publier, archiver, sauvegarder, conserver, transmettre au public par télécommunication ou par l'Internet, prêter, distribuer et vendre des thèses partout dans le monde, à des fins commerciales ou autres, sur support microforme, papier, électronique et/ou autres formats.

L'auteur conserve la propriété du droit d'auteur et des droits moraux qui protègent cette thèse. Ni la thèse ni des extraits substantiels de celle-ci ne doivent être imprimés ou autrement reproduits sans son autorisation.

In compliance with the Canadian Privacy Act some supporting forms may have been removed from this thesis.

Conformément à la loi canadienne sur la protection de la vie privée, quelques formulaires secondaires ont été enlevés de cette thèse.

While these forms may be included in the document page count, their removal does not represent any loss of content from the thesis.

Bien que ces formulaires aient inclus dans la pagination, il n'y aura aucun contenu manquant.


Canada

Abstract

Nanopatterning is the fabrication of topologically and chemically patterned surfaces, with structural parameters < 100 nm. It is a topic of great interest given the demand in applying nanoscience and nanotechnology in the next generation of electronic and optical devices, and catalysts. To this end, novel bottom-up strategies hold the most promise to this end for creating a great variety of morphologies in a parallel manner.

This Thesis is centered on the development of new methodologies for creating nanopatterned surfaces, and their characterization in light of possible applications. A symmetric, amphiphilic diblock copolymer, polystyrene-*b*-poly(2-vinylpyridine) was self-assembled at the air-water interface to create an array of surface micelles. The Langmuir-Blodgett technique was used to transfer continuous films of ordered surface micelles to different substrates to be used as a sacrificial mask. Argon ion-milling of the block copolymer-coated substrates resulted in the high-fidelity pattern transfer of the topological features in the case of Au, Si/SiO_x, and SiO₂ substrates, and the generation of Au island arrays in the case of Si/SiO_x, mica and quartz substrates coated with thin (10-20 nm) Au films. The wetting of water on the resulting nanopatterned surfaces was determined to be conformal (Wenzel-type) and the transition to non-conformal (Cassie-type) wetting is described. The extinction of light by the gold island arrays was measured and compared to calculations made using the quasistatic approximation to Mie theory. The response of the localized surface plasmon resonance of these arrays to alkylthiol adsorption and changes in the surrounding medium refractive index was measured and discussed with respect to creating a sensing scheme.

Résumé

La fabrication de surfaces, topologiquement et chimiquement modelées, dont les paramètres structuraux sont <100 nm, est un sujet de grand intérêt étant donné la demande d'application des nanosciences et des nanotechnologies pour la prochaine génération de dispositifs électroniques et optiques, et des catalyseurs. Dans ce but, les nouvelles approches ascendantes tiennent le plus de promesses pour réaliser une grande variété de nanostructures d'une manière alternative et parallèle.

Cette Thèse est centrée sur le développement de nouvelles méthodologies permettant de créer des surfaces modelées à l'échelle nanométrique, ainsi que sur leur caractérisation, en tenant compte de leurs applications possibles. Un copolymère bloc, symétrique et amphiphile, de polystyrène-b-poly(2-vinylpyridine) a été auto-assemblé à l'interface air/eau pour créer une matrice de micelles de surface. La technique de Langmuir-Blodgett a été utilisée pour transférer des couches minces de ces micelles ordonnées sur différents substrats, afin d'être utilisées comme un masque pour la lithographie. La gravure ionique à l'argon de ces substrats permet un transfert de grande fidélité des motifs sur des surfaces d'or, de Si/SiO_x, et de SiO₂, ainsi que la génération d'une matrice de nanoparticules d'or dans le cas des substrats de Si/SiO_x, du mica et du quartz revêtus de couches minces d'or (10-20 nm).

Le mouillage de l'eau sur les surfaces modelées a été déterminé conforme (comme le modèle de Wenzel), et la transition de mouillage non-conforme (comme le modèle de Cassie) est décrite. L'extinction de lumière par les matrices de nanoparticules d'or a été mesurée et a été comparée aux calculs utilisant la théorie de Mie. La réponse de la résonance plasmon de surface de ces nanoparticules à l'adsorption d'une couche monomoléculaire d'alkylthiol, ainsi que les changements de l'indice de réfraction, a été mesuré et a été discuté en vue de la création d'un capteur chimique.

Foreword

This dissertation is written in the form of two published papers and two thesis chapters. The two thesis chapters will be submitted shortly to peer-refereed journals. The papers each comprise one chapter in the main body of the Thesis (Chapters 2 and 3), with Chapters 4 and 5 comprising the remaining body of the Thesis. A general introduction to this work is provided in Chapter 1, and conclusions to the work are provided in Chapter 6. The papers have been published in the following scientific journals:

Chapter 2: Self-Assembled Masks for the Transfer of Nanometer-Scale Patterns into Surfaces: Characterization by AFM and LFM
co-authored by A. Badia, P. Grütter, and R. Bruce Lennox
Nano Letters 2002 2, 131-135.

Chapter 3: Preparation of Nanoscale Au Islands in Patterned Arrays
co-authored by R. Bruce Lennox
Langmuir 2003 19, 90-97.

In accordance with guideline C of the “Thesis Preparation and Submission Guidelines” (Faculty of Graduate Studies and Research), these Chapters are logically linked into a cohesive unit using connecting texts. Furthermore, supplementary information relevant to the papers (Chapters 1 and 2) is provided in Appendix 1 and 2. The contribution of all co-authors to the papers is described along with signed waivers for copyright clearance from the co-authors.

Since both papers have been published by the American Chemical Society (ACS), and the ACS provides blanket permission to students to include the text of their papers in their thesis (see cited text below), a credit line is provided on the first page of the respective articles, in accordance with the “ACS Publications Division Guidelines”.

Contribution of Authors

The two papers were both co-authored by the research director, Professor R. Bruce Lennox. Chapter 2 also includes A. Badia and P. Grütter as co-authors. Dr. A. Badia performed the initial studies of pattern transfer of the block copolymer pattern as a postdoctoral fellow in collaboration with Drs. P. Grütter and R. B. Lennox. Ideas and results generated from that work initiated the work shown in the later paper (*Nano Letters* 2002). Dr. P. Grütter provided expertise in the acquisition and interpretation of lateral force microscopy images. Other than the supervision, advice and direction of Dr. Lennox and the support mentioned above, all of the work presented in the dissertation was performed by the author.

I hereby give copyright clearance for the inclusion of the following papers, of which I am co-author, in the dissertation of Maria-Victoria Meli

"Self-Assembled Masks for the Transfer of Nanometer-Scale Patterns into Surfaces: Characterization by AFM and LFM"
Published in *Nano Letters* 2002 2, 131-135.

and

"Preparation of Nanoscale Au Islands in Patterned Arrays"
Published in *Langmuir* 2003 19, 90-97.

Date: June 27, 2005

Dr. R. Bruce Lennox
McGill University

I hereby give copyright clearance for the inclusion of the following paper, of which I am co-author, in the dissertation of Maria-Victoria Meli

"Self-Assembled Masks for the Transfer of Nanometer-Scale Patterns into Surfaces: Characterization by AFM and LFM"

Published in *Nano Letters* 2002 2, 131-135.

Date: 29/06/2005

Dr. A. Badia

Université de Montréal

I hereby give copyright clearance for the inclusion of the following paper, of which I am co-author, in the dissertation of Maria-Victoria Meli

"Self-Assembled Masks for the Transfer of Nanometer-Scale Patterns into Surfaces: Characterization by AFM and LFM"
Published in *Nano Letters* 2002 2, 131-135.

Date: 17-6-2005

Dr. P. Grütter
McGill University

Acknowledgments

I would like to express my gratitude to a number of people who have contributed to this Thesis and my graduate student experience in a positive way.

First, I must sincerely thank my research supervisor, Prof. Bruce Lennox, for his supervision and guidance throughout. His creativity, confidence, and infinite patience have inspired me to take some scientific “risks” and to grow as both a person and researcher. Most importantly, he has always allowed and encouraged me to explore interests outside of the immediate scope of my thesis work, by recognizing their value in my whole education. His unselfish attitude has enabled me to explore new avenues that too easily would have never been possible.

I must also thank Prof. Antonella Badia for her boundless energy, and positive attitude which initially hooked me onto research. Her selfless support gave me the most important tools for doing research: passion, technical expertise, self-confidence, and a strong work ethic. I am especially grateful for the pep-talks and good advice, and for always feeling welcome at her lab in the UdeM.

I would also like to thank Prof. Peter Grütter for his great enthusiasm, support, and many useful discussions. I often felt that I had a “second home” in his lab, and I thank him for enabling that level of interaction.

Very warm thanks belong with the members of the Lennox lab and the Grütter lab (past and present), particularly Carl Bartels, Ian Burgess, Valérie Gandubert, Adil Kassam, Brian Seivewright, and Ben Smith, who through

many useful discussions and their colourful personalities have contributed to my learning and enjoyment of research. I would like to give special thanks to Adil Kassam who has significantly improved all things computer-related in the lab and has even managed to make me a little computer-literate; to Brian Seivewright and Ian Burgess who have come to my aid when instruments need fixing; to Gilles Bourret for help with the French translation of the Thesis Abstract; and to Louis Cuccia and Carl Bartels for helpful discussions and for proofreading parts of this Thesis.

Big thanks are due to the people who always make things run smoothly yet sometimes go unrecognized: Robert Gagnon (McGill Center for the Physics of Materials) for the preparation of sputtered gold films, S. Kelly Sears and Helen Campbell for advice and helpfulness in trying out new things on the FEGSEM, Georges Vielleux (INRS-Varrenes) for his expertise and training on the XPS experiment. The McGill machine shop (Mr. Fred Kluck and Mr. Bill Bastian), Rick Rossi (electronics), and Georges Kopp (glassblowing) have been instrumental in creating exactly what I wanted (or better!) in a timely way.

My sincere thanks go out to the graduate secretaries, Renée Charron and Chantal Marotte, as well as the departmental secretaries, especially the chair's secretary, Sandra Aerssen, who have helped simplify the navigation through an often obtuse bureaucracy. For financial assistance, I would like to thank Bruce Lennox, McGill University Chemistry department, and the National Science and Engineering Research Council of Canada for a doctoral fellowship.

I am especially grateful to my family and friends who have provided me with solid support throughout this endeavour. My parents Francine and

Emanuel (my first and most important teachers), my brothers Anthony and Dave, Eleanor, and my little niece Abigail—you all inspire me, and give me confidence and faith in your own ways. I would also like to thank Pluto whose insanity has allowed me to feel relatively sane, and all Pluto-philes over the years at McGill—Carl, Mel, Lee and Stephanie, and Joy. Very warm thanks belong with Margaret Antler, Janet Caruana, and Jennifer Murphy—your support and friendships have been an invaluable part of my life at school and beyond.

Last, but certainly not least, I give my most heartfelt thanks to Ian Chute for his love, extreme patience, understanding, and support through this challenging time.

Table of Contents

| | |
|---|------|
| Abstract | i |
| Résumé | ii |
| Foreword | iii |
| Table of Contents | x |
| List of Frequently Used Symbols | xiv |
| List of Frequently Used Abbreviations | xv |
| | |
| <i>Chapter 1</i> | 1-1 |
| Introduction | |
| 1.1 General Introduction..... | 1-1 |
| 1.2 Objectives of the Thesis..... | 1-6 |
| 1.3 Nanopatterning | 1-7 |
| 1.3.1 Nanopatterned Topology | 1-8 |
| 1.3.2 Nanopatterned Distinct Nanoparticles | 1-11 |
| 1.3.3 Nanopatterning Methodologies..... | 1-13 |
| References | 1-22 |
| | |
| Connecting Text for Chapter 2..... | 2-0 |
| <i>Chapter 2</i> | 2-2 |
| Self-Assembled Masks for the Transfer of Nanometer-Scale Patterns into Surfaces: Characterization by AFM and LFM | |
| Abstract | 2-2 |
| 2.1 Introduction | 2-2 |
| 2.2 Experimental Section | 2-5 |
| 2.3 Results and Discussion..... | 2-7 |
| 2.4 Conclusions | 2-15 |

| | |
|--|------|
| Acknowledgments..... | 2-16 |
| References | 2-17 |
| | |
| Connecting Text for Chapter 3:..... | 3-0 |
| <i>Chapter 3</i> | 3-2 |
| Preparation of Nanoscale Au Islands in Patterned Arrays | |
| 3.1 Abstract | 3-2 |
| 3.2 Introduction | 3-2 |
| 3.3 Experimental Section | 3-6 |
| 3.4 Results and Discussion..... | 3-9 |
| 3.5 Conclusions | 3-15 |
| 3.6 Acknowledgements..... | 3-15 |
| References | 3-17 |
| | |
| Connecting Text for Chapter 4..... | 4-0 |
| <i>Chapter 4</i> | 4-1 |
| The Wetting of Nanopatterned Surfaces | |
| 4.1 Introduction | 4-1 |
| 4.2 Experimental Section | 4-7 |
| 4.3 Results and Discussion..... | 4-9 |
| 4.4 Conclusions | 4-18 |
| References | 4-19 |
| | |
| Connecting Text for Chapter 5..... | 5-0 |
| <i>Chapter 5</i> | 5-2 |
| Spectroscopic Characterization of Au Island Patterns formed on Solid Surfaces | |
| 5.1 Characterization of Au Island Pattern in Air..... | 5-2 |

| | |
|--|------|
| 5.1.1 Introduction | 5-2 |
| 5.1.2 Experimental Section | 5-4 |
| 5.1.3 Results and Discussion | 5-5 |
| 5.1.3.1 Modeling the Surface Plasmon Resonance Response of Au Islands | 5-8 |
| 5.2 Towards the design of a bio-/chemo-sensor | |
| The effect of the surrounding medium | 5-19 |
| 5.2.1 Introduction | 5-19 |
| 5.2.2 Experimental Section | 5-20 |
| 5.2.3 Results and Discussion | 5-21 |
| 5.2.3.1 Effect of Monolayer Coverage | 5-31 |
| 5.3 Conclusions | 5-35 |
| References | 5-37 |
| | |
| <i>Chapter 6</i> | 6-1 |
| Conclusions, Original Contributions to Knowledge, and Ideas for Future Work | |
| 6.1 Overview and Conclusions | 6-1 |
| 6.2 Original Contributions to Knowledge | 6-5 |
| 6.3 Ideas for Future Work | 6-5 |
| | |
| <i>Appendix 1</i> | A-1 |
| Supplementary Information for Chapter 2 | |
| 1.1 Langmuir films of PS-b-P2VP | A-1 |
| 1.2 The Effect of Different Substrate Properties on the Feasibility of Pattern Transfer | A-2 |
| 1.2.1 Substrate Roughness | A-2 |
| 1.2.2 Hydrophobic and Hydrophilic Substrates | A-4 |
| 1.2.3 Refractory Substrates | A-6 |
| References | A-8 |

| | |
|--|------|
| <i>Appendix 2</i> | A-9 |
| Further Details Concerning Making Gold Island Arrays | |
| 2.1 Elemental Analysis of Gold Island Arrays | A-9 |
| 2.2 Surface Resistance during Pattern Transfer | A-10 |
| 2.3 Making Au Islands on ITO..... | A-14 |
| | |
| <i>Appendix 3</i> | A-18 |
| Calculation of r and f(Chapter 4) | |
| | |
| <i>Appendix 4</i> | A-20 |
| Calculation of p_{quartz} (Chapter 5) | |
| | |
| <i>Appendix 5</i> | A-22 |
| Calculation of Extinction for Oblate Spheroids in the Quasistatic Approximation | |
| 5.1 Matlab program for Calculation of Extinction Coefficients of Oblate Gold Spheroids..... | A-22 |

List of Frequently Used Symbols

| | |
|------------------|--|
| h | Planck's constant, 6.63×10^{-34} J s |
| e^- | Electron |
| ε_1 | Real component of the dielectric function |
| ε_2 | Imaginary component of the dielectric function |
| ε_m | Dielectric constant (real component) of the medium |
| f | Fractional contact area |
| f_0 | Resonant frequency in kHz |
| G | Gibbs' free energy |
| γ | Surface tension/interfacial energy |
| k | Force constant in N/m |
| κ | Extinction coefficient |
| λ | Wavelength in meters |
| λ_{\max} | Wavelength corresponding to the peak maximum |
| ν | Frequency in Hz |
| N | Number |
| r | Total surface area/projected surface area |
| θ | Contact angle |
| θ_a | Advancing contact angle |
| θ_r | Receding contact angle |
| θ_w | Apparent contact angle defined by Wenzel |
| θ_c | Apparent contact angle defined by Cassie |
| θ_{cb} | Apparent contact angle defined by Cassie-Baxter |
| θ^* | Apparent contact angle |
| $\Delta\theta$ | Contact angle hysteresis |
| V | Volume |

List of Frequently Used Abbreviations

| | |
|--|--|
| AFM | Atomic force microscopy |
| Au-C5SH | Gold substrate derivatized with a pentanethiol monolayer |
| Au-C18SH | Gold substrate derivatized with a octadecanethiol monolayer |
| Au-Si | Patterned gold islands/nanoparticles on Si/SiO _x |
| Au-Si-C5SH | Pentanethiol-derivatized gold island array on Si/SiO _x |
| Au-Si-C18SH | Octadecanethiol-derivatized gold island array on Si/SiO _x |
| Au-Quartz | Patterned gold islands/nanoparticles on quartz substrate |
| FEGSEM | Field emission gun scanning electron microscopy |
| FFT | Fast fourier transform |
| FWHM | Full width at half maximum |
| LB | Langmuir-Blodgett |
| LFM | Lateral force microscopy |
| LSPR | Localised surface plasmon resonance |
| <i>n</i> -C ₅ H ₁₁ SH | Pentanethiol |
| <i>n</i> -C ₁₆ H ₃₃ SH | Hexadecanethiol |
| <i>n</i> -C ₁₈ H ₃₇ SH | Octadecanethiol |
| PS | Polystyrene |
| P2VP | Poly(2-vinylpyridine) |
| PS-P2VP | Polystyrene- <i>b</i> -poly(2-vinylpyridine) |
| rms | Root mean square |
| RIU | Refractive index unit |
| SEM | Scanning electron microscopy |
| Si/SiO ₂ | Silicon wafer with thermally-grown surface oxide layer |
| Si/SiO _x | Silicon wafer with native oxide surface layer |
| SPM | Scanning probe microscopy |
| TEM | Transmission electron microscopy |
| XPS | X-ray photoelectron spectroscopy |

Chapter 1

Introduction

1.1 General Introduction

Nanoscience is the science concerned with structures that have at least one dimension that is <100 nm. Nanostructures bridge the atomic/molecular size regime (roughly < 10 nm) to the “bulk” size regime (often >100 nm), and in doing so, bridge quantum and classical mechanics descriptions of matter. Key to nanoscience being a distinct science is the emergence of properties which are best described by concepts stemming from both approaches, and are directly linked to the size and shape of the nanostructure.

Although much of today’s interest in nanoscience originates from the prospect of new properties (and hence new materials) and the aspirations of nanotechnology, the initial driving force for nanoscience was miniaturization. Richard Feynman’s inspiring talk given at the 1959 American Physical Society (at Caltech), titled “There’s *Plenty* of Room at the Bottom”, is usually attributed to have initiated the idea by urging scientists to seek out the limits of technology¹. For example Feynman suggested using atoms to write the entire contents of the Encyclopaedia Britannica on the head of a pin. Since then, miniaturization technology has progressed at an exponential rate. In

particular, computers have doubled in information density and efficiency approximately every 18 months, a relationship known as “Moore’s (First) Law”². Although it is an empirical relationship, Moore’s (First) Law has become the computer/semiconductor industries’ road map, and has provided much of the recent impetus for nanoscience and nanotechnology. It is widely believed that the technologies which are responsible for the last 40 years of miniaturization, particularly in microelectronics, will face major challenges to develop processes down to the sub-100 nm scale³. This has focused attention on the problem of synthesis and spatial control of nanostructures.

Activity in nanoscience has been catalyzed by key synthetic and technological tools which make studying nanostructures considerably more accessible. Of particular importance is the scanning probe microscope (SPM), invented by Binnig and Rohrer in 1982 in the form of the scanning tunnelling microscope (STM).⁴ The unprecedented capability of SPM to visualize and manipulate surfaces at the atomic and nanometer scale has created experimental opportunities in nanoscience, such as single atom and molecule manipulation, and highly localized mechanical (elasticity, hardness), electronic, and magnetic measurements. Several other enablers of nanoscience, that have come along more recently (within the last 10-20 years), are facile synthetic methods for making nanostructures. Of particular

importance are metal and semiconducting nanoparticles and fullerenes. These materials have piqued the interest of many from all areas of science and engineering because of their unique, size-dependent properties. Like SPM, they are attractive because of their ability to interface these properties to the atomic/molecular and microscopic regimes. For example, considerable research activity is directed toward use of nanoparticles to detect DNA, transfect cell membranes for drug delivery, cell targeting, or cell labelling⁵⁻¹⁰. These applications generally aim to exploit the unique properties offered by these new materials and to take advantage of their small sizes. Because physical disruption by probes and materials is frequently a problem at the cellular level, the typical nanoparticle length scales of 1-20 nm are very attractive. Another example of the interest generated by nanostructures is their use as additives in polymer composite blends¹¹⁻¹⁴. With the relatively new tools available to nanoscience, it is becoming increasingly understood how bulk materials properties are implicitly linked to the nanoscale composition and structure. Like abalone shell nacre¹⁵⁻¹⁷, many materials become stronger when they are comprised of nanoscale components¹⁸⁻²⁰. Moreover, many nanoscale components, such as the carbon nanotubes, show considerably improved strength compared to their bulk counterparts.

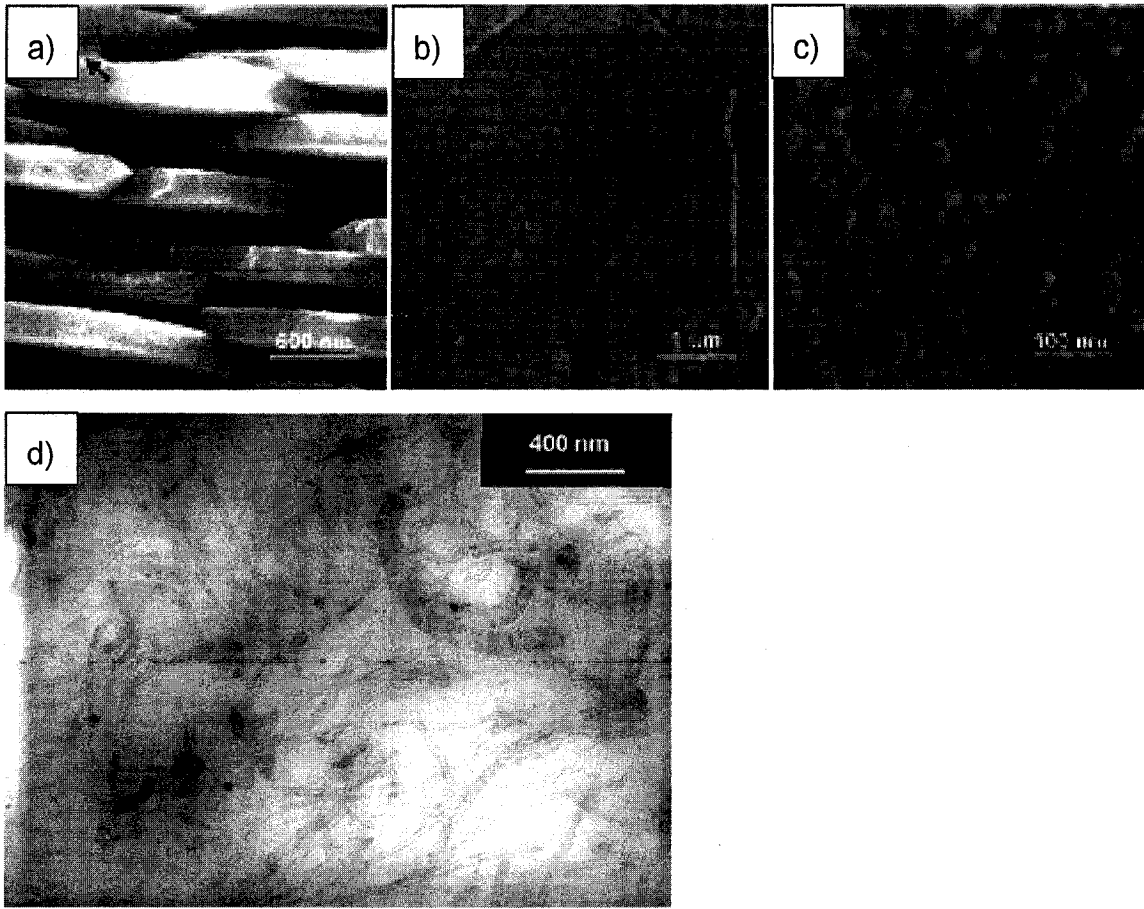


Figure 1-1: (a) Scanning electron microscopy (SEM) image of the nacreous cross-section of red abalone shells shows the stacking of aragonite platelets. (b) and (c) are atomic force microscopy images (topography and phase contrast respectively) of the top of an aragonite platelet revealing nanostructured phases. (d) SEM of multiwalled carbon nanotubes embedded in a poly(styrene-*co*-butyl acrylate) matrix to form a polymer nanocomposite. Images taken from reference 15 (a-c) and reference 20 (d).

A need for various types of spatial control, ranging from the ultra-specific (ability to address a single atom/molecule) to general ($>\mu\text{m}^2$ areas)

has become apparent in attempts to create new technologies and materials. For example, using carbon nanotubes (CNTs) as molecular wires requires that electrical contact is made specifically between the two ends of the CNT and electrical leads deposited on the host silicon surface. There are two common approaches to this problem. The first is to start with writing the pattern of leads on the surface and then have the CNTs assemble onto the leads (Figure 1-2a). The second is to allow the CNTs to assemble and then to specifically create the contacts on top of the CNT(s) of choice (Figure 1-2b). Both approaches require spatial control of different kinds and as such have inherent (dis)advantages that make them appropriate for certain applications. In many cases, this type of control is required for basic characterization of properties of nanostructures before one can begin formulating possible applications. This problem has resonated throughout the field of nanoscience, particularly with experiments involved with performing fundamental measurements of different phenomena on *single* nanostructures. Such measurements include conductivity and capacitance of nanoparticles and nanowires, and near-field coupling between magnetic and metallic nanostructures.

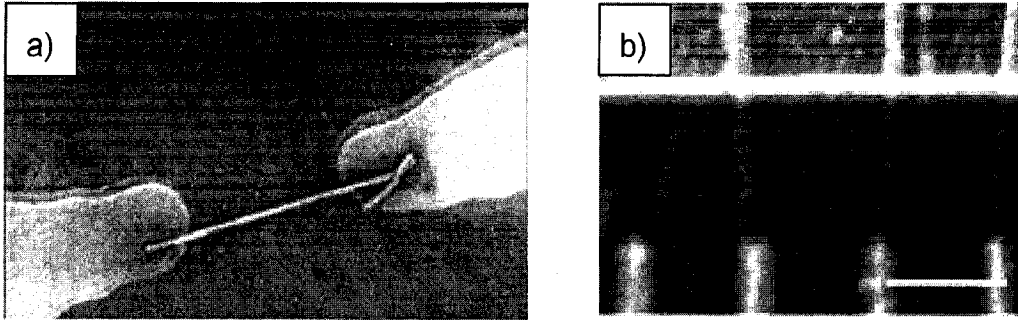


Figure 1-2: Different nanowire-probe assembly configurations. In (a) the Au nanowires are directed to assemble onto the predefined electrodes²¹ whereas in (b) the electrodes (bright, finger-like features at the bottom, and continuous bar electrode at the top) are patterned on top of a pre-assembled array of Si nanowires (thin bright lines, scale bar: 300 nm)²². Image in (a) was taken from reference 21 and (b) from reference 22.

1.2 Objectives of the Thesis

The subject of this Thesis is the generation and characterization of patterned nanostructures. The objectives are three-fold:

1. The development of an efficient, bottom-up, accessible and reliable method for patterning surfaces at the nanometer length scale.
2. To characterise the resulting nanopatterned surfaces in terms of surface energy and available electronic (optical) characterisation.

3. To explore the (experimentally accessible) applications of the nanopatterned surfaces.

Chapter 2 describes a novel methodology used to create self-patterned lithographic masks, and the pattern-transfer into solid substrates (chemically homogeneous patterns). Chapter 3 describes an extension of this methodology to create patterned arrays of gold nanoparticles (chemically heterogeneous pattern) on various substrates. Chapters 4 and 5 describe the surface energy and electronic characterization of these nanopatterned substrates in relation to applications in self-cleaning surfaces and bio-/chemo sensing respectively. Several Appendices are included which contain both a summary of some other studies performed, as well as supplementary information to the Thesis chapters.

The following sections of this Introduction will highlight some interesting studies making use of nanopatterned surfaces, provide an overview of the nanopatterning methods currently available, and will discuss some key aspects to the characterization methods used in this work.

1.3 Nanopatterning

1.3.1 Nanopatterned Topology (Chemically Homogeneous Patterns)

Introducing spatial control at the nanoscale with varying degrees of order introduces a number of interesting opportunities for study. At the very least, nanostructured surfaces have potential to improve upon a number of applications of microstructured surfaces ranging from self-cleaning^{23,24} and bio-compatible materials²⁵⁻³¹ to micro-/nanofluidics^{32,33}. It is also believed that in the case of superhydrophobic surfaces found on the leaves of the lotus plant, as well as the ultra-adhesive surfaces found on the feet of the gecko lizard, that it is not only the nanostructure aspect ratio, but also the shape and spacing between the (nano)structures that determine these properties³⁴⁻³⁶.

Much of the enhanced functionality inherent to nanostructured surfaces arises from their enhanced surface-to-volume ratio over conventional structures.

For example, thin semiconducting films of tin oxide (SnO_2), produced using pulsed laser deposition, have a variety of nanoscale morphologies depending on the deposition temperature. A study by Dolbec *et al.* correlates the resistivity of these films with their nanoscale morphology³⁷. The number density of grain boundaries is found to be particularly important to resistivity.

Many interesting properties of nanostructures arise from the fact that the nanoscale bridges the atomic/molecular length scale and the macromolecular and microscopic length scales. A good example of this is the

functionalization of a surface with cone-shaped dendrons by Hong *et al.* in making DNA microarrays³⁸. The dendron monolayer assembles at the surface to yield an apex-spacing of approximately 3 nm, onto which ss-DNA (single stranded) is then covalently bonded. Hong and coworkers found that the single nucleotide polymorphism (SNP) discrimination efficiency on the nanostructure is equivalent to the solution value, because the relief from steric hindrance provided by the dendron template is sufficient while not causing a loss in the sensitivity³⁸.

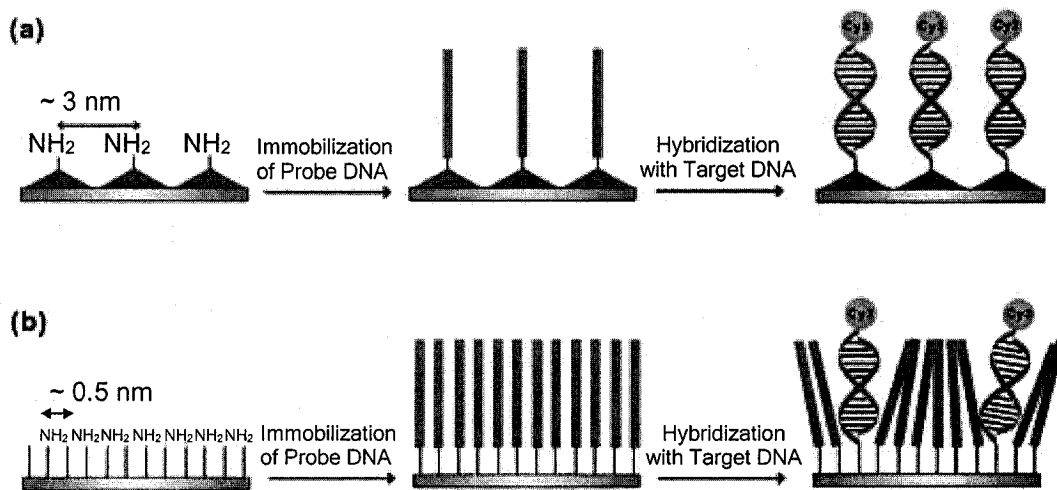


Figure 1-3: Schematic diagram showing DNA hybridization on (a) the dendron-modified substrate and (b) the monolayer-modified substrate.

(Image taken from reference 38).

Vessels within which the inner surface is patterned with nanoscale silicon pillars have been used to study the migration of molecules with dimensions comparable to that of the containing vessel³⁹⁻⁴². For example, Craighead *et al.* have used such vessels to describe electrophoretic and entropy-driven separation of DNA molecules. The outcome of these studies has consequences in micro-/nanofluidics, separation of macromolecules, and rapid genetic identification.

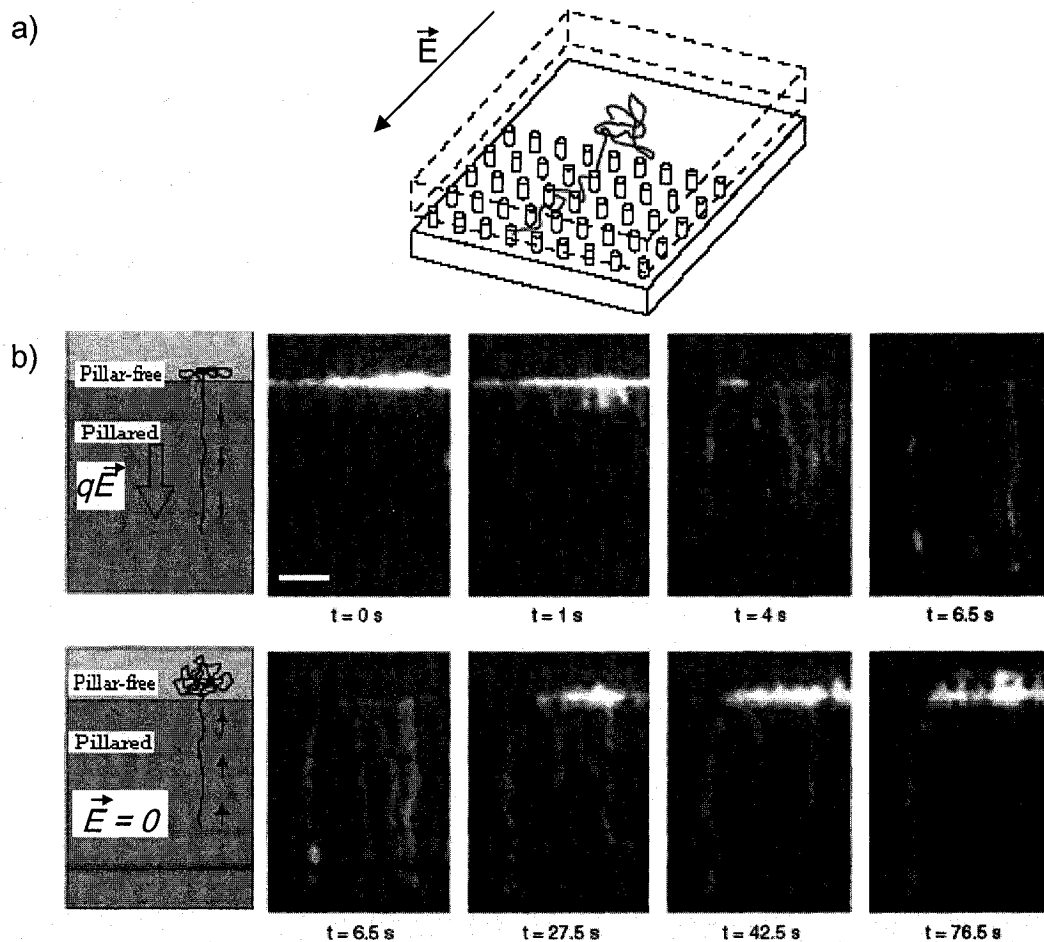


Figure 1-4: Schematic diagram (a) and optical micrographs (b) of fluorescently labelled-DNA migration through a vessel containing a nanopillar

array (35 nm diameter, 160 nm spacing, 60 nm height) when applied field is on (top) and entropic-recoil of shorter DNA strands when applied field is off (bottom). Images taken from reference 42.

As these examples demonstrate, the size, shape and spacing all play a significant role in creating interesting properties of nanoscale systems. A major advantage gained by nanopatterning is that creating a pattern intrinsically results in a built-in monodispersity in size, shape and spacing of the nanostructures.

1.3.2 Nanopatterned Distinct Nanoparticles (Chemically Heterogeneous Patterns)

Monolayers with spatially defined nanostructures that are chemically distinct from the substrate are interesting for many of the same reasons as are nanopatterned topological structures, except that they offer an additional level of chemical contrast. This makes possible the use of monolayer-coated surfaces to either effect chemically selective adsorption (“decoration”) in order to make more complex architectures or to locally change the surface energy. Control over both particle size and interparticle spacing in nanoparticle arrays have considerable impact in a number of applications. One example of this arises in the preparation of magnetic nanoparticle arrays. When

nanoparticles of magnetic materials (Fe, Co, Ni, and their alloys) are made smaller than approximately 10 nm they become *superparamagnetic*. This means that even below the Curie temperature of the material thermal motions overcome a particle's magnetic alignment, and the particle does not maintain a net magnetization when a field is not applied. However, by creating nearly monodisperse nanoparticles, Sun and coworkers have found that they can make close-packed superlattices, whose constituent nanoparticles are sufficiently coupled to one another that the films have significantly improved storage capability than thin films (of the same thickness) made in the conventional manner⁴³. The improvements realized are a direct result of having monodisperse nanoparticles which can then close pack in a highly uniform manner.

A lack of monodispersity in size and spacing often complicates the characterization of nanoparticle phenomena because when coupled to one another, nanoparticle properties can become substantially different. For example, much interest has been directed toward using the localized surface plasmon resonance (LSPR) absorbance of silver, gold and copper nanoparticles which occurs in the visible spectrum. While there are many examples of attempts to make use of the sensitivity of the nanoparticle LSPR signal to adsorbates⁴⁴⁻⁴⁹, few studies are able to use monodisperse (and

regularly spaced) nanoparticles. However, it has also been shown that both polydispersity and interparticle coupling change the sensitivity (peak shift) as well as the efficiency (peak shape) of the plasmon resonance⁵⁰⁻⁵².

1.3.3 Nanopatterning Methodologies

There are two general approaches to create nanostructures, which are also applied to nanopatterning. The first is the “top-down” approach, which is analogous to sculpting. The desired structure is generated by the removal of material starting from the bulk state. In making nanostructures, this approach tends to generate excess waste, is relatively slow, and involves very costly infrastructure. The advantage, however, of most “top-down” approaches is they can be scaled-up to run in parallel, thus increasing the speed and efficiency of the processing. The different types of lithography used to pattern surfaces (photolithography, X-ray lithography (XRL), electron-beam lithography (EBL), and ion-beam lithography (IBL)) are the most common examples of “top-down” techniques. Of these, the most widely used methodology is photolithography. Standard photolithography is ultimately limited in its capability to produce sub-100 nm structures by virtue of Rayleigh-limited resolution. While the remaining lithography approaches still offer a wide capability of structure shapes, sizes and spacings, they each

have limited applicability in most conventional laboratory settings due to low sample throughput, high infrastructure costs, or high cost per nanostructure⁵³.

The second technique used to generate nanostructures involves the “bottom-up” approach, where atoms and molecules serve as “building blocks” and are assembled in specific ways to result in a final superstructure. Some bottom-up approaches, such as techniques aiming to manipulate single atoms and molecules, are limited by being serial processes, making the creation of many nanostructures a very slow and inefficient process. On the other hand, many bottom-up approaches have the important advantage of having little or no resolution limit, and having the availability of a variety of shapes and spacings in the resulting nanostructures. Good examples of the bottom-up approach to nanostructure synthesis and patterning can be found in the approaches generally termed “SPM nanolithography”. SPM nanolithography makes use of the high lateral resolution (sub-Å) and sharp tip (typically ~10 nm radius) associated with the scanning probe microscope to generate structures, and patterns of structures, on surfaces. For example, SPM tips have been used to push around or pick up/drop off individual atoms and nanoparticles on surfaces in order to create a desired structure⁵⁴⁻⁵⁶. SPM tips have also been used create voids and ridges in soft surfaces, such as self-assembled monolayers and polymer films, by “embossing” and

“engraving/shaving” with the SPM tip⁵⁷⁻⁵⁹. Dip-pen lithography uses an SPM tip like a fountain pen to deliver molecules to the surface in a desired pattern⁶⁰. Many of these techniques have only been possible with the exceptional opportunities offered by SPM instrumentation and truly represent the state-of-the-art in lithography resolution. These methods are however limited by their ability to create nanostructures only in a serial rather than parallel manner.

Chemistry offers a number of solutions to the problem of serial processing in the “bottom-up” approach. Chemists’ expertise in parallel synthesis techniques can be applied to nanostructure formation. Chemical approaches to structure and pattern “synthesis” on the nanometer length scale are central to supramolecular chemistry. A common approach taken in supramolecular chemistry is the design of molecular building blocks for use in molecular *self-assembly*. Self-assembly may be defined as the process by which components spontaneously assemble into a structure via by non-covalent, low energy (~ 2-10 kJ/mol) interactions. This use of van der Waals forces and hydrogen bonds leads to properties unique to self-assembled structures. For example, structures (molecules) held together by strong, covalent interactions (200-800 kJ/mol) are not typically affected by changing the solvent, whereas solvents can play a major role in determining the final

architecture of a self-assembled structure. Covalently-bound structures are usually formed irreversibly and both desired and undesired products are formed. Isolation and purification considerations thus often dominate synthetic strategies. In contrast, error-correction (*via* kinetically accessible reversible processes) is a highly desirable feature of self-assembled systems.

One example of nanopatterning achieved via self-assembly involves the use of colloidal particles organized into a close-packed array on a surface. For example, Van Duyne *et al.* have taken polystyrene spheres (typically ~ 200 – 600 nm diameter) and spin-coated them as monolayer films on a glass surface^{53,61}. Depending on the solvent, concentration and spin rates, the resulting close-packed monolayers of spheres are then used as metal evaporation shadow masks. Evaporated silver into the (nm-scale) voids of the array, and subsequent removal of the spheres by sonication in solvent results in truncated tetrahedral silver nanoparticles remaining on the substrate in an array defined by the initial position of the polystyrene spheres. This is an excellent example of “bottom-up” nanostructure fabrication methodology that makes use of self-assembly and a subsequent parallel pattern-fixing process.

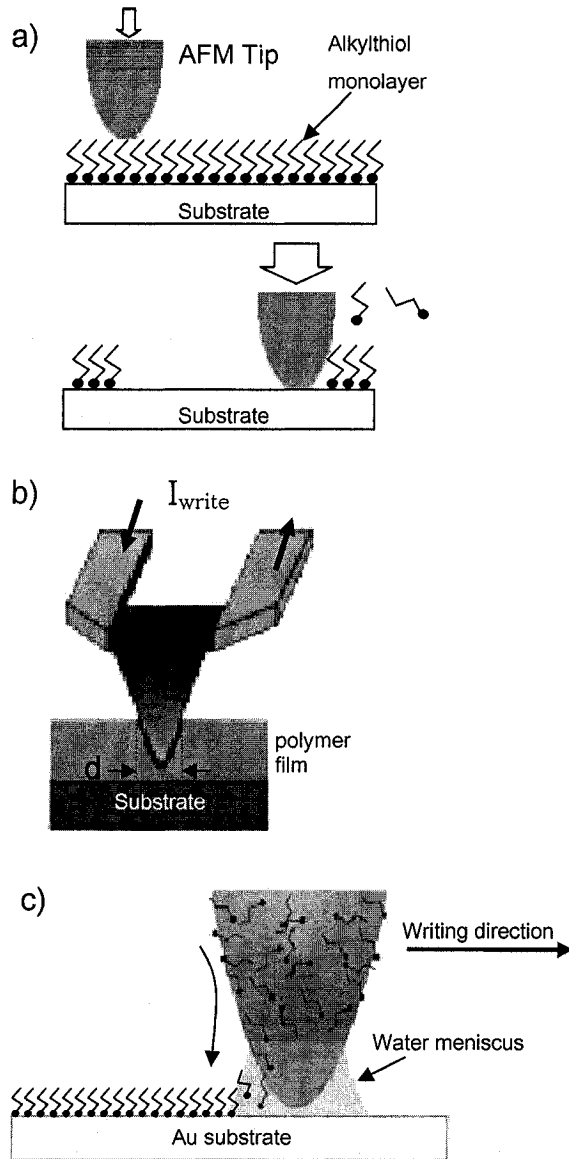


Figure 1-5: Schematic diagrams of (a) “nanoshaving” a self-assembled monolayer using an SPM tip to apply load to the surface, (b) “embossing” a hole (with diameter d) into a polymer film, where I_{write} is the electrical current applied to resistively heat the tip and locally melt the polymer film, and (c) dip-pen lithography which uses an AFM tip to deliver alkylthiol molecules to a

gold substrate. Images were taken from references 57, 58 and 60 respectively.

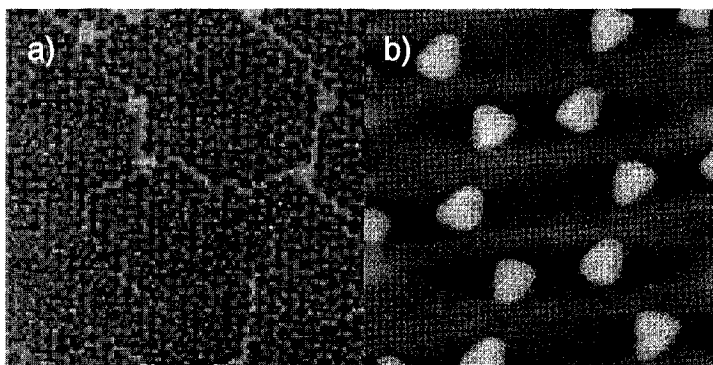


Figure 1-6: AFM (topography) images of (a) evaporation shadow-mask consisting of a spin-coated monolayer of polystyrene spheres used in nanosphere lithography. Evaporated silver fills the voids in the close-packed array and subsequent removal of the polystyrene spheres results in an array of truncated tetrahedral silver nanoparticles (b). Images were taken from reference 61.

There are many examples of self-assembly of small molecule amphiphiles in solution⁶². The resulting structures (micelles, lamellae, vesicles, etc.) depend on the intrinsic properties of the amphiphilic components (relative solubilities, size, shape, etc.) as well as the solvent, temperature, and concentration. Amphiphilic diblock copolymers are structurally analogous to low molecular weight amphiphiles and can self-assemble into an even greater number of structures in solution (spheres,

rods, vesicles, hexagonally packed hoops, etc.) when the solvent is incrementally changed such that only one of the blocks is favored⁶³. Diblock copolymer systems exhibit similar behaviour in solid-phase films after temperature annealing for several hours⁶⁴. These films can be used as nanopatterned masks for the generation of (nano)patterned substrates in several ways⁶⁵⁻⁷⁰(Figure 1-7). Because the final film morphologies consist of phase-separated, ordered domains of each block, one of the blocks is usually selectively (chemically) removed in order to create either topological contrast or material contrast. Given the range of shapes, sizes, and spacings that are achievable by changing the relative and absolute block lengths in the copolymer, these methodologies are an interesting alternative to the lithographic approaches described above⁶⁹.

Self-assembly at the air-water interface is determined in the balance between wettability (interfacial energy) and intermolecular van der Waals forces. As a result, amphiphiles can assemble into a number of configurations (phases) at the air-water interface. Given the similarities in the behaviour of small molecule amphiphiles and block copolymers in solution, it follows that block copolymers deposited at the air-water interface show a rich variety of phase behaviour. A number of these systems have previously been studied in this laboratory. In particular, work by Zhu *et al.* reported the

discovery of self-assembly in the polystyrene-*b*-polyvinylpyridine system at the air-water interface⁷¹⁻⁷⁶. This process is driven by hydrophobic nature of the polystyrene block such that in a 1:1 block ratio, circular surface micelles are the thermodynamically preferred morphology. The resulting surface micelle cores of polystyrene are surrounded by a polar polyvinylpyridine corona. Self-assembly of this polymer system has been exploited in this Thesis by using the surface micellar films as self-patterned sacrificial masks for pattern-transfer into substrates.

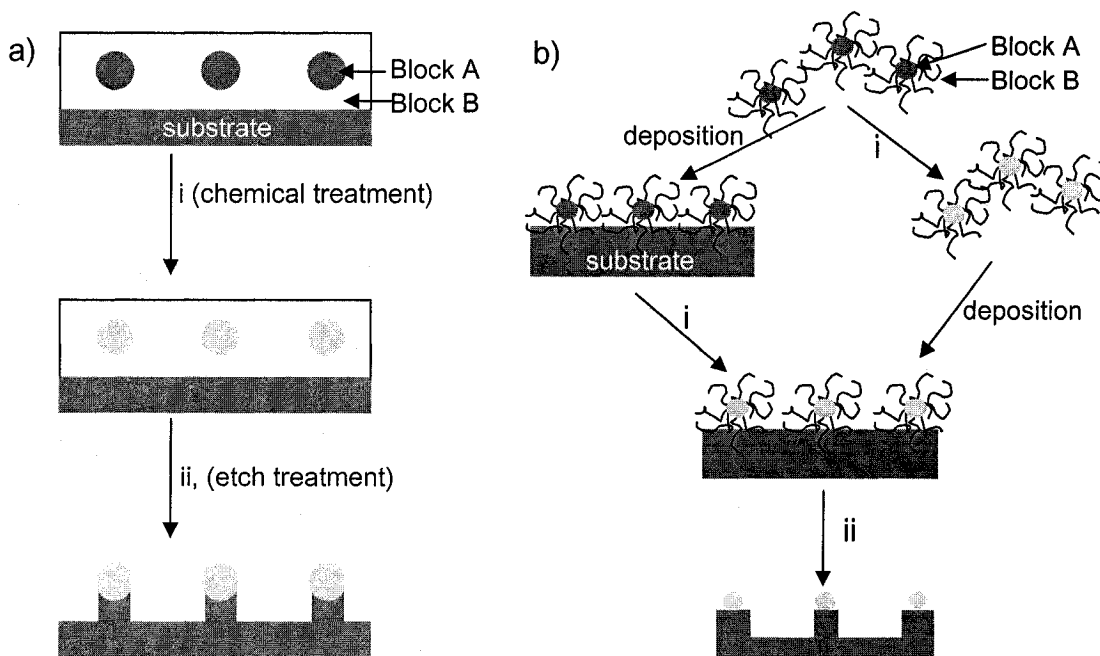


Figure 1-7: Two general approaches to nanopatterning using block copolymer (AB) thin films (a) and solution micelles (b). Phase-segregated block copolymer domains are deposited onto a substrate, then (i) chemically

treated to enhance chemical contrast between domains followed by a chemically selective pattern-transfer (etch) step (ii).

References

1. Feynman, R. P. *Caltech Eng. Sci. J.* 1960, and available at <http://www.foresight.org/nano/history.html>.
2. Moore, G. E. *Electronics* 1965, 38.
3. Madou, M. *Fundamentals of Microfabrication*, CRC Press LLC: Boca Raton, Florida, 1997.
4. Binnig, G.; Rohrer, H.; Gerber, C.; Weibel, E. *Phy. Rev. Lett.* 1982, 49, 57-61.
5. Storhoff, J. J.; Marla, S. S.; Garimella, V.; Mirkin, C. A. *Microarray Technol. Appl.* 2005, 147-179.
6. Drake, T. J.; Zhao, X. J.; Tan, W. *Nanobiotechnology* 2004, 444-457.
7. Gao, X.; Nie, S. *Nanobiotechnology* 2004, 343-352.
8. Gao, X.; Cui, Y.; Levenson, R. M.; Chung, L. W. K.; Nie, S. *Nature Biotechnol.* 2004, 22, 969-976.
9. Kumar, M. N. V. R.; Bakowsky, U.; Lehr, C.-M. *Nanobiotechnology* 2004, 319-342.
10. Rosi, N. L.; Mirkin, C. A. *Chem. Rev.* 2005, 105, 1547-1562.
11. Cammarata, R. C. *Intro. Nano. Sci. Technol.* 2004, 199-213.
12. Schadler, L. S. *Nanocomposite Science and Technology* 2003, 77-153.
13. Schadler, L. S. In *Nanocomposite Science and Technology*, Ajayan, P. M., Schadler, L. S., Braun, P. V., Eds.; Wiley-VCH Verlag GmbH & Co.: Online Publication, 2004; Vol. DOI: 10.1002/3527602127.ch2.
14. Caseri, W. *Chem. Nanostruc. Mater.* 2003, 359-386.
15. Li, X.; Chang, W.-C.; Chao, Y. J.; Wang, R.; Chang, M. *Nano Lett.* 2004, 4, 613-617.
16. Smith, B. L.; Schaffer, T. E.; Viani, M.; Thompson, J. B.; Frederick, N. A.; Kind, J.; Belcher, A.; Stucky, G. D.; Mors, D. E.; Hansma, P. K. *Nature* 1999, 399, 761-763.
17. Sarikaya, M.; Aksay, I. A. *Chem. Process. Adv. Mater.* 1992, 543-55.
18. Ajayan, P. *Nanocomp. Sci. Technol.* 2003, 1-75.

19. Amato, I. *Mater. Sci. Forum* 2004, 455-456, 550-555.
20. Dalmas, F.; Chazeau, L.; Gauthier, C.; Masenelli-Varlot, K.; Dendievel, R.; Cavaille, J. Y.; Forro, L. *J. Poly. Sci. Pol. Phys.* 2005, 43, 1186-1197.
21. Mbindyo, J. K. N.; Mallouk, T. E.; Mattzela, J. B.; Kratochvilova, I.; Razavi, B.; Jackson, T. N.; Mayer, T. S. *J. Am. Chem. Soc.* 2002, 124, 4020-4026.
22. Jin, S.; Whang, D.; McAlpine, M. C.; Friedman, R. S.; Wu, Y.; Lieber, C. M. *Nano Lett.* 2004, 4, 915-919.
23. Krupenkin, T. N.; Taylor, J. A.; Schneider, T. M.; Yang, S. *Langmuir* 2004, 20, 3824-3827.
24. Lau, K. K. S.; Bico, J.; Teo, K. B. K.; Chhowalla, M.; Amaratunga, G. A. J.; Milne, W. I.; McKinley, G. H.; Gleason, K. K. *Nano Lett.* 2003, 3, 1701-1705.
25. Muller, B.; Riedel, M.; Michel, R.; De Paul, S. M.; Hofer, R.; Heger, D.; Grutzmacher, D. *J. Vac. Sci. & Tech. B* 2001, 19, 1715-1720.
26. Papra, A.; Bernard, A.; Juncker, D.; Larsen, N. B.; Michel, B.; Delamarche, E. *Langmuir* 2001, 17, 4090-4095.
27. Ferraro, J. T.; Daneshmand, M.; Bizios, R.; Rizzo, V. *Am. J. Physiol.* 2004, 286, C831-C839.
28. Hasenbein, M. E.; Andersen, T. T.; Bizios, R. *Biomaterials* 2002, 23, 3937-3942.
29. Dalby, M. J.; Pasqui, D.; Affrossman, S. *IEE Proc.- Nanobiotech.* 2004, 151, 53-61.
30. Dalby, M. J.; Riehle, M. O.; Sutherland, D. S.; Agheli, H.; Curtis, A. S. G. *Biomaterials* 2004, 25, 5415-5422.
31. Elias, K. L.; Price, R. L.; Webster, T. J. *Biomaterials* 2002, 23, 3279-3287.
32. Blossey, R. *Nat. Mater.* 2003, 2, 301-306.

33. Cottin-Bizonne, C.; Barrat, J.-L.; Bocquet, L.; Charlaix, E. *Nat. Mater.* **2003**, *2*, 237-240.
34. Sun, T.; Feng, L.; Gao, X.; Jiang, L. *Acc. Chem. Res.* **2005**, ACS ASAP.
35. Arzt, E.; Gorb, S.; Spolenak, R. *PNAS* **2003**, *100*, 10603-6.
36. Öner, D.; McCarthy, T. J. *Langmuir* **2000**, *16*, 7777-7782.
37. Dolbec, R.; El Khakani, M. A.; Serventi, A. M.; Trudeau, M.; Saint-Jacques, R. G. *Thin Solid Films* **2002**, *419*, 230-236.
38. Hong, B. J.; Oh, S. J.; Youn, T. O.; Kwon, S. H.; Park, J. W. *Langmuir* **2005**, *21*, 4257-4261.
39. Seo, Y.-S.; Luo, H.; Samuilov, V. A.; Rafailovich, M. H.; Sokolov, J.; Gersappe, D.; Chu, B. *Nano Lett.* **2004**, *4*, 659-664.
40. Han, J.; Craighead, H. G. *Anal. Chem.* **2002**, *74*, 394-401.
41. Foquet, M.; Korlach, J.; Zipfel, W.; Webb Watt, W.; G., C. H. *Anal. Chem.* **2002**, *74*, 1415-22.
42. Turner, S. W. P.; Cabodi, M.; Craighead, H. G. *Phy. Rev. Lett.* **2002**, *88*, 128103/1-128103/4.
43. Sun, S.; Murray, C. B.; Weller, D.; Folks, L.; Moser, A. *Science* **2000**, *287*, 1989-1992.
44. Hutter, E.; Pileni, M.-P. *J. Phys. Chem. B* **2003**, *107*, 6497-6499.
45. Taton, T. A.; Mirkin, C. A.; Letsinger, R. L. *Science* **2000**, *289*, 1757-1760.
46. Haes, A. J.; Van Duyne, R. P. *J. Am. Chem. Soc.* **2002**, *124*, 10596-10604.
47. Krasteva, N.; Besnard, I.; Guse, B.; Bauer, R. E.; Muellen, K.; Yasuda, A.; Vossmeier, T. *Nano Lett.* **2002**, *2*, 551-555.
48. Nath, N.; Chilkoti, A. *Anal. Chem.* **2002**, *74*, 504-509.
49. Zhang, H. L.; Evans, S. D.; Henderson, J. R.; Miles, R. E.; Shen, T. H. *Nanotechnology* **2002**, *13*, 439-444.

50. Malynych, S.; Chumanov, G. *J. Am. Chem. Soc.* **2003**, *125*, 2896-2898.
51. Atay, T.; Song, J.-H.; Nurmikko, A. V. *Nano Lett.* **2004**, *4*, 1627-1631.
52. Kreibig, U.; Vollmer, M. *Optical Properties of Metal Clusters*; Springer: Berlin, 1995.
53. Hulteen, J. C.; Treichel, D. A.; Smith, M. T.; Duval, M. L.; Jensen, T. R.; Van Duyne, R. P. *J. Phys. Chem. B* **1999**, *103*, 3854-3863.
54. Crommie, M. F.; Lutz, C. P.; Eigler, D. M.; Heller, E. J. *Surf. Rev. Lett.* **1995**, *2*, 127-37.
55. Eigler, D. M. *NATO ASI Ser. E* **1993**, *239*, 1-10.
56. Weiss, P. S.; Eigler, D. M. "What is underneath (adsorbate). Moving atoms and molecules to find out," Dep. Chem., Pennsylvania State Univ., University Park, PA, USA., 1992.
57. Liu, G.-Y.; Xu, S.; Qian, Y. *Acc. Chem. Res.* **2000**, *33*, 457-466.
58. Binnig, G.; Despont, M.; Drechsler, U.; Haberle, W.; Lutwyche, M.; Vettiger, P.; Mamin, H. J.; Chui, B. W.; Kenny, T. W. *Appl. Phys. Lett.* **1999**, *74*, 1329-1331.
59. Geissler, M.; Xia, Y. *Adv. Mater.* **2004**, *16*, 1249-1269.
60. Piner, R. D.; Zhu, J.; Xu, F.; Hong, S.; Mirkin, C. A. *Science* **1999**, *283*, 661-663.
61. Jensen, T. R.; Schatz, G. C.; Van Duyne, R. P. *J. Phys. Chem. B* **1999**, *103*, 2394-2401.
62. Israelachvili, J. N. *Intermolecular and Surface Forces*; Academic Press Inc.: San Diego, 1992.
63. Cameron, N. S.; Corbierre, M. K.; Eisenberg, A. *Can. J. Chem.* **1999**, *77*, 1311-1326.
64. Bates, F. S.; Fredrickson, G. H. *Ann. Rev. Phy. Chem.* **1990**, *41*, 525-57.
65. Park, M.; Harrison, C.; Chaikin, P. M.; Register, R. A.; Adamson, D. H. *Science* **1997**, *276*, 1401.

66. Park, C.; Yoon, J.; Thomas, E. L. *Polymer* **2003**, *44*, 7779.
67. Hamley, I. W. *Nanotechnology* **2003**, *14*, R39-R54.
68. Turner, A., T.; Steiner, R.; DeRouchey, J.; Stafford, C. M.; Huang, E.; Bal, M.; Tuominen, M.; Hawker, C. J.; Russell, T. P. *Adv. Mater.* **2000**, *12*, 787-791.
69. Guarini, K. W.; Black, C. T.; Zhang, Y.; Kim, H.; Sikorski, E. M.; Babich, I. V. *J. Vac. Sci. Technol. B* **2002**, *20*, 2788-2792.
70. Black, C. T.; Guarini, K. W.; Sandstrom, R. L.; Yeung, S.; Zhang, Y. *MRS Symp. Proc.* **2002**, *728*, 79-86.
71. Zhu, J.; Eisenberg, A.; Lennox, R. B. *J. Am. Chem. Soc.* **1991**, *113*, 5583-8.
72. Zhu, J.; Eisenberg, A.; Lennox, R. B. *Macromolecules* **1992**, *25*, 6556-62.
73. Zhu, J.; Eisenberg, A.; Lennox, R. B. *Macromolecules* **1992**, *25*, 6547-55.
74. Zhu, J.; Hanley, S.; Eisenberg, A.; Lennox, R. B. *Makromol. Chem.* **1992**, *53*, 211-20.
75. Zhu, J.; Lennox, R. B.; Eisenberg, A. *J. Phys. Chem.* **1992**, *96*, 4727-30.
76. Zhu, J.; Lennox, R. B.; Eisenberg, A. *Langmuir* **1991**, *7*, 1579-84.

Connecting Text for Chapter 2:

Self-Assembled Masks for the Transfer of Nanometer-Scale Patterns into Surfaces: Characterization by AFM and LFM

This Chapter describes the preparation of arrays of nanoscale features in surfaces, where the arrays are predefined by the diblock copolymer surface micellar film structure. A high-fidelity transfer of the mask topology to the substrate results. Given a suitably *smooth* substrate, the substrate is found to play a minimal role in determining the final structure of the patterned features, thus yielding an efficient, accessible, and general methodology for introducing periodic nanoscale topology to surfaces. It therefore serves as an excellent example of surface patterning on the nanometer length scale, and is the core methodology used in the Thesis.

Atomic Force and Lateral Force Microscopy (AFM, LFM) and X-ray photoelectron spectroscopy (XPS) were used to characterise the morphology of the surfaces and to track the removal of the diblock copolymer film during the pattern transfer process, respectively. The LFM results inform us on two issues. The first is nanoscale features can produce misleading lateral friction contrast, normally interpreted as chemical contrast. The second issue is the adsorption of ambient water to the nanostructured surfaces may be non-conformal, an issue explored in Chapter 4. The generation of patterned

nanostructures in silicon and gold substrates enabled the study pursued in Chapter 4. In addition, Appendix 1 provides information related to the methodology described in this paper.

Chapter 2

Self-Assembled Masks for the Transfer of Nanometer-Scale Patterns into Surfaces: Characterization by AFM and LFM*

* *This paper was reproduced with permission from Nano Letters* **2002**, 2(2), 131-135.

Copyright 2002 American Chemical Society. It is coauthored by Antonella Badia, Peter Grütter, and R. Bruce Lennox. The text below is a verbatim copy of the published paper.

Abstract

A new methodology has been used to create an extensive array of nanometer-sized features through the Ar⁺ milling of Si/SiO_x and gold surfaces covered with a diblock copolymer mask with an intrinsic topological nanopattern. Mask removal was tracked using XPS and the final arrays were characterized by AFM and LFM. Friction contrast observed throughout the transferred pattern is associated with a surface water layer.

2.1 Introduction

The micromachining of materials with features in the 0.1 nm to 100 nm range¹ is of great interest for use in electronic devices,² sensors (optical, pressure, electronic, etc.)³⁻⁵ and separation science.^{6,7} Despite advances in

lithography, it remains extremely difficult and expensive to realize nanometer-sized structures in an efficient and parallel process. Mask-based lithographic techniques, while being an entry into the parallel fabrication of features, face considerable challenges involving the interplay of the Rayleigh limit of the impinging etch beam ($h\nu$, e^-) and the chemical demands of the mask. These problems are compounded by the difficulty in creating a mask with the desired nanometer features in the first instance. Given these challenges, we have explored the use of self-organizing polymer monolayers as a sacrificial etch mask. Building on our experience with the phenomenon of 2D self-ordered arrays of self-assembled diblock copolymers,⁸⁻¹⁴ we describe here a methodology in which a polymer film with an intrinsic topological pattern serves as a mask in the (nano)machining of Si/SiO_x, SiO₂, and gold surfaces. The result is a high fidelity transfer of the mask features into the underlying solid surface, generating an array of topologically distinct features which are ca. 50 nm in diameter, with a periodicity of 110 nm, and exhibit friction contrast by lateral force microscopy (LFM).

There have been several successful demonstrations where pattern-forming materials have been used as masks for the creation of surface nanostructures. Möller and co-workers have shown that block copolymer reverse micelles deposited on a surface self-order and can be selectively

derivatized to provide etch contrast.^{15,16} Register, Chaikin, and co-workers¹⁷⁻¹⁹ have been able to exploit the selective reactivity of one component of a block copolymer mask (i.e. polybutadiene domains in polystyrene matrices) to yield a versatile nanoscale mask system. Both these approaches rely on the mask having an intrinsic chemical pattern, whereupon follow-up chemical reactivity¹⁵⁻²⁰ yields the desired topological features in the mask. One variation involves using a diblock copolymer that has intrinsic etch contrast.²¹ Transfer of these features then involves ion-milling or reactive ion etching technologies. A more desirable configuration, which essentially eliminates a step in the fabrication process of the transferred pattern, is one where a mask with intrinsic topological contrast is used as a sacrificial mask in a chemically *unselective* etch process. Such a configuration was demonstrated by Clark and co-workers, where a 2D array of bacterial proteins was an effective topological mask towards an Ar⁺ milling beam.^{22,23} 6 nm features with 25 nm periodicity resulted over cm² of surface. Several novel etch masks have recently been employed to create nanostructures in solid surfaces. For example, gold nanoparticles deposited on Si act as condensation nuclei and after etching lead to ca. 10 nm (diameter) by 100 nm (height) Si pillars.²⁴ Rigid rod-like protein assemblies (microtubules) provide a mask, which after etching, yields structures ca. 50 nm wide by several microns long.²⁵ The

successful introduction of topological contrast to a surface using a phase-separated polymer²⁶ suggests that the block copolymer surface micelle mask could be used for pattern transfer in a manner similar to that used in the protein mask system.

Surface micelles formed from symmetric amphiphilic block copolymers at the air/water interface are circular in nature and have aggregation numbers in the range of 100-125.⁹ The (narrow) polydispersity of the unimer combined with the distribution in aggregation numbers lead to the formation of an array of surface micelles with a narrow but finite size distribution. This surface micelle system has the unique design capability wherein the dimensions of the features in the desired mask can be tuned by choosing the appropriate block lengths.^{13,27}

2.2 Experimental Section

Langmuir-Blodgett (LB) monolayer films of surface micelles were prepared by evenly spreading 80-100 μL of a 0.5 mg/ml chloroform solution of polystyrene(510)-b-poly-2-vinylpyridine(480) ($M_w/M_n = 1.06$, Polymer Source Inc., Dorval, Canada) in ca. 5 μL drops onto a 18M Ω water surface (23 °C, KSV 3000). 20 mins elapsed after spreading before the Langmuir-Blodgett transfer began. The LB film was compressed at a rate of 5 mm/min to a surface pressure of 2 mN/m, and then transferred to a clean substrate²⁸ at 1

mm/min (upward deposition). The resulting LB films consist of a quasi-hexagonal array of surface micelles composed of disk-like polystyrene (PS) cores surrounded by a continuum of poly-2-vinylpyridine (P2VP) coronae (Figure 1).^{8,11,29} The monolayer-coated substrate was then exposed to an Ar⁺ ion beam at 5 keV ($I = 70$ nA, flux = $3.5 \mu\text{A}/\text{cm}^2$, 50° from surface normal) for a variety of exposure times (60 to 900 s). The progress of the ion-milling process was tracked by x-ray photoelectron spectroscopy (XPS) with a VG ESCALAB 220i-XL spectrometer employing a monochromatic Al K α x-ray source ($h\nu=1486.6$ eV). The milled substrates were subsequently imaged using atomic force microscopy (AFM) and lateral force microscopy (LFM) with a Digital Instruments Multimode AFM (Nanoscope IIIA) using oxide-sharpened silicon nitride tips ($k=0.58$ N/m, Digital Instruments).

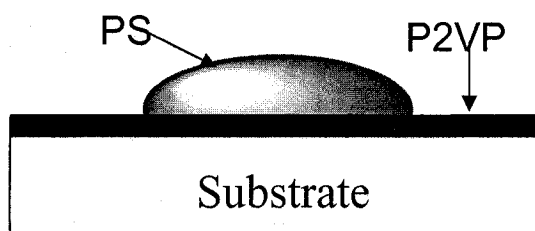


Figure 1: Schematic side profile of a PS-P2VP surface micelle. The PS core is ca. 4.5 nm high, and the P2VP corona is ca. 1 nm thick.²⁹

2.3 Results and Discussion

Figure 2 depicts typical AFM images of the PS-P2VP surface micelle film transferred to a Si/SiO_x substrate (Semiconductor Processing Inc., Ottawa, Canada). The surface micelle pattern extends over the entire substrate (several cm²). A typical 1 μm² area of the symmetric diblock (PS₅₁₀-P2VP₄₈₀) used here results in surface micelles whose dimensions are 4.5±0.5 nm (height), and 50±5 nm full width at half maximum (FWHM), and which form a pattern whose periodicity is 110±10 nm (Figure 2). The range of these dimensions for a large area (~100 μm²) is however greater, where the average height is 4.5±1 nm, the FWHM is 50±20 nm, and the periodicity is 110±30 nm.

Figure 3 shows the changes in relative intensity of the N1s and Si2p maxima obtained by XPS throughout the ion-milling process. Before ion-milling begins, a prominent N1s peak associated with the P2VP block is observed at 400 eV. 300 s of ion milling leads to the disappearance of this peak to background noise levels, which is consistent with the polymer mask being completely removed. The Si2p peak (99 eV), corresponding to elemental Si, increases with longer Ar⁺ beam exposure, while the peak at 103 eV (corresponding to the native Si oxide layer), diminishes to the background noise level. These results imply that after 150 s milling, the polymer monolayer has been almost completely removed. In this time frame the

native oxide layer has been completely milled away, exposing underlying bulk Si.

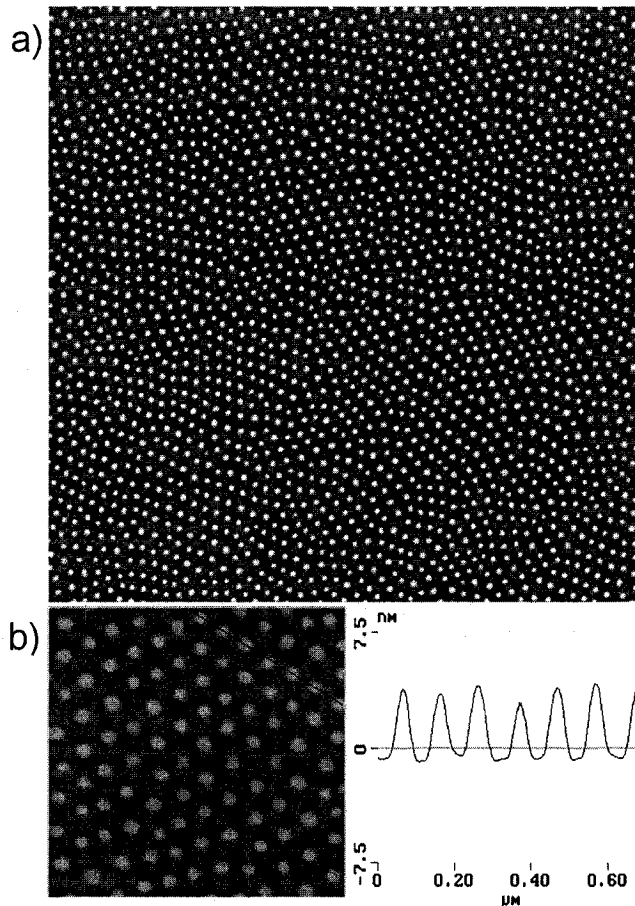


Figure 2: AFM images of a PS-P2VP surface micelle film deposited on Si/SiO_x obtained with tapping mode imaging using a Si cantilever ($f_0 \sim 300$ kHz, NanoSensors). a) 5 μm x 5 μm area; b) 1 μm x 1 μm area (left) with cross-section profile (right).

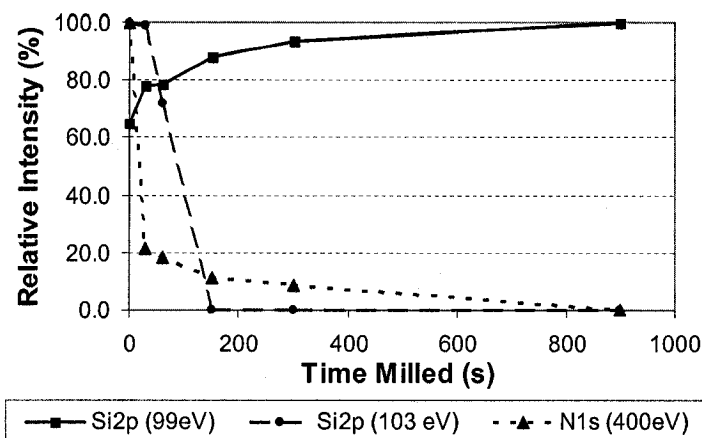


Figure 3: XPS relative intensities for the Si2p and N1s maxima followed as a function of Ar⁺ beam exposure time (0 to 900 s). Lines serve only as visual aids.

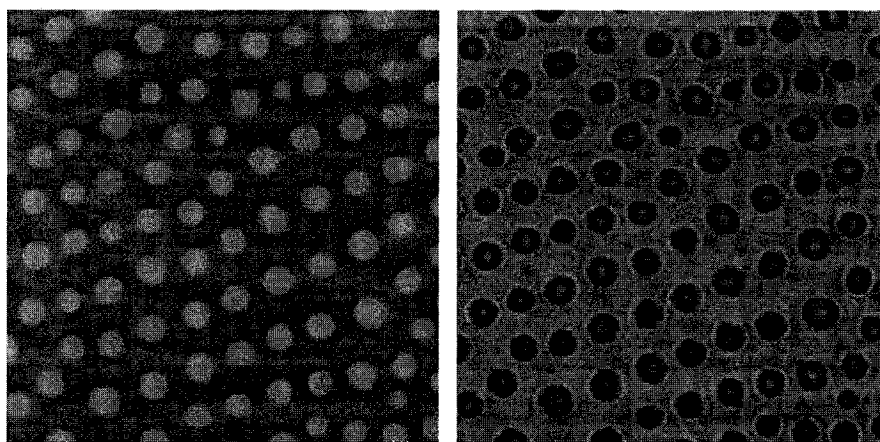


Figure 4: 1 μm x 1 μm AFM (left) and LFM (right) images of PS-P2VP mask transferred into Si/SiO_x after 300 s ion milling. Bright features in AFM image correspond to higher height, and darker features in LFM image correspond to lower friction. Note that the exact area imaged here is not the exact same area imaged in Figure 2b.

AFM and LFM were performed in order to assess the topological and friction contrast which result from this masked etching process. Experiments were performed in ambient conditions (air, room temperature ca. 20°C). All LFM images presented here were obtained by subtracting the retrace from the trace scan in order to essentially remove topography convolution. Figure 4 is a typical example of the results obtained for the pattern milled into a Si substrate.³⁰ The AFM (topography) images suggest that the dimensions of the transferred pattern are not dependent on the milling time (60 to 900 s). The contact mode AFM topological images clearly show that the pattern formed in the Si/SiO_x surface is a high fidelity replica of the original diblock copolymer mask. Both the feature dimensions and periodicity of the mask are effectively transferred into the Si surface by the ion-milling process. The differences noted between Figure 2B and Figure 4 are within the limits of the feature size distribution of the original polymer mask (see Figure 4 caption). It is noteworthy that the chemically unselective ion milling process employed yields feature heights in substrates that are similar to those of the mask. However, some variation in the heights of the features can occur if the substrate has a significantly different ion-milling rate than do the components of the mask.

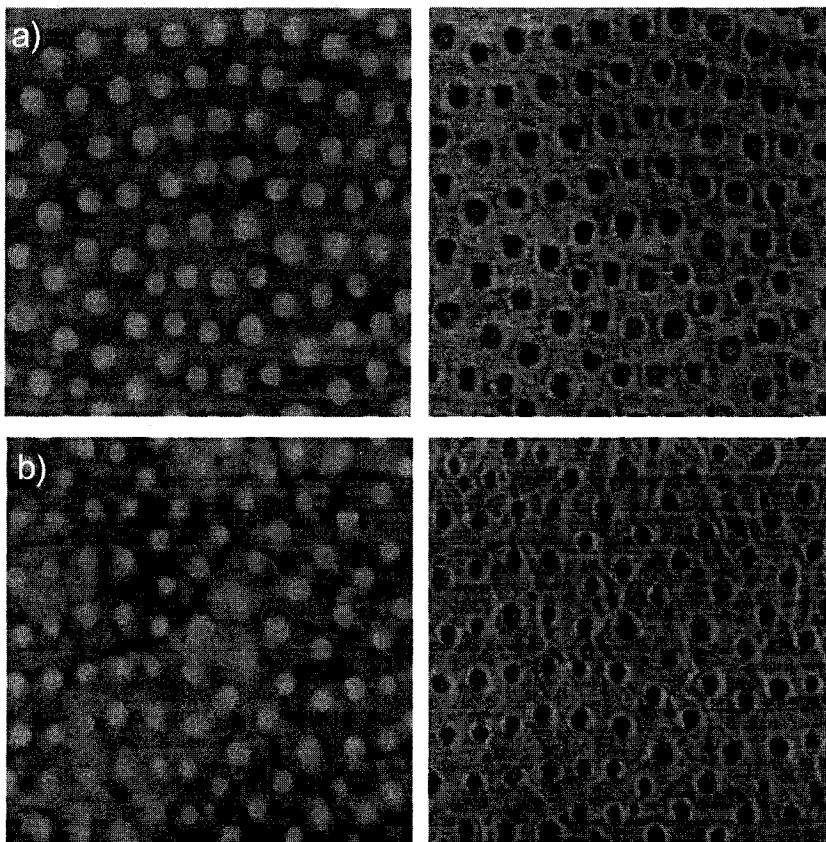


Figure 5: 1 μm x 1 μm AFM (left) and LFM (right) images of PS-P2VP pattern milled for 150 s into a) Si/SiO₂ and b) Au.

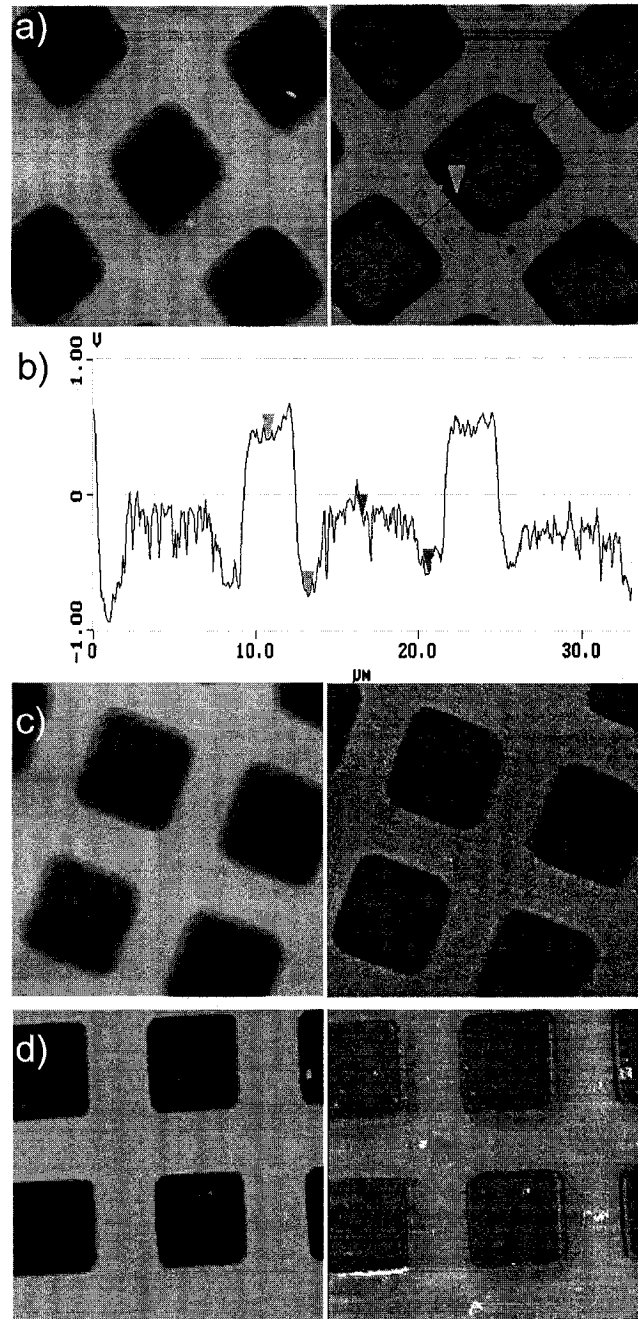


Figure 6: 25 μm x 25 μm AFM (left) and LFM (right) images of substrates ion-milled through a superfine mesh TEM grid. a) 100 nm-deep pits formed by milling for 300 s into Si/SiO_x; b) Cross-section profile for LFM image in a); c)

60 nm-deep pits formed from milling for 150 s into Si/SiO₂; d) 100 nm-deep pits formed from milling for 60 s into Au.

LFM imaging yields interesting contrast (Figures 4, 5, 6) that can arise from a number of sources. LFM contrast can arise from contact-related forces (adhesion, friction) as well as capillary effects³¹⁻⁴¹ associated with tip-adsorbed water interactions when imaging is performed under ambient conditions. The LFM contrast observed in Figures 4 and 5b is related to the surface topography and *not* to chemical contrast on the surfaces. Two series of experiments were performed to help determine the origin of the contrast observed in the LFM image. Firstly, nanopatterns were formed on both a SiO₂ substrate (in the form of a 114 nm thick oxide layer on a Si wafer (AMC, Edmonton, Canada) and a smooth 200 nm thick Au substrate.⁴²⁻⁴⁴ The observed LFM contrast (Figure 5) parallels that observed on the Si/SiO_x substrate (Figure 4), suggesting that the difference in friction observed between the “hills” and the “valleys” in the nanopattern is not intrinsic to the substrate used. Instead, we find that the friction is related in some way to the intrinsic physical and/or chemical properties of the patterned surface. A second series of experiments was performed to establish whether the three regions of friction contrast (hill, valley, edge) is a feature of the nanoscale

pattern or arises from another phenomenon. Si/SiO_x, Si/SiO₂, and Au substrates were exposed to similar ion-milling conditions as above (5 keV, 25 μA/cm², 50° from surface normal, MET-ETCH™, Gatan Inc., USA) but instead of the polymer mask, a Super2000 mesh Cu TEM grid (7.5 μm holes separated by 5 μm bars, Canemco Inc., St. Laurent, Canada) was used as a mask. Typical AFM/LFM images of the resulting surfaces (Figure 6) reveal that the areas exposed to the ion-beam exhibit lower friction than do the masked areas. A variation of this experiment was also performed wherein the substrates were first patterned by ion-milling through a TEM-grid-mask, the mask was removed, and the samples were re-exposed to the ion-milling beam for another 60 s. The substrates subjected to this sequential milling show the same LFM characteristics, establishing that increased ion-beam exposure leads to lower LFM-measured friction. The nanoscale roughness induced by the ion-milling process is believed to promote the formation of a thin water layer, and that this water layer gives rise to a lesser friction than that of the unmilled regions. Moreover, the regions corresponding to the feature edges in both the nanoscale and microscale patterned Si/SiO_x samples (Figure 4 and 6a) have a pronounced lessening of the friction.⁴⁵ These results suggest that lower friction is linked to the details of the topography (nanoscale roughness and curvature) of the surfaces.

LFM measured friction is known to be exceptionally sensitive to the thickness of the adsorbed layer of water. For example, a 3 Å thick layer of water has been distinguished by LFM on a mica surface as having lower friction.³¹ It is thus very likely that the observed decrease in friction at the etch edge region arises because it has a thicker water coating than do the adjacent areas.

However, it is also possible that the LFM experiment is generating the observed decrease in friction at the feature edges as a result of larger capillary forces between the tip and sample at the feature edges than at flat regions on the pattern. The possibility that water accumulates to a greater extent at the edges than elsewhere is intriguing, and we are currently investigating the relationships between substrate topologies, surface energy variations, and conformal vs. non-conformal water layers on surfaces, as well as the effects of capillaries formed between the AFM tip and curved versus flat surfaces.

2.4 Conclusions

In summary, the self-assembly of a sacrificial mask with a topologically distinct array of nanometer-sized features has successfully been applied towards pattern-transfer into smooth solid surfaces using a straightforward milling process. The high-fidelity pattern transfer process and removal of the mask were monitored using XPS, AFM and LFM. Friction contrast observed

in the nanopattern is a consequence of the topography introduced to the surfaces. Further work will concentrate on the investigation of non-conformal wetting and the adhesion of water onto the topological features, as well as the application of this pattern-transfer methodology to the generation of topologically and *chemically* distinct features in an array.

Acknowledgments

We thank NSERC Canada for financial support for this research. We also thank Georges Veilleux for assistance with the XPS experiments, Benjamin Smith for helpful discussions regarding the AFM/LFM experiments, and Miriam Rafailovich and Jason Li for discussions related to reference 26.

References

1. Kovacs, G. T. A.; Petersen, K.; Albin, M. *Anal. Chem.* 1996, *68*, 407A-412A.
2. Ogino, T.; Hibino, H.; Homma, Y.; Kobayashi, Y.; Prabhakaran, K.; Sumitomo, K.; Omi, H. *Acc. Chem. Res.* 1999, *32*, 447-454.
3. Lauks, I. *Acc. Chem. Res.* 1998, *31*, 317-324.
4. Semancik, S.; Cavicchi, R. *Acc. Chem. Res.* 1998, *31*, 279-287.
5. Berger, R.; Delamarche, E.; Lang, H. P.; Gerber, C.; Gimzewski, J. K.; Meyer, E.; Güntherodt, H.-J. *Science* 1997, *276*, 2021-2024.
6. Volkmuth, W. D.; Austin, R. H. *Nature* 1992, *358*, 600-602.
7. Figeys, D.; Pinto, D. *Anal. Chem.* 2000, *72*, 330A-335A.
8. Zhu, J.; Eisenberg, A.; Lennox, R. B. *J. Am. Chem. Soc.* 1991, *113*, 5583-5588.
9. Zhu, J.; Lennox, R. B.; Eisenberg, A. *Langmuir* 1991, *7*, 1579-1584.
10. Zhu, J.; Hanley, S.; Eisenberg, A.; Lennox, R. B. *Makromol. Chem.* 1992, *53*, 211-220.
11. Cox, J. K.; Eisenberg, A.; Lennox, R. B. *Curr. Opin. Colloid Interface Sci.* 1999, *4*, 52-59, and references therein.
12. Zhu, J.; Lennox, R. B.; Eisenberg, A. *J. Phys. Chem.* 1992, *96*, 4727-4730.

13. Zhu, J.; Eisenberg, A.; Lennox, R. B. *Macromolecules* 1992, *25*, 6547-6555.
14. Cox, J. K.; Yu, K.; Constantine, B.; Eisenberg, A.; Lennox, R. B. *Langmuir* 1999, *15*, 7714-7718.
15. Spatz, J. P.; Eibeck, P.; Mößmer, S.; Möller, M.; Herzog, T.; Ziemann, P. *Adv. Mater.* 1998, *10*, 849-852.
16. Spatz, J. P.; Herzog, T.; Mößmer, S.; Ziemann, P.; Möller, M. *Adv. Mater.* 1999, *11*, 149-153.
17. Park, M.; Harrison, C.; Chaikin, P. M.; Register, R. A.; Adamson, D. H. *Science* 1997, *276*, 1401-1404.
18. Li, R. R.; Dapkus, P. D.; Thompson, M. E.; Jeong, W. G.; Harrison, C.; Chaikin, P. M.; Register, R. A.; Adamson, D. H. *Appl. Phys. Lett.* 2000, *76*, 1689-1691.
19. Harrison, C.; Park, M.; Chaikin, P. M.; Register, R. A.; Adamson, D. H. *J. Vac. Sci. Technol. B* 1998, *16*, 544-552.
20. Thurn-Albrecht, T.; Steiner, R.; DeRouchey, J.; Stafford, C. M.; Huang, E.; Bal, M.; Tuominen, M.; Hawker, C. J.; Russell, T. P. *Adv. Mater.* 2000, *12*, 787-791.
21. Lammertink, R. G. H.; Hempenius, M. A.; van den Enk, J. E.; Chan, V. Z.-H.; Thomas, E. L.; Vancso, G. J. *Adv. Mater.* 2000, *12*, 98-103.

22. Douglas, K.; Devaud, G.; Clark, N. A. *Science* 1992, *257*, 642-644.
23. Holland, B. W.; Douglas, K.; Clark, N. A. *Mater. Res. Soc. Symp. Proc.* 1994, *330* (Biomolecular Materials by Design), 121-126.
24. Tada, T.; Hamoudi, A.; Kanayama, T.; Koga, K. *Appl. Phys. Lett.* 1997, *70*, 2538-2540.
25. Fritzsche, W.; Böhm, K. J.; Unger, E.; Köhler, J. M. *Appl. Phys. Lett.* 1999, *75*, 2854-2856.
26. Zhu, S.; Gambino, R. J.; Rafailovich, M. H.; Sokolov, J.; Schwarz, S. A.; Gomez, R. D. *IEEE Transactions on Magnetics* 1997, *33*, 3022-3024.
27. Zhu, J.; Eisenberg, A.; Lennox, R. B. *Macromolecules* 1992, *25*, 6556-6562.
28. Silicon substrates were cleaned by soaking for 5 mins in boiling chloroform (Fisher Scientific, Canada, HPLC Grade) / ethanol (Anhydrous, Commercial Alcohols Inc., Canada) (50:50 v/v) solution, followed by ultrasonication for 2 mins.
29. Li, Z.; Zhao, W.; Quinn, J.; Rafailovich, M. H.; Sokolov, J.; Lennox, R. B.; Eisenberg, A.; Wu, X. Z.; Kim, M. W.; Sinha, S. K.; Tolan, M. *Langmuir* 1995, *11*, 4785-4792.
30. AFM and LFM imaging was performed with a large range of applied loads (~20 to 200 nN approximately) using oxide-sharpened silicon nitride tips

(NanoSensors) with a variety of force constants ($k = 0.06, 0.12, 0.32, 0.56$ N/m), and at a scan rate of 1 Hz. Generally LFM contrast was observed for the nano-patterned samples when the load was kept low (less than approximately 80 nN). However, the contrast was (infrequently) observed to reverse such that areas that normally appeared to cause less lateral deflection, appeared to cause more lateral deflection. The cause of this contrast reversal is unclear, however, we suspect that it is related to changes in the ambient relative humidity (typically ~60% relative humidity). Piner et al.³¹ have reported similar humidity effects on the LFM experiment when performed in air.

31. Piner, R. D.; Mirkin, C. A. *Langmuir* 1997, *13*, 6864-6868.
32. Thundat, T.; Zheng, X. Y.; Chen, G. Y.; Warmack, R. J. *Surf. Sci.* 1993, *294*, L939-L943.
33. Binggeli, M.; Mate, C. M. *Appl. Phys. Lett.* 1994, *64*, 415-417.
34. Binggeli, M.; Mate, C. M. *J. Vac. Sci. Technol., B* 1995, *13*, 1312-1315.
35. Sugimura, H.; Okiguchi, K.; Nakagiri, M.; Miyashita, M. *J. Vac. Sci. Technol., B* 1996, *14*, 4140-4143.
36. Crassous, J.; Charlaix, E.; Loubet, J. *Phys. Rev. Lett.* 1997, *78*, 2425-2428.

37. Hu, J.; Xiao, X.-D.; Ogletree, D. F.; Salmeron, M. *Surf. Sci.* 1995, *327*, 358-370.
38. Sedin, D. L.; Rowlen, K. L. *Anal. Chem.* 2000, *72*, 2183-2189.
39. Quon, R. A.; Ulman, A.; Vanderlick, T. K. *Langmuir* 2000, *16*, 8912-8916.
40. Thundat, T.; Zheng, X.-Y.; Chen, G. Y.; Sharp, S. L.; Warmack, R. J.; Schowalter, L. J. *Appl. Phys. Lett.* 1993, *63*, 2150-2152.
41. Fujihira, M.; Aoki, D.; Okabe, Y.; Takano, H.; Hokari, H. *Chem. Lett.* 1996, *7*, 499-500.
42. SiO₂ and Au nanopatterns were also prepared under a variety of milling times (60 to 300s) and the AFM and LFM images presented are consistent for all samples prepared within this range of ion-beam exposure. XPS was used to verify that the SiO₂ and Au layers (114 nm and 200 nm respectively) had not been milled through.
43. The smooth Au films were prepared by first evaporating 200 nm Au onto a clean Si wafer at a rate of 2 Å/s at 5x10⁻⁶ Torr. The Au surface was fixed to a glass slide with epoxy glue, and then pulled off the Si wafer thus exposing a smooth surface of Au. This method is a variation of that described by Stamou et al (ref. 44).
44. Stamou, D.; Gourdon, D.; Liley, M.; Burnham, N. A.; Kulik, A.; Vogel, H.; Duschl, C. *Langmuir* 1997, *13*, 2425-2428.

45. The friction contrast observed at the edges of the features was only observed for the Si/SiO_x samples, and has not been observed in the Si/SiO₂ or Au samples under the experimental conditions explored. Furthermore, UV/ozone cleaned and oxide-sharpened AFM tips are required to resolve these edge effects.

Connecting Text for Chapter 3:

Preparation of Nanoscale Au Islands in Patterned Arrays

This Chapter describes the preparation of patterned features in a nanoscale array which are chemically distinct from the substrate. Gold-coated silicon and mica substrates are applied to the methodology described in Chapter 2, resulting in distinct islands or nanoparticles of gold (gold “islands”) in arrays predefined by the diblock copolymer surface micellar film structure. The morphology of the underlying gold film, and the choice of substrate are found to play a significant role in determining the final structure of the patterned features.

Atomic force microscopy and field emission (gun) scanning electron microscopy (FEGSEM) were used to characterise the final structures. Tracking the removal of gold in between the patterned features by FEGSEM, energy dispersive spectroscopy (EDS), as well as comparison to the FEGSEM imaging of patterned gold substrates allow the assignment of contrast in the FEGSEM images to arise from Au/Si or Au/Mica chemical contrast. The determination of chemically distinct nanostructures directly leads to the studies pursued in Chapters 4 and 5.

This Chapter presents an important extension of the methodology presented in Chapter 2, by offering a novel route to nanoparticle array

synthesis which is independent of the nanoparticle self-assembly properties. As such, it serves as an excellent example of surface patterning on the nanometer length scale. In addition, Appendix 2 provides information related to the methodology described in this paper.

Chapter 3

Preparation of Nanoscale Au Islands in Patterned Arrays*

** This paper was reproduced with permission from Langmuir 2003, 19(22), 9097-9100. Copyright 2002 American Chemical Society. It is coauthored by R. Bruce Lennox. The text below is a verbatim copy of the published paper.*

Abstract

A facile method is presented for generating quasihexagonal two-dimensional (2-D) arrays of nanoscale gold islands. The topological contrast intrinsic to Langmuir-Blodgett (LB) monolayer films of surface micelles, self-assembled from an amphiphilic diblock copolymer, was used as a stencil mask. Argon ion-milling of gold-coated silicon and mica substrates which had been covered with these ultra-thin masks resulted in arrays of ~25 nm diameter gold islands supported on patterned silicon pillars, or gold islands directly adhered to a mica substrate. The resulting arrays were characterized by atomic force microscopy (AFM) and field emission gun scanning electron microscopy (FEGSEM).

3.2 Introduction

The fabrication of chemically patterned surfaces, with structural parameters < 100 nm, is a topic of great interest and demand given the

interest in applying nanoscience and nanotechnology in the next generation of electronic and optical devices, and catalysis. Metallic and semiconducting nanoparticles have unique size-dependent properties which are further influenced by their arrangement in space with respect to other nanoparticles and the surrounding matrix.¹⁻⁵ However, there are relatively few methods to control the fabrication and arrangement of metal islands or nanoparticles on surfaces. Because electron beam and photolithography are resolution-limited by Rayleigh diffraction, there has been increasing interest in using masks which self-assemble from molecular building blocks. Diblock copolymers are known to self-assemble into a variety of nanometer-scale organized morphologies based on the surface free energy and volume fraction of each block.⁶ Building on our experience with the self-assembly of symmetric, amphiphilic diblock copolymers at the air-water interface,^{7,8} we have recently used these films as stencil masks to create large arrays of ordered nanostructures on surfaces.⁹ These ultra-thin masks have intrinsic topology (dependent upon the choice of block copolymer), ranging from about 10 - 100 nanometers in width and spacing. Here, we report the application of the self-assembled mask formed from polystyrene-*b*-poly-2-vinylpyridine (PS-P2VP) towards the generation of gold island arrays on silicon and mica substrates.

Ordered 2D-arrays of metal islands or nanoparticles are much sought after. We define nanoscale metal islands here as structures which are generated in-situ (using a mask technique) and fixed to a surface. In contrast, nanoparticles are chemically synthesized ex-situ and are subsequently deposited on the surface. Methods which yield patterns of metal islands are inevitably more general than the (directed) self-assembly of nanoparticles, where in the latter case the colloidal properties and ligand-stabilizers control the dimensions of the final array. Van Duyne and coworkers^{10,11} have demonstrated the versatility of nanosphere particle arrays as evaporation masks. Metal islands of various shapes and sizes are created in this process, where silver is deposited into the holes generated in a close-packed lattice of nanospheres. Porous anodic aluminum oxide films have also been used as evaporation masks in a variety of ways to create metal island arrays with controlled dimensions.^{12,13} Another type of mask system, based on block copolymer self-assembly, has been attracting interest for its capability to independently design the structural and ordering parameters of dot arrays. Möller et al.¹⁴ have made arrays of Au nanoparticles (up to 15 nm) by selective derivitization of PS-PVP reverse micelles with HAuCl_4 and subsequent reduction of the core to Au(0). Monolayer films of these micelles deposited from solution are generated and subsequent reactive ion etching of

the polymer yields the bare Au nanoparticles. Others^{15,16} have also made metal islands, on the order of 10-20 nm in diameter, using selective chemistry on one component of a block copolymer mask resulting in nanoporous evaporation masks. Several groups¹⁷⁻¹⁹ have explored the self-assembly of polyferrocenylsilane-*b*-organic (polystyrene, polydimethylsiloxane, polyisoprene, etc.) diblock copolymers, making organometallic dots in an organic matrix which can be removed by reactive ion etching.¹⁹

In the system used here, the surface micelles formed from polystyrene(510)-*b*-poly-2-vinylpyridine(480) have PS cores with average diameter 50 ± 5 nm, thickness 4.5 ± 0.5 nm and spacing 110 ± 10 nm on a P2VP continuum (Figure 1). These micelles self-order into quasihexagonal close-packed domains of $\sim 1 \mu\text{m}^2$. The main design capability of the block copolymer system stems from the fact that the micelles have aggregation numbers typically in the range of 100-125, which means that both the diameter of the circular domains and the spacing between them are determined by the block lengths chosen. An additional advantage offered by the air-water assembly of the polymer is that the micelle topology is essentially determined by the relative difference in hydrophilicity of the two blocks instead of more subtle factors such as χ differences. The intrinsic topology of our mask system also avoids the use of selective chemistry on

one of the two blocks in order to transfer a pattern to the substrate, thus making a variety of amphiphilic block copolymers useful in this methodology (i.e. polystyrene-*b*-polymethacrylates, -polyacrylates, -poly(ethylene oxide), and -poly(dimethyl siloxane)).^{20,21} Furthermore, the use of a chemically unselective etch process for pattern transfer (i.e. Ar ion beam milling) makes this methodology a relatively inexpensive and simple means of generating nanoscale metal island arrays on a variety of (semi-)conducting and insulating substrates.

3.3 Experimental Section

Langmuir-Blodgett monolayer films of ordered surface micelles were prepared as previously described.⁹ 80-100 μL of a 0.5 mg/ml chloroform solution of polystyrene(510)-*b*-poly-2-vinylpyridine(480) ($M_w/M_n = 1.06$, Polymer Source Inc., Dorval, Canada) was evenly spread in ca. 5 μL drops onto a $18\text{M}\Omega$ water surface (23 °C, KSV 3000). 20 min elapsed after spreading before compression to the desired surface density began. The Langmuir film was compressed at a rate of 5 mm/min to a surface pressure of 2 mN/m, and then transferred at 1 mm/min to clean²² substrates prepared in two ways. In the first, a 0.5 nm Ti adhesion layer followed by a 20 nm film of Au was sputter-deposited (20W, 6mTorr Ar) onto clean silicon²² with a native oxide layer (Si/SiO_x). In the second, a substrate consisting of a 10 nm Au film

sputter-deposited on freshly-cleaved mica was used. Sputter-deposited Au was used because of its very low rms roughness (≤ 0.5 nm) over cm^2 areas and excellent surface coverage for thin films, with the absence of voids as observed for evaporated thin (~ 10 nm) Au films. The resulting substrates clearly show that the topology of the PS-P2VP mask is well-resolved above the roughness of the polycrystalline gold layer (Figure 2).

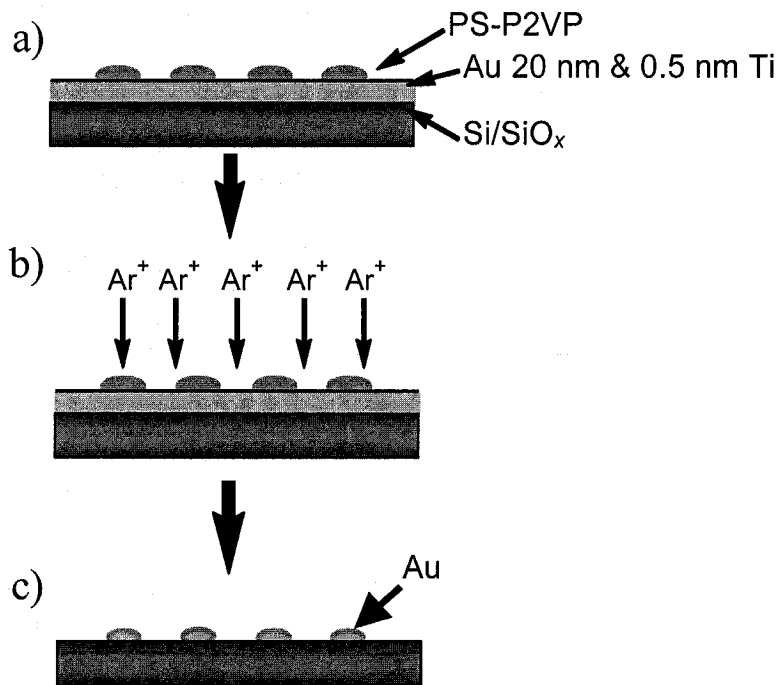


Figure 1: Schematic cross-sectional view of the pattern-transfer methodology.

a) Film of surface micelles (round PS domains on a ~ 1 nm thin PVP layer) covering a substrate consisting of a thin gold film adhered to Si/SiO_x with a 0.5 nm Ti layer. b) Ar⁺-milling unselectively removes material from the

surface, transferring the topology of the mask. c) Ar⁺-milling is stopped once the gold located between PS-masked domains has been removed, leaving an array of Au islands on Si/SiO_x.

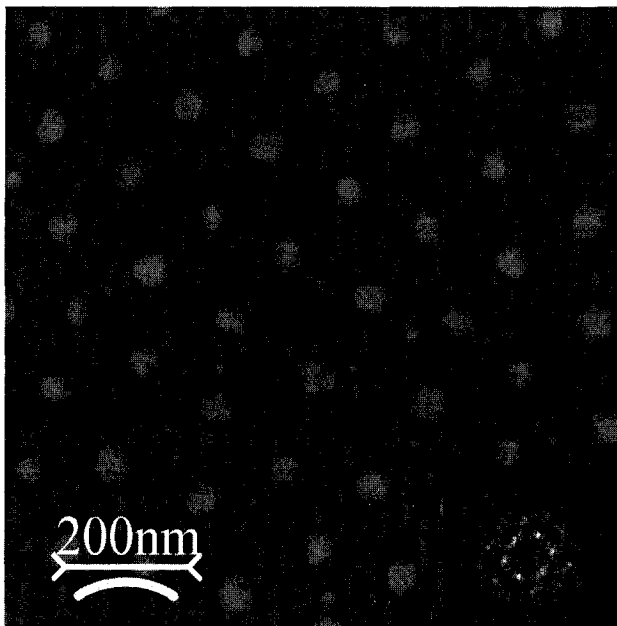


Figure 2: AFM image of a PS-P2VP LB-film transferred to a 20 nm film of sputter-deposited Au onto 0.5 nm Ti and Si/SiO_x (as schematically shown in Figure 1a) with corresponding FFT (inset).

The array of Au islands was generated by Ar⁺ milling of the LB film-coated substrates until the gold, in the regions not masked by the PS domains of the surface micelles, is fully removed (Figure 1). Typically, the substrates were exposed to a 6 keV Ar⁺ ion-beam (3.5 μA/cm², samples rocked at 40°/s from 0-50° from surface normal, 60 rpm, MET-ETCH, Gatan Inc.) for 300s (in the case of the 20 nm Au film) and 180 s (for the 10 nm Au

film). Removal of the Au to make a discontinuous island film was monitored ex-situ with a field emission gun scanning electron microscope (FEGSEM, Hitachi S-4700). The etched substrates were subsequently imaged by tapping-mode atomic force microscopy (AFM, Park Scientific Instruments AutoProbe CP) using silicon nitride Ultralevers™ ($f_0 \sim 140$ kHz, ThermoMicroscopes).

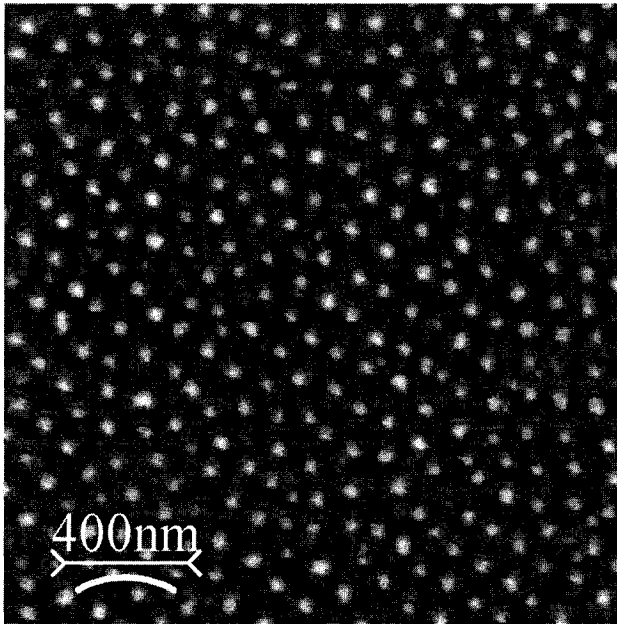


Figure 3: AFM image of Au islands on Si/SiO_x obtained after 300s of Ar⁺-milling through the sample shown in Figure 2.

3.4 Results and Discussion

The AFM image of the gold islands on Si/SiO_x substrate (Figure 3) shows that the mask features have been transferred to the substrate resulting

in 45 ± 5 nm diameter features separated by 110 ± 10 nm. The height of the features, however, is significantly larger than the original mask owing to the faster ion-milling rate of Au compared to Si (approximately 4x faster at 5 keV).²³ The 4.5 nm vertical contrast of the mask profile thus increases to 13 ± 2 nm in the transferred pattern.

Figure 4 shows the FEGSEM secondary electron images,²⁴ obtained at 3kV, of the PS-P2VP film on the Au/Ti/SiO_x/Si substrate before and after ion-milling. The PS domains in Figure 4a appear as dark spots indicating that the yield of secondary electrons in these regions is suppressed. In contrast, the gold islands shown in Figure 4b appear as bright spots on the silicon substrate as a result of the greater secondary emission yield of gold compared to that of silicon.²⁵ We assign the FEGSEM contrast observed in Figure 4b to the difference in secondary emission yields, and not to topology, for two reasons. Firstly, the FEGSEM image shown in Figure 4c is of a (continuous) gold substrate patterned via the same PS-P2VP polymer methodology, such that all of the polymer has been removed and only the patterned topological features in the gold surface remain.²⁶ The resulting *ca.* 10 nm tall gold features appear darker compared to the rest of the gold surface.

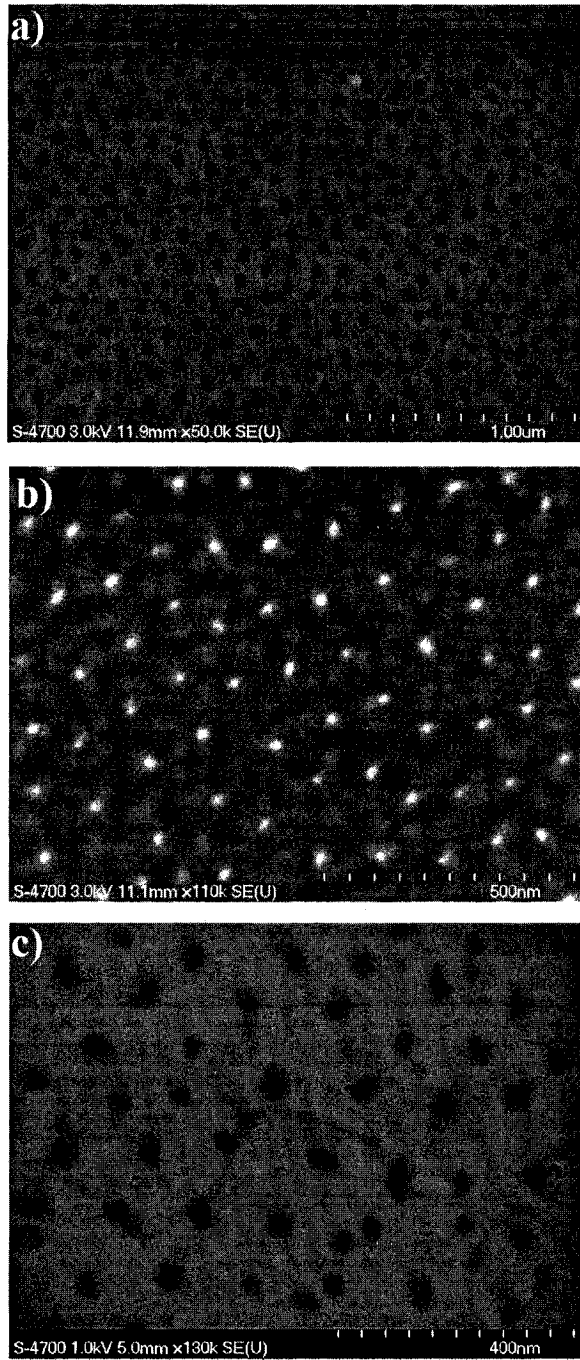


Figure 4: FEGSEM images of a) PS-PVP on Au/Ti/SiO_x/Si substrate. b) Au islands on Ti/Si/SiO_x substrate. c) Au “islands” on Au substrate.

Secondary electrons are especially sensitive to the work function, the distance from the surface, as well as topology.²⁷ The relatively small topology of the pattern in Figure 4c evidently leads to a *reduction* in the number of secondary electrons that escape from the surface compared to the flat gold regions. While further investigation is needed to elucidate the factors responsible for this contrast, they ultimately outweigh the more commonly observed topology effects in SEM where taller, rounded features appear brighter. Secondly, we have not observed the topological pattern on Si/SiO_x substrates in FEGSEM using the same imaging conditions. The pure topology contrast of patterned silicon is not a significant contributor to the contrast observed in Figure 4b.

The average diameter of the gold islands in Figure 4b is 28 ± 4 nm, less than the diameter of the PS cores of the surface micelle mask (50 ± 5 nm). Some loss in the pattern transfer fidelity was expected due to the irregular nature of the polycrystalline gold film and the use of relatively unselective ion-milling conditions compared to reactive ion etching. The discrepancy in diameter of the Au islands between the FEGSEM and AFM measurements implies that the Au domains are located on top of ~ 10 nm tall Si/SiO_x pillars. To confirm this, the gold was removed using aqua regia (concentrated HNO₃ : concentrated HCl : H₂O, 1:3:6 vol. %) for 20 mins followed by rinsing with

water, and drying under a gentle stream of nitrogen gas. AFM measurement of the remaining surface (Figure 5) revealed an array of pillars 12 ± 2 nm high. This establishes that the etching process indeed produces Si/SiO_x pillars as well, and that Au islands are approximately 4 nm (± 1 nm) thick in gold (Figure 7a).

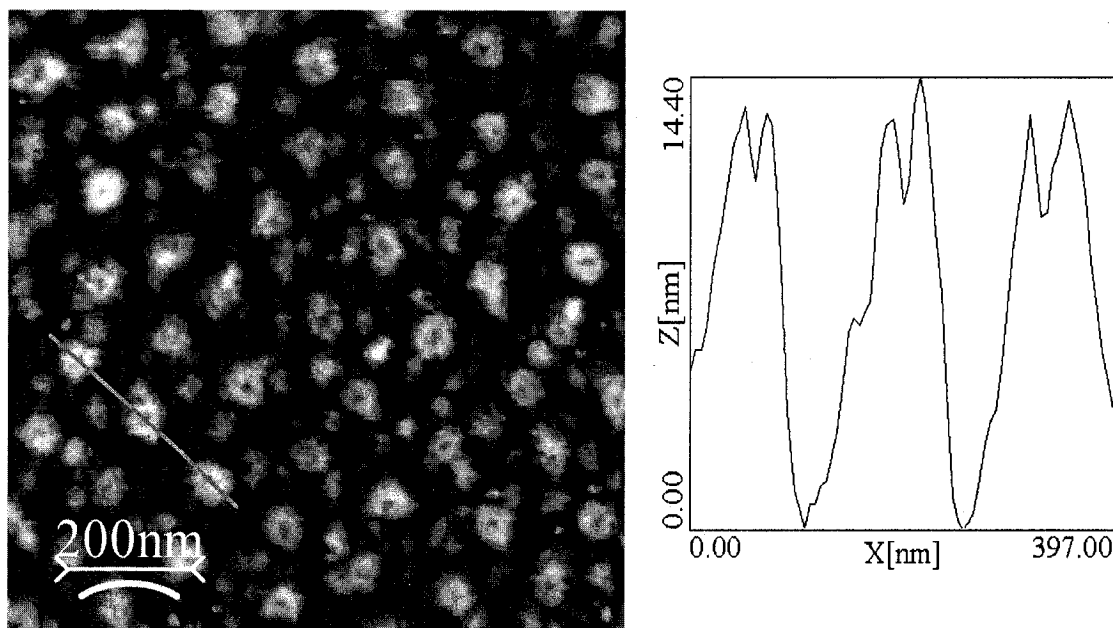


Figure 5: AFM image (left) and line scan profile (right) of the Au island sample on Si/SiO_x (as shown in Figure 3) after dissolution of the Au in aqua regia for 20 mins. Pits on the tops of the patterned SiO_x pillars correspond to the ~ 30 nm Au domains and are ~ 4 nm deep.

Figure 6a shows the FEGSEM image of gold islands of 23 ± 5 nm diameter formed on a mica substrate. The AFM image (Figure 6b) reveals features with 10 ± 1 nm height.²⁸ In contrast to the pattern of Si/SiO_x pillars generated

upon dissolution of the gold islands in aqua regia (Figure 5), no features remain on mica after treatment with aqua regia. This is consistent with our observations of zero pattern-transfer into mica when a mica substrate coated with the PS-P2VP mask is ion-milled. Mica is highly refractory towards the Ar^+ milling conditions we use. The gold islands therefore are formed directly on the flat mica substrate and are not supported on nanometer-scale pillars of the substrate, as seen in the Si/SiO_x case (Figure 7).

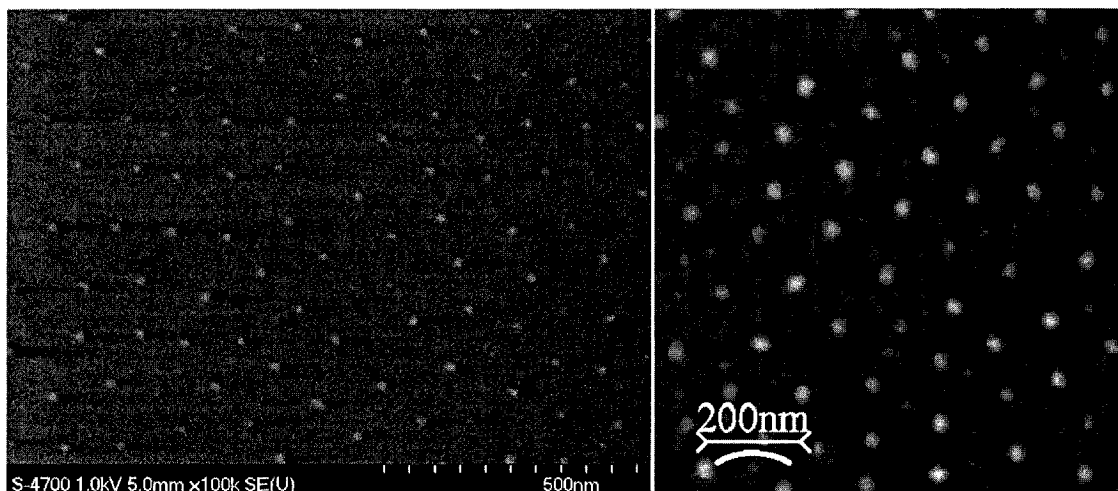


Figure 6: FEGSEM (left) and AFM (right) images of Au islands on mica. The small (< 4 nm) particles randomly located between the patterned Au domains (only visible in the AFM image) are most likely remnant Au particles left behind after the ion-milling process.

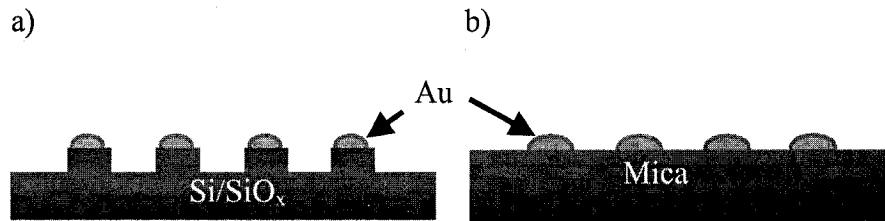


Figure 7: Schematic cross-sectional view of a) Au islands formed on a Si/SiO_x substrate and b) Au islands formed on a mica substrate.

3.5 Conclusions

In summary, quasihexagonal (2D) arrays of nanoscale gold islands have been generated using Langmuir-Blodgett (LB) monolayer films of surface micelles self-assembled from an amphiphilic diblock copolymer used as stencil masks. Straightforward Ar⁺-milling of gold-coated silicon and mica substrates covered with these ultra-thin masks results in arrays of ~25 nm diameter gold islands supported on patterned silicon pillars, or directly adhered to a mica substrate. Further work will concentrate on the optical and electrical properties of these unique gold structures situated on both semiconducting (Si/SiO_x) and insulating and optically transparent (mica) substrates.

3.6 Acknowledgements

We thank NSERC Canada for financial support for this research. We also thank Robert Gagnon for assistance with preparation of the gold films, Dr. S.

Kelly Sears and Prof. Raynald Gauvin for helpful discussions regarding the FEGSEM experiments.

References

1. Kreibig, U.; Vollmer, M. *Optical Properties of Metal Clusters*; Springer-Verlag, 1995; Vol. 25.
2. Murray, C. B.; Kagan, C. R.; Bawendi, M. G. *Annu. Rev. Mater. Sci.* **2000**, *30*, 545-610.
3. Alivisatos, A. P. *J. Phys. Chem.* **1996**, *100*, 13226-13239.
4. El-Sayed, M. A. *Acc. Chem. Res.* **2001**, *34*, 257-264.
5. Coe, S.; Woo, W.-K.; Bawendi, M. G.; Bulovic, V. *Nature* **2002**, *420*, 800-803.
6. Bates, F. S.; Fredrickson, G. H. *Annu. Rev. Phys. Chem.* **1990**, *41*, 525-557.
7. Zhu, J.; Lennox, R. B.; Eisenberg, A. *J. Phys. Chem.* **1992**, *96*, 4727-4730.
8. Cox, J. K.; Eisenberg, A.; Lennox, R. B. *Curr. Opin. Colloid Interface Sci.* **1999**, *4*, 52-59, and references therein.
9. Meli, M.-V.; Badia, A.; Grütter, P.; Lennox, R. B. *Nano Lett.* **2002**, *2*, 131-135.
10. Hulteen, J. C.; Van Duyne, R. P. *J. Vac. Sci. Technol. A* **1995**, *13*, 1553-1558.

11. Hulteen, J. C.; Treichel, D. A.; Smith, M. T.; Duval, M. L.; Jensen, T. R.; Van Duyne, R. P. *J. Phys. Chem. B* **1999**, *103*, 3854-3863.
12. Masuda, H.; Yasui, K.; Nishio, K. *Adv. Mater.* **2000**, *12*, 1031-1033.
13. Almawlawi, D.; Bosnick, K. A.; Osika, A.; Moskovits, M. *Adv. Mater.* **2000**, *12*, 1252-1257.
14. Spatz, J. P.; Mössmer, S.; Hartmann, C.; Möller, M.; Herzog, T.; Krieger, M.; Boyen, H.-G.; Ziemann, P.; Kabius, B. *Langmuir* **2000**, *16*, 407-415.
15. Shin, K.; Leach, K. A.; Goldbach, J. T.; Kim, D. H.; Jho, J. Y.; Tuominen, M.; Hawker, C. J.; Russell, T. P. *Nano Lett.* **2002**, *2*, 933-936.
16. Park, M.; Chaikin, P. M.; Register, R. A.; Adamson, D. H. *Appl. Phys. Lett.* **2001**, *79*, 257-259.
17. Massey, J. A.; Power, K. N.; Winnik, M. A.; Manners, I. *Adv. Mater.* **1998**, *10*, 1559-1562.
18. Li, W.; Sheller, N.; Foster, M. D.; Balashis, D.; Manners, I.; Annis, B.; Lin, J.-S. *Polymer* **2000**, *41*, 719-724.
19. Lammertink, R. G. H.; Hempenius, M. A.; van den Enk, J. E.; Chan, V. Z.-H.; Thomas, E. L.; Vansco, G. J. *Adv. Mater.* **2000**, *12*, 98-103.

20. Li, S.; Hanley, S.; Khan, I.; Varshney, S. K.; Eisenberg, A.; Lennox, R. B. *Langmuir* **1993**, *9*, 2243-2246.
21. Cox, J. K.; Yu, K.; Eisenberg, A.; Lennox, R. B. *Phys. Chem. Chem. Phys.* **1999**, *1*, 4417-4421.
22. Substrates were cleaned by soaking for 5 min in boiling chloroform (Fisher Scientific, Canada, HPLC Grade)/ethanol (Anhydrous, Commercial Alcohols Inc., Canada) (50:50 v/v) solution, followed by ultrasonication for 2 mins.
23. *Calculation of Sputter Etch Rates*; Fisons Instruments plc., Technical Document TD#950203.
24. All images shown in this paper were obtained with a sample 0°-tilt angle, and collected in the upper detector (secondary electron detector).
25. *CRC Handbook of Chemistry and Physics*; 83rd ed.; CRC Press LLC, 2002.
26. A 200 nm thick layer of Au was evaporated onto mica at a rate of 1.2 Å/s. The PS-P2VP film was LB-deposited onto the gold surface, and ion-milled for 180s. The removal of polymer was monitored by X-ray photoelectron spectroscopy (XPS) as per reference 9.

27. Goldstein, J. I. *Scanning Electron Microscopy and X-ray Microanalysis: a text for biologists, materials scientists, and geologists*; 2nd ed.; Plenum Press: New York, 1992.
28. The AFM-measured diameter of the Au islands was 34 (\pm 5) nm, well within the range of tip broadening effects for a \sim 10 nm diameter Ultralever™ tip. There may also be some contribution to the difference between the AFM and FEGSEM-measured diameters of Au islands on mica (not silicon) from the calibration of the AFM scanning motion.

Connecting Text for Chapter 4:

The Wetting of Nanopatterned Surfaces

This Chapter describes the characterisation of the nanopatterned surfaces (made by methods described in Chapters 2 and 3), in terms of the surface energy they present, and the properties of a water droplet that comes into contact with such a surface. The measurement of the wetting of nanopatterned surfaces, derivatized with self-assembled monolayers, is performed and compared to that of their smooth, or unpatterned counterparts. The results are discussed in light of using nanoscale patterning to create *functional* surfaces (self-cleaning, anti-adhesive surfaces).

This Chapter therefore serves as an important fundamental characterisation of these novel surfaces. Contact angle measurements of nanopatterned surfaces are rarely performed because other patterning methodologies capable of sub-100 nm resolution are typically limited to small patterned areas (1-2 μm^2). However, the block copolymer mask methodology employed here creates the opportunity for this measurement as $\sim 1\text{cm}^2$ areas of homogeneously nanopatterned surfaces are accessible.

Chapter 4

The Wetting of Nanopatterned Surfaces

4.1 Introduction

The formal study of surface energy and wetting phenomena was reported in 1612 by Galileo, whom many would consider the father of the field. Galileo noticed that when a flat thin solid (such as gold leaf) was placed on a liquid of lesser density (such as water), the solid would not only float on the water surface, but also bend it such that the top surface of the solid lay below the surface of the water (Figure 4-1).^{1,2} Although Galileo did not invoke the concept of surface tension, he introduced the idea that some forces other than gravity and buoyancy were responsible for this phenomenon.

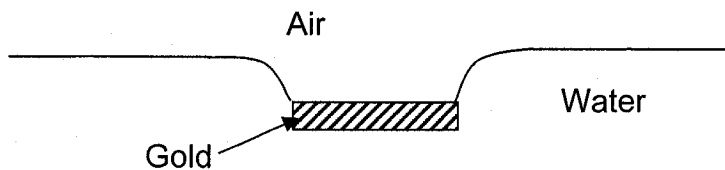


Figure 4-1: Side view of a flat thin sheet of gold at an air/water interface.

Nearly 200 years later, Thomas Young introduced a framework for describing surface energy phenomena with equation 4-1:

(Young's equation) $\gamma_{sv} = \gamma_{sl} + \gamma_{lv} \cos\theta$ Equation 4-1

where γ is the surface tension (or surface free energy), and the subscripts sv, sl, and lv refer to the solid-vapour, solid-liquid, and liquid-vapour interfaces, respectively.³ Equation 4-1 originates from the balance of forces at the interface of a liquid drop on a solid surface and the surrounding vapour environment (Figure 4-2).

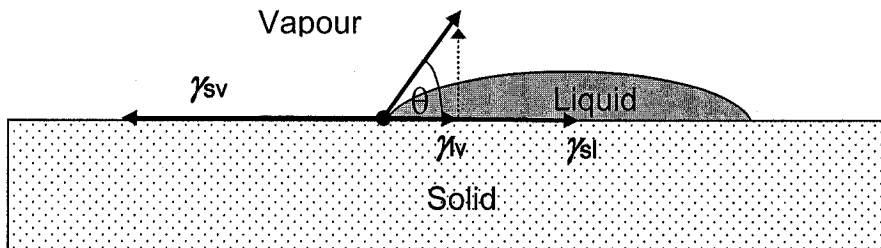


Figure 4-2: Drop of liquid on a solid showing the balance of forces about the 3-phase line.

Dupré further developed the concept of surface energy as the free energy per unit area (equivalent to the force per unit length) and related it in terms of the classical thermodynamic notion of work (W)⁴. When two bodies i and j (of unit area) are brought together reversibly, the free energy ΔG_{ij} is given by the Young-Dupré equation (equation 4-2):

$$\Delta G_{ij} = \gamma_{ij} - \gamma_i - \gamma_j = -W_{ij} \quad \text{Equation 4-2}$$

When $i = j$, then W_{ij} represents the work of cohesion, whereas when $i \neq j$, W_{ij} is the work of adhesion.

Equations 4-1 and 4-2 are based on the assumptions that the solid has only atomic roughness, is chemically homogeneous, stable, rigid, and free of adsorbates from the vapour or liquid phases.¹ Given these inherent limitations, estimates of the true equilibrium contact angle are made by measuring the angle of a recently advanced or receded drop on the surface. The true equilibrium contact angle (θ) is thought to lie between the two (i.e., $\theta_{\text{rec}} < \theta < \theta_{\text{adv}}$). In practice, the advancing/receding process is rarely completely reversible, and an appreciable hysteresis ($\Delta\theta = \theta_{\text{adv}} - \theta_{\text{rec}}$) can be observed. The hysteresis is typically on the order of 3-10°, but can be as low as ~1° for very well defined surfaces.⁵

Roughness is known to have significant effects on the wettability and hysteresis of contact angle measurements on surfaces. Wenzel's equation (equation 4-3) accounts for the effect of roughness on the apparent contact angle of a surface by accounting for the increased area of contact^{6,7}:

$$\cos \theta_w = r \cos \theta \quad \text{Equation 4-3}$$

where θ_w is the apparent or measured contact angle, θ is the contact angle of the smooth surface, and r is the ratio of the total area in contact with the

liquid to the projected area. In some cases, roughness can lead to the incomplete wetting of the surface such that the liquid does not sample the entire surface area. In this case, the drop wets a composite or chemically heterogeneous surface, made of both solid and vapour components (Figure 4-3b). Such wetting is typically described using Cassie's equation⁸ (equation 4-4) for heterogeneous surface which reduces to the Cassie-Baxter equation (equation 4-5) for the case where the second surface component is the vapour⁹:

$$\cos \theta_c = \sum f_i \cos \theta_i \quad \text{Equation 4-4}$$

$$\cos \theta_{cb} = -1 + f(\cos \theta + 1) \quad \text{Equation 4-5}$$

where f is the fraction of the area of the solid in contact with the drop to the projected area.

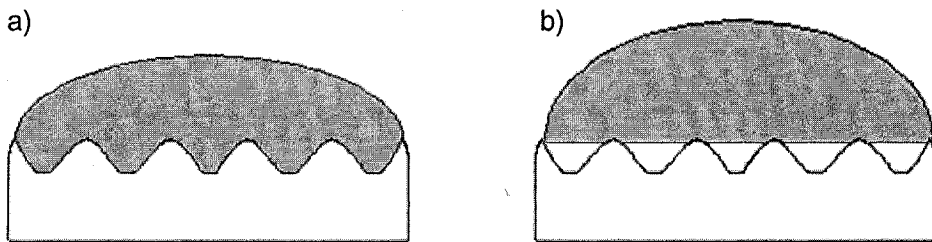


Figure 4-3: Wetting of rough surfaces modelled by (a) the Wenzel equation and (b) the Cassie equation.

Substrate roughness is investigated in many systems for its far-reaching effects on wetting and adhesion phenomena for non-“ideal” yet exceptionally

functional surfaces. Examples of such surfaces include water-repellent insect legs such as those of the water strider¹⁰, the setae on the feet of gravity-defying geckos¹¹, as well as the engineering of self-cleaning glass¹² and “non-stick” water¹³. Rooted in such surfaces is the (de)wetting property called *ultrahydrophobicity*. This is a property of surfaces whose water-surface contact angle $>150^\circ$ (and approaching 180°). Flat surfaces have not exhibited contact angles much beyond 120° due to chemical composition alone, but have been shown to become ultrahydrophobic (or ultrahydrophilic) when surface topography is introduced. Surface roughness is also intimately related to the (contact angle) hysteresis ($\Delta\theta$)^{14,15}. In the complete (Wenzel) wetting scenario, hysteresis is expected to increase with an increase in roughness until the composite (Cassie) wetting occurs with a corresponding reduction in hysteresis. Very small hysteresis in the wetting of composite surfaces has consequences in the dynamic wettability of surfaces¹⁶. In particular, it is believed to give rise to the anti-adhesive properties attributed to surfaces where non-wetting drops roll off the surface with the application of a trivial amount of force (i.e. a low tilt angle). The combination of ultrahydrophobicity and anti-adhesive properties renders a surface *superhydrophobic*. A common example of superhydrophobicity is the self-cleaning Lotus leaf¹⁷. Micron-scale roughness has been demonstrated to

cause superhydrophobicity and is understood to be *via* heterogeneous wetting described by the Cassie equation^{12,13,18-20}. There are several accounts of the wetting of surfaces with “hierarchical roughness” where surfaces have nanoscale roughness superimposed onto micron-scale surface features²¹⁻²⁴. There have been, however, fewer demonstrations of superhydrophobicity of purely nanostructured surfaces. Badyal and coworkers have characterized the superhydrophobic behaviour of polybutadiene films treated with a CF₄ plasma to arise in part from lowering of surface energy *via* introduction of -CF_n groups and in part from the surface roughening on the order of *ca.* 50 nm (rms roughness of a 50 μm x 50 μm area)²⁵. Gleason and coworkers have demonstrated the superhydrophobic character of a carbon nanotube array (50 nm diameter, 2 μm height, random spacing) grown perpendicularly to the Si surface²⁶. Recently, Yang and coworkers have demonstrated excellent dynamic electrical control on the wetting behaviour of nanostructured surfaces (350 nm diameter, 7 μm high posts, spaced 1-4 μm apart) ranging from ultrahydrophilic to superhydrophobic²⁷. On the other hand, there have been several accounts in the literature where nanoscopic roughness has a minimal effect on the contact angle²⁸⁻³¹. Clearly, the extent to which nanoscale roughness can

affect hydrophobicity, especially for structures with at least one dimension < 100 nm, has not been fully explored.

4.2 Experimental Section

Nanopatterned Au and Si/SiO_x substrates were prepared as per the procedures described in Chapter 2^a. Freshly patterned Au substrates were immersed in 1 mM ethanolic thiol (*n*-C₅H₁₁SH and *n*-C₁₈H₃₇SH) solution for 1 hour, rinsed with approximately 250 ml of anhydrous ethanol, and dried under a stream of nitrogen gas. Nanopatterned substrates were compared with their “flat”, *unpatterned* counterparts: a thiolated flat gold substrate and an ion-milled clean³² Si/SiO_x substrate. Si/SiO_x substrates which were not exposed to the argon ion beam were also cleaned and assessed in order to compare to the ion-milled Si/SiO_x sample. Freshly formed template-stripped gold replicas³³ were used as flat gold substrates and were immediately placed in 1 mM ethanolic thiol solution for 1 hour followed by rinsing and drying as previously described. Clean Si/SiO_x substrates were exposed to an Ar⁺ beam under the same conditions as used in the pattern-transfer step in the nanopatterning methodology (6.5 keV, 12μA, 180s). Lastly, patterned Au

^a The procedures in Chapter 2 were followed except that the ion-milling conditions were changed in order to use an apparatus capable of ion-milling a 1cm-diameter spot suitable for contact angle measurements (6 keV, 3.5 μA/cm², samples rocked at 40°/s from 0 to 50° from the surface normal, 60 rpm, MET-ETCH, Gatan, Inc.).

island samples were prepared as described in Chapter 3, and cleaned by first exposing to in UV/ozonolysis conditions^{34,35} for 1 hour followed by rinsing with water, ethanol, degreased, and dried under a stream of nitrogen gas. After cleaning, the Au/Si samples were immersed in 1 mM ethanolic alkanethiol (*n*-C₅H₁₁SH) solution for 1 hour followed by rinsing with approximately 250 ml of ethanol (anhydrous) and dried under a stream of nitrogen gas.

The resulting surfaces were imaged using tapping-mode atomic force microscopy (AutoProbe CP, Park Scientific Instruments) using silicon cantilevers ($f_0 \sim 300$ kHz, Asylum Research) in order to determine the size and shape of the patterned features.

Contact angles were measured using the sessile drop method in a home-built humidity chamber³⁶, placed on a levelled, temperature-controlled stage. The measurements were made under a relative humidity and temperature of 45(2)% and 25(1)°C respectively. Advancing (θ_a) and receding (θ_r) contact angle measurements were made by placing a ca. 5 μ l drop of Ultrapure MilliQ (18M Ω) water on the surface with a syringe, subsequently adding/removing ~ 1 μ l quantities to/from the drop, and retracting the needle before measurement. A video capture image of the drop was made using a CCD camera within 5 s of removing the needle. The contact angle was determined by fitting the drop shape to that of a spherical

cap (Multiskop, Optrel GbR). Values reported are the average of at least 3 replicate measurements made on multiple drops on two identically prepared surfaces, with the exception of the Au-Si island patterns which exhibit unique topological features and hence could not be averaged (see Table 4.1).

4.3 Results and Discussion

Figure 4.4 shows a typical AFM image of the nanopatterned Au surface described above, with its flat counterpart (an *unpatterned* Au surface). Table 4.1 lists the dimensions of the features measured from representative images such as those depicted in Figure 4-4 and Figure 4-5, and the respective values for r and f as defined by the Wenzel and Cassie equations.

The advancing contact angles measured for the flat substrates were used to estimate the contact angle of the nanopatterned substrates using equations 4.3 and 4.5. Finally, the Wenzel contact angle for the Au-Si island patterns was determined using the advancing contact angles of the flat Si/SiO_x and Au surfaces (equation 4-6) for a composite surface.

$$\cos \theta' = f' \cos \theta_{Au} + (1 - f') \cos \theta_{Si} \quad \text{Equation 4-6}$$

where f' is the ratio of the Au island surface area to the total surface area.

The measured and calculated contact angles are summarized in Table 4.2.

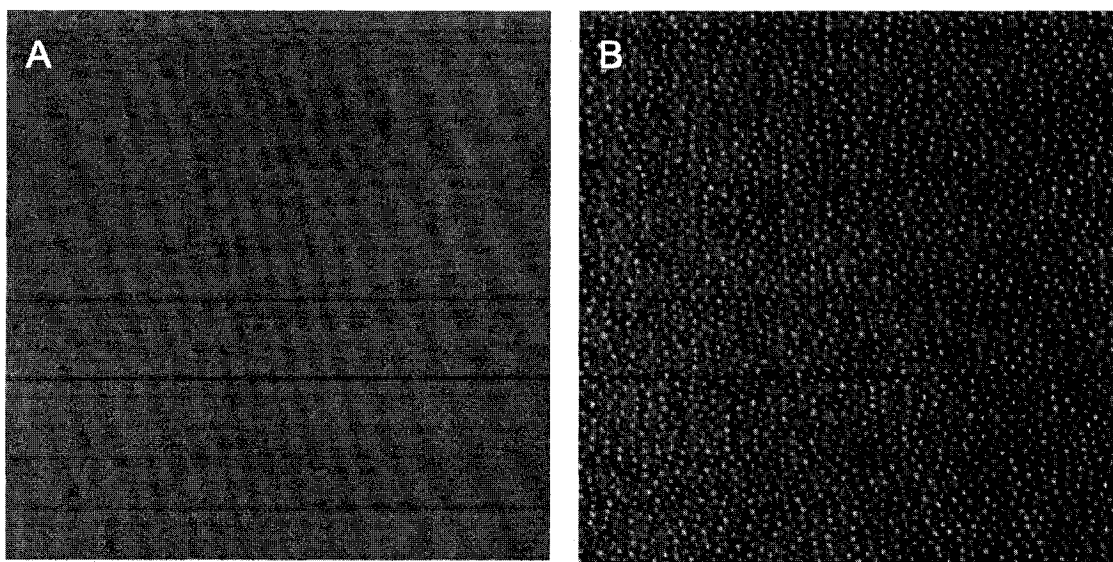


Figure 4-4: 5 μm x 5 μm AFM images of (A) flat and (B) nanopatterned template-stripped Au "replicas". Both images are displayed on a height scale of 0-20 nm.

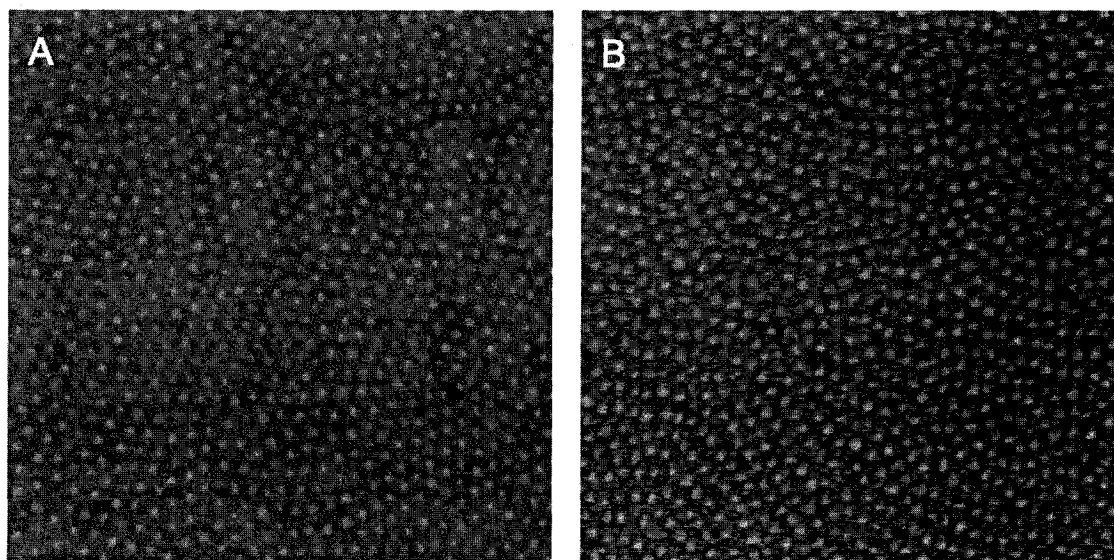


Figure 4-5: 3.5 μm x 3.5 μm AFM images of (A) nanopatterned Si/SiO_x and (B) Au islands (Au-Si-2). Both images are displayed on a height scale of 0-20 nm.

Table 4.1: Measured (average) values of the features shown in Figure 4-4 and Figure 4-5. Standard deviations are in brackets.

| Sample | Height ^a (nm) | Maximum Diameter ^b (nm) | Spacing ^c (nm) | r_d | f_d |
|----------------------------------|-----------------------------|---------------------------------------|------------------------------|-------|-------|
| Patterned Si/SiO _x | 4.0 (0.7) | 56 (7) | 128 (15) | 1.07 | 0.25 |
| Patterned Au | 7.8 (0.8) | 42 (6) | 104 (14) | 1.10 | 0.14 |
| Au-Si -1 | 13 (2) | 55 (9) 27 (3) ^e | 120 (16) | 1.23 | 0.06 |
| Au-Si -2 | 6.5 (0.8) | 57 (6) 30 (3) ^e | 112 (12) | 1.12 | 0.07 |

a: Average AFM-measured heights of patterned features.

b: Average AFM-measured diameters of patterned features.

c: Average AFM-measured peak-to-peak spacing of patterned features.

d: Calculated by approximating the shape of the topological features to be cylinders with heights and diameters as given in the table, and an areal density of 10^{10} features/cm². A sample calculation is provided in Appendix 3.

e: Average FEGSEM-measured diameter of Au islands.

Table 4.2: Measured and calculated contact angles (CA) of nanopatterned and smooth surfaces. Standard deviations are in brackets.

| Surface | Experimental CA | | | | | | Calculated CA | |
|---------------------------------|-------------------|-------------------------|--------------------|----------------|---------------------|--------------------|---------------|---------------|
| | Patterned Surface | | | Smooth Surface | | | θ^w | θ^{cb} |
| | θ_a (°) | θ_r (°) | $\Delta\theta$ (°) | θ_a (°) | θ_r (°) | $\Delta\theta$ (°) | (°) | (°) |
| Si/SiO _x | n/a | n/a | n/a | 56 (3) | 53 (3) | 3 | n/a | n/a |
| Si/SiO _x (milled) | 23 (2) | 13 (8) | 10 ^b | 24 (3) | 18 ^a (3) | 6 ^b | 12 | 122 |
| Au -C5SH | 83 (1) | 81 (1) | 2 | 83 (2) | 76 (2) | 7 | 82 | 89 |
| Au -C18SH | 108 (2) | 108 (2) | 0 | 102 (2) | 101 (1) | 1 | 103 | 153 |
| Au-Si-1 - C5SH | 48 (3) | 28(6) ^a | 20 ^b | n/a | n/a | n/a | 29-38 | 90 |
| Au-Si-2 - C5SH | 55 (3) | 32 (16) ^a | 23 ^b | n/a | n/a | n/a | 30-35 | 89 |

a: Because drops were highly pinned to the surface, an accurate measurement could not be obtained.

b: A large hysteresis is implied because the receding angle approaches 0°.

Unreliable values were obtained for the receding angle (and hysteresis) for the patterned Si/SiO_x surfaces given the large degree of adhesion observed and subsequent pinning of the 3-phase contact line. This is a common observation for such high surface energy substrates yielding contact angles of approximately 20°. It is evident that ion-milling has a significant lowering effect on the surface energy of silicon substrates ($\theta_a = 56^\circ$) when compared to the flat unmilled silicon counterpart ($\theta = 24^\circ$). In terms of the effect of the surface patterned roughness, the experimental values obtained agree with values calculated for complete (Wenzel) wetting within experimental error. Furthermore, the hysteresis appears to increase with the introduction of nanoscale roughness for increasingly hydrophobic surfaces (Si/SiO_x < Au-C5SH < Au-C18SH), where adhesion is also lessened. Lastly, the chemical and topological heterogeneity introduced by the Au island patterned substrates similarly give contact angles that agree reasonably well with those predicted by complete wetting on a surface with a weighted average contribution of surface energy arising from the two components (Si/SiO_x and Au-C5SH SAM). Such a heterogeneous sample is expected to give rise to a larger hysteresis as well.

The choice between a complete wetting (Wenzel-type) to a composite wetting (Cassie-type) has been the subject of recent interest in contact angle

and wettability experiments, particularly in light of the crucial role it plays in designing superhydrophobic surfaces. Johnson and Dettre have addressed this issue experimentally and theoretically for an idealized sinusoidal roughness¹⁴, and the topic has recently been revisited experimentally by Quéré³⁷ and Lee³⁸. The “true” equilibrium contact angle results from the global minimum free energy configuration of the liquid drop on the surface. Metastable configurations exist which give rise to hysteresis and increase with increasing roughness and heterogeneity. Associated with the metastable states are energy barriers which should be overcome in order for the liquid to sample all available states and find the global minimum¹⁴. The wetting configurations expressed by Wenzel and Cassie each describe free energy minima states: the lower contact angle is thus favoured. The spacing and size of the features providing roughness determine which type of wetting is most favourable, as well as the critical angle, θ_{crit} , at which $\theta_{cb} = \theta_w$ (*cf.* Figure 4-6), and can be calculated using equation 4-7 below.

$$\cos \theta_{crit} = \frac{(f-1)}{(r-f)} \quad \text{Equation 4-7}$$

In practice, the metastable state offered by composite wetting for surfaces with $\theta_{crit} > \theta > 90^\circ$ is often observed, instead of complete wetting which is more favourable. This observation has caused some confusion in understanding what conditions lead to composite wetting and hence

ultrahydrophobic and superhydrophobic effects. Lee et al. showed that by *gently* placing a drop of water on a surface (for which complete wetting is energetically favoured) that the measured result is a contact angle corresponding to the composite wetting situation³⁸. The composite surface (surface and air pockets) can also be directly imaged with optical microscopy. However, when the same size drop is dropped from a height onto the surface, the kinetic energy overcomes the energy barrier required to achieve complete wetting and a lower contact angle is observed. Complete wetting of the solid interface results, and is visualized by the drop of water filling in the gaps that had previously been filled by air. Quéré et al. have demonstrated the same principle by applying pressure to the solid-liquid interface by squeezing the liquid between two identical substrates³⁷, and observing the transition from Cassie-type wetting to complete wetting upon compression, and reversal upon retraction.

In light of this revised model for wetting on rough surfaces, characterized by θ_{crit} , it is reasonable that the experimental results obtained for the nanopatterned surfaces measured here agree with complete wetting predicted by the Wenzel equation. In order to create a surface with $\theta \geq \theta_{crit}$, by introducing only the nanoscale topology accessible here (typically 4 nm height, 50 nm diameter, 100 nm spacing), the contact angle of the surface

prior to nanopatterning would have to be $>160^\circ$. However, the highest contact angle reported *via* chemical composition of a smooth surface is $\sim 120^\circ$. This is observed for the hexagonally close-packed $-\text{CF}_3$ surface of a *n*-perfluoroeicosane film. If one can change the aspect ratio of the nanopattern by increasing the height of the features, calculations indicate that a (minimum) height of ~ 185 nm is required for composite wetting to become favourable for a *n*-C18SH-SAM surface (CA = 102°). This minimum height requirement is reduced to ~ 40 nm if a *n*-perfluoroeicosane film (CA = 120°)³⁹ is patterned.

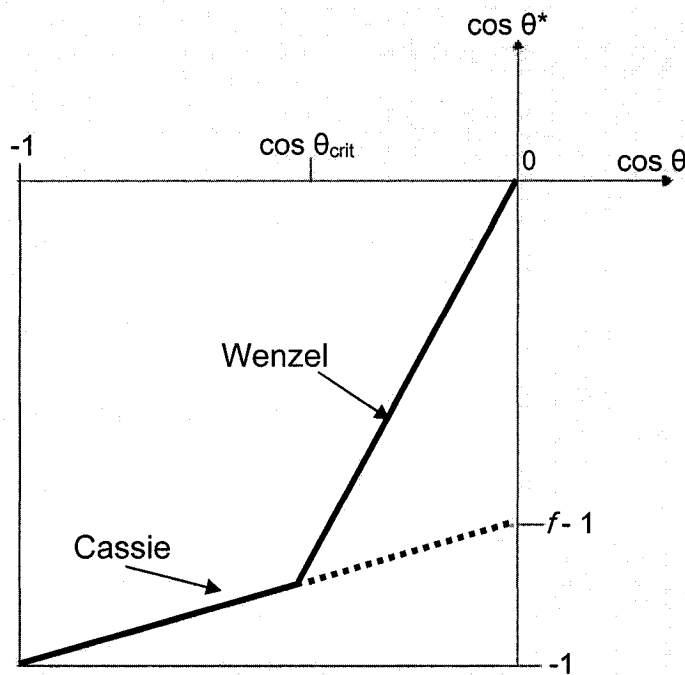


Figure 4-6: Two models of wetting at rough surfaces (θ^* is the apparent contact angle, either θ_w or θ_{cb}). The dotted line depicts the metastable Cassie-type wetting situation (figure adapted from reference 37).

Our findings agree with accounts of the wetting properties of surfaces with similar nanoscale roughness reported in the literature. Both Müller *et al.*²⁸ and Ramos *et al.*³⁰ have created nanostructured surfaces with features of similar aspect ratio (although randomly oriented) and in addition, have varied the areal density of features. Both groups have reported contact angles that correspond to complete wetting of the nanostructured surface with very little dependence on the areal density of features. Both groups also report an increase of hysteresis with areal feature density. However, Ramos *et al.* found that the hysteresis decreases with increasing areal density after a critical density value is reached, although the contact angle remains fairly constant³⁰. They speculate that this finding may point toward a subtle effect as to how the drop is pinned by such a surface in a way that would not significantly affect the static contact angle measurement. Guo *et al.*⁴⁰ as well as Lee *et al.*⁴¹ have created polymer nanopillars using anodized alumina porous templates, yielding feature diameters and feature densities similar to those studied here, but with heights typically >50 nm. Both groups have found that this magnitude of nanostructured roughness is sufficient to yield ultrahydrophobic surfaces that they assign to the Cassie-type wetting mechanism. In another size regime, Zhu *et al.* have demonstrated several

examples of ultrahydrophobic nanostructured surfaces, where the surface features have diameters and/or spacings <100 nm, but have micron scale heights.⁴²⁻⁴⁵

4.4 Conclusions

Contact angle measurements were performed on hydrophobic, hydrophilic, and mixed hydrophobic/hydrophilic nanopatterned substrates. The wetting behaviour was found to be consistent with the theory of wetting on rough substrates proposed by Wenzel⁷. The patterning process used here offers a versatile approach to surface derivatization. Secondary elaboration of the pattern using chemically selective etching/milling processes (such as reactive ion-beam etching) on the Au-Si patterns may offer aspect ratios (increased height) currently unavailable in the current methodology. Current and future efforts include the exploration of the wetting of water on these surfaces with systematic changes in both the topology and derivatization of the Au and/or Si/SiO_x substrate. A better understanding of nanoscale wetting is expected to be of fundamental importance in the design of functional surfaces with or without intentional nanoscale architecture. As such nanoscale wetting is destined to have far-reaching effects on applications such as microfluidics, self-cleaning surfaces, and nanotechnology.

References

1. Good, R. J. In *Contact Angle, Wettability and Adhesion*; Mittal, K. L., Ed.; VSP BV: Utrecht, 1993.
2. Drake, S. *Cause, Experiment and Science: A Galilean Dialogue Incorporating a New Translation of Galileo's Bodies that Stay Atop Water*; University of Chicago Press: Chicago, 1981.
3. Young, T. *Trans. R. Soc. London* **1805**, *95*, 65.
4. Dupré, A. *Théorie Mécanique de la Chaleur*; Gauthier-Villars: Paris, 1869.
5. Chaudhury, M. K.; Whitesides, G. M. *Science* **1992**, *255*, 1230-2.
6. Wenzel, R. N. *J. Ind. Eng. Chem.* **1936**, *28*, 988-94.
7. Wenzel, R. N. *J. Phys. Colloid Chem.* **1949**, *53*, 1466-7.
8. Cassie, A. B. D. *Discuss. Faraday Soc.* **1948**, *No. 3*, 11-16.
9. Cassie, A. B. D.; Baxter, S. *Trans. Faraday Soc.* **1944**, *40*, 546-51.
10. Gao, X.; Jiang, L. *Nature* **2004**, *432*, 36.
11. Arzt, E.; Gorb, S.; Spolenak, R. *PNAS* **2003**, *100*, 10603-6.
12. Blossey, R. *Nat. Mater.* **2003**, *2*, 301-306.
13. Aussillous, P.; Quere, D. *Nature* **2001**, *411*, 924-7.
14. Johnson, R. E., Jr.; Dettre, R. H. *Adv. Chem. Series* **1964**, *43*, 112-35.
15. Joanny, J. F.; De Gennes, P. G. *J. Chem. Phys.* **1984**, *81*, 552-62.
16. Johnson, R. E., Jr.; Dettre, R. H.; Brandreth, D. A. *J. Colloid Interface Sci.* **1977**, *62*, 205-12.
17. Barthlott, W.; Neinhuis, C. *Planta* **1997**, *202*, 1-8.
18. Bico, J.; Marzolin, C.; Quere, D. *Europhys. Lett.* **1999**, *47*, 220-226.
19. Feng, L.; Li, S.; Li, Y.; Li, H.; Zhang, L.; Zhai, J.; Song, Y.; Liu, B.; Jiang, L.; Zhu, D. *Adv. Mater.* **2002**, *14*, 1857-1860.
20. Öner, D.; McCarthy, T. J. *Langmuir* **2000**, *16*, 7777-7782.
21. Xie, Q.; Xu, J.; Feng, L.; Jiang, L.; Tang, W.; Luo, X.; Han, C. C. *Adv. Mater.* **2004**, *16*, 302-305.

22. Sun, T.; Wang, G.; Feng, L.; Liu, B.; Ma, Y.; Jiang, L.; Zhu, D. *Angew. Chem. Int. Ed.* **2004**, *116*, 361-364.
23. Liu, H.; Feng, L.; Zhai, J.; Jiang, L.; Zhu, D. *Langmuir* **2004**, *20*.
24. Shirtcliffe, N. J.; McHale, G.; Newton, M. I.; Chabrol, G.; Perry, C. C. *Adv. Mater.* **2004**, *16*, 1929-1932.
25. Woodward, I.; Schofield, W. C. E.; Roucoules, V.; Badyal, J. P. S. *Langmuir* **2003**, *19*, 3432-3438.
26. Lau, K. K. S.; Bico, J.; Teo, K. B. K.; Chhowalla, M.; Amaratunga, G. A. J.; Milne, W. I.; McKinley, G. H.; Gleason, K. K. *Nano Lett.* **2003**, *3*, 1701-1705.
27. Krupenkin, T. N.; Taylor, J. A.; Schneider, T. M.; Yang, S. *Langmuir* **2004**, *20*, 3824-3827.
28. Muller, B.; Riedel, M.; Michel, R.; De Paul, S. M.; Hofer, R.; Heger, D.; Grutzmacher, D. *J. Vac. Sci. Technol. B* **2001**, *19*, 1715-1720.
29. Grundke, K.; Pospiech, D.; Kollig, W.; Simon, F.; Janke, A. *Colloid Polym. Sci.* **2001**, *279*, 727-735.
30. Ramos, S. M. M.; Charlaix, E.; Benyagoub, A.; Toulemonde, M. *Phys. Rev. E* **2003**, *67*, 031604/1-031604/6.
31. Ramos, S. M. M.; Charlaix, E.; Benyagoub, A. *Surf. Science* **2003**, *540*, 355-362.
32. Substrates were cleaned using a "degreasing" treatment consisting of soaking in recently boiled 50:50 ethanol/chloroform solution for 5 mins followed by 2 mins of sonication.
33. prepared as per *Meli et al.*, *Nano Lett.* **2002**, *2(2)*, 131-135.
34. Substrates were placed 1 cm away from a Hg pen lamp (4.5 mW/cm²) in ambient air. Previous experiments and literature reports (see reference 26 for example) have demonstrated the effectiveness of this method in alkanethiol oxidation and subsequent removal from gold surfaces.

35. Tarlov, M. J.; Burgess, D. R. F., Jr.; Gillen, G. *J. Am. Chem. Soc.* **1993**, *115*, 5305-6.
36. Nitrogen gas was circulated 5 times through a saturated solution of potassium carbonate and sent to the humidity chamber (80 ml) for vapour exchange at a flow rate of ~50 ml/min for at least 2 hours. The humidity chamber was placed on top of a temperature controlled stage set at 25°C.
37. Lafuma, A.; Quere, D. *Nat. Mater.* **2003**, *2*, 457-460.
38. He, B.; Patankar, N. A.; Lee, J. *Langmuir* **2003**, *19*, 4999-5003.
39. Nishino, T.; Meguro, M.; Nakamae, K.; Matsushita, M.; Ueda, Y. *Langmuir* **1999**, *15*, 4321-4323.
40. Guo, C.; Feng, L.; Zhai, J.; Wang, G.; Song, Y.; Jiang, L.; Zhu, D. *ChemPhysChem* **2004**, *5*, 750-753.
41. Lee, W.; Jin, M.-K.; Yoo, W.-C.; Lee, J.-K. *Langmuir* **2004**, *20*, 7665-7669.
42. Feng, X.; Feng, L.; Jin, M.; Jiang, L.; Zhu, D. *J. Am. Chem. Soc.* **2004**, *126*, 62-63.
43. Feng, L.; Li, S.; Li, H.; Zhai, J.; Song, Y.; Jiang, L.; Zhu, D. *Angew. Chem. Int. Ed.* **2002**, *41*, 1221-1223.
44. Feng, L.; Yang, Z.; Zhai, J.; Song, Y.; Liu, B.; Ma, Y.; Yang, Z.; Jiang, L.; Zhu, D. *Angew. Chem. Int. Ed.* **2003**, *42*, 4217-4220.
45. Feng, L.; Song, Y.; Zhai, J.; Liu, B.; Xu, J.; Jiang, L.; Zhu, D. *Angew. Chem. Int. Ed.* **2003**, *42*, 800-802.

Connecting Text for Chapter 5:

Spectroscopic Characterization of Au Island Patterns

This Chapter describes the spectroscopic characterization (absorbance) of the nanoparticle arrays created using the methods described in Chapter 3 and quartz substrates. The surface plasmon resonance response of the nanoparticle array is measured as an absorption band in UV-vis spectroscopy, and compared with the response predicted by the quasistatic approximation to Mie theory. The nanoparticles in the array are believed to be isolated such that each gives rise to an independent, uncoupled, surface plasmon resonance upon the absorption of incident light. The response of the surface plasmon resonance of the nanoparticle arrays to different media, as well as the effect of derivatization with a self-assembled monolayer was also explored.

An interesting result of this study is the measured peak shift in different media combined with the FEGSEM-measured radius of the nanoparticles can be used with the quasistatic approximation model to deduce the average height of the nanoparticles in the array, circumventing the problem of direct height measurement involving sample destruction.

This Chapter describes an important application of the methodology described in Chapter 3. The feasibility of the method to create monolayer

arrays of gold nanoparticles with spacings and sizes determined by the block copolymer mask, and which have absorbance properties that can be measured using a conventional UV-vis spectrometer.

Chapter 5

Spectroscopic Characterization of Au Island Patterns formed on Solid Surfaces

5.1 Characterization of Au Island Pattern in Air

5.1.1 Introduction

The field of nanoparticle research has attracted much interest as a result of the search and discovery of new properties when materials are reduced in size and dimensionality. Quantum size effects and greatly enhanced surface-to-volume ratios have brought nanoparticles to the forefront of emerging nanotechnologies. Semiconducting nanoparticles have markedly different spectroscopic properties from both their bulk counterparts as well as molecular dyes, such as fluorescence with exceptional quantum yields, stability toward photobleaching, and emission wavelengths that can be directly tuned by changing the diameter of the nanoparticle. Many researchers have since been interested in the physical and chemical properties of semiconducting nanoparticles, especially those who wish to use them in a range of applications from solar cells to optical data storage to bio-labelling.

Similarly, gold has become a newly relevant material for catalysis¹⁻⁵,

drug delivery and therapeutics,⁶⁻¹¹ and nanocomposites^{5,7,12-17} when in nanoparticulate form. The strong ruby red colour of nanoscale gold is the result of its strong interaction (absorption and scattering) with light which is typically several orders of magnitude more efficient than that of organic dyes. This unique property of metallic nanoparticles has generated much interest in their applications in surface-enhanced Raman spectroscopy¹⁸⁻²⁰, nanophotonics²¹⁻²³, and a variety of sensing approaches²⁴⁻²⁹.

Introducing spatial and orientational order to metal nanoparticles creates many advantages to the applications listed above, by virtue of creating more uniform materials and thus more predictable behaviour. In particular, size, shape, orientation and spacing can all have very significant consequences on the optical properties of metal nanoparticles in terms of both the extinction wavelength and extinction efficiency, as well as sensitivity towards adsorbates or surrounding medium^{1,30-32}.

In this study, arrays of isolated gold nanoparticles, as gold islands, have been prepared on quartz substrates using the methodology described in Chapter 3. Transmission mode UV-Visible spectroscopy measurement of the arrays performed to obtain the extinction of the gold islands. These data are compared to the calculated extinction of oblate gold spheroids via the quasistatic approximation to Mie theory³³.

5.1.2 Experimental Section

Quartz slides (Chemglass, Inc.) were soaked in hot 50:50 $\text{CHCl}_3/\text{EtOH}$ solution for 10 mins, followed by bath sonication (Branson 1510) for 2 mins, before drying under a gentle stream of N_2 gas. A very thin layer of Ti (0.5 nm) followed by 20 nm Au were sputter deposited (20 W, 6 mTorr Ar) onto the quartz slides. A block copolymer (polystyrene-*b*-poly-2-vinylpyridine) film was transferred to the Au-coated quartz slides using the Langmuir-Blodgett deposition technique (23 °C, KSV 3000) at 2 mN/m, with an upstroke speed of 1 mm/min. Ion-milling of the substrates (6 keV, 3.5 $\mu\text{A}/\text{cm}^2$, samples rocked at 40°/s from 0 to 50° from the surface normal, 60 rpm, MET-ETCH, Gatan, Inc.) was tracked using FEGSEM to determine when the gold layer became sufficiently discontinuous and the pattern of Au “islands” became observable. The ion-milling process typically required between 270s and 300s. Atomic force microscopy was used to measure the nanoparticle height (AutoProbe CP, Park Scientific Instruments). UV-vis spectra (extinction) were obtained for the substrates in the standard transmission mode set-up (90° incidence, Cary 5000, Varian), both before and after annealing the samples at 400 °C for 2 hours³⁴. Figure 5-1 shows a representative image and corresponding UV-vis spectrum for the gold island sample referred to throughout as “Au-Quartz 1”.

5.1.3 Results and Discussion

The average diameter of the gold islands was determined using FEGSEM (Hitachi S-4700, 1-2 kV, 10 μ A) images in SigmaScan Pro 5.0 image software. The average height of the gold islands (Figure 5-1) was determined by taking the difference of AFM-determined average height of the patterned features before and after the gold was removed by dissolution in aqua regia (1:3:6 HNO₃(conc.):HCl (conc.): H₂O; 20 mins). Both the roughness of the Au layer and the underlying quartz substrate, as well as the ion-milling process contributes to increase the average roughness of these substrates. An increased uncertainty in these measurements results, compared to measurements made of the patterned features on either silicon or template-stripped gold. Figure 5-2 shows the AFM images used to measure the average height values. Although it is more difficult to visualize in the AFM images, the topological pattern resulting from the block copolymer mask is still present. This is evident in the 2D self-correlation plots included in Figure 5-2. Table 5-1 lists the dimensions of the gold island samples determined in the AFM and FEGSEM analyses.

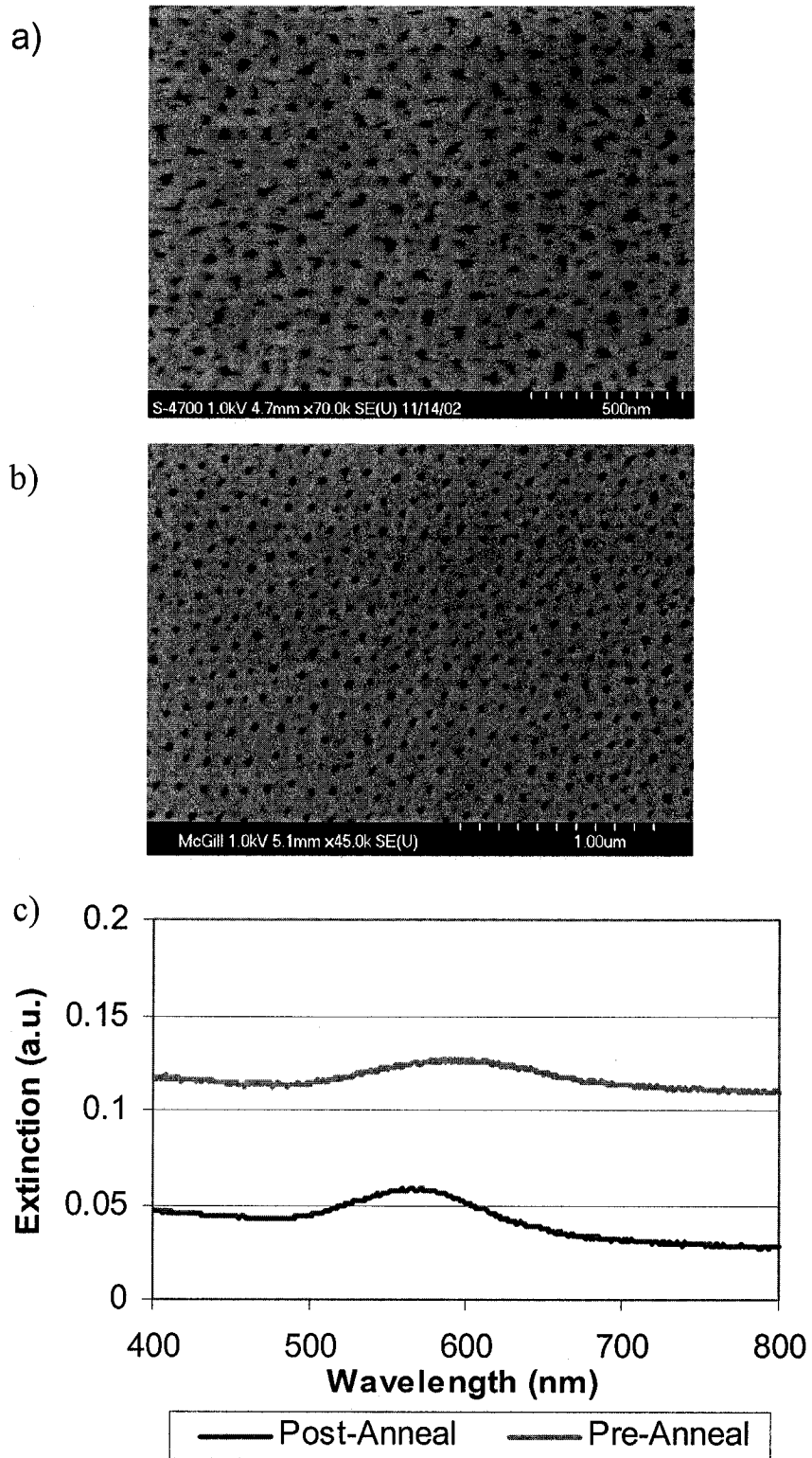


Figure 5-1: FEGSEM image of Au-Quartz 1 before (a) and after (b) annealing, with corresponding UV-vis spectra (c).

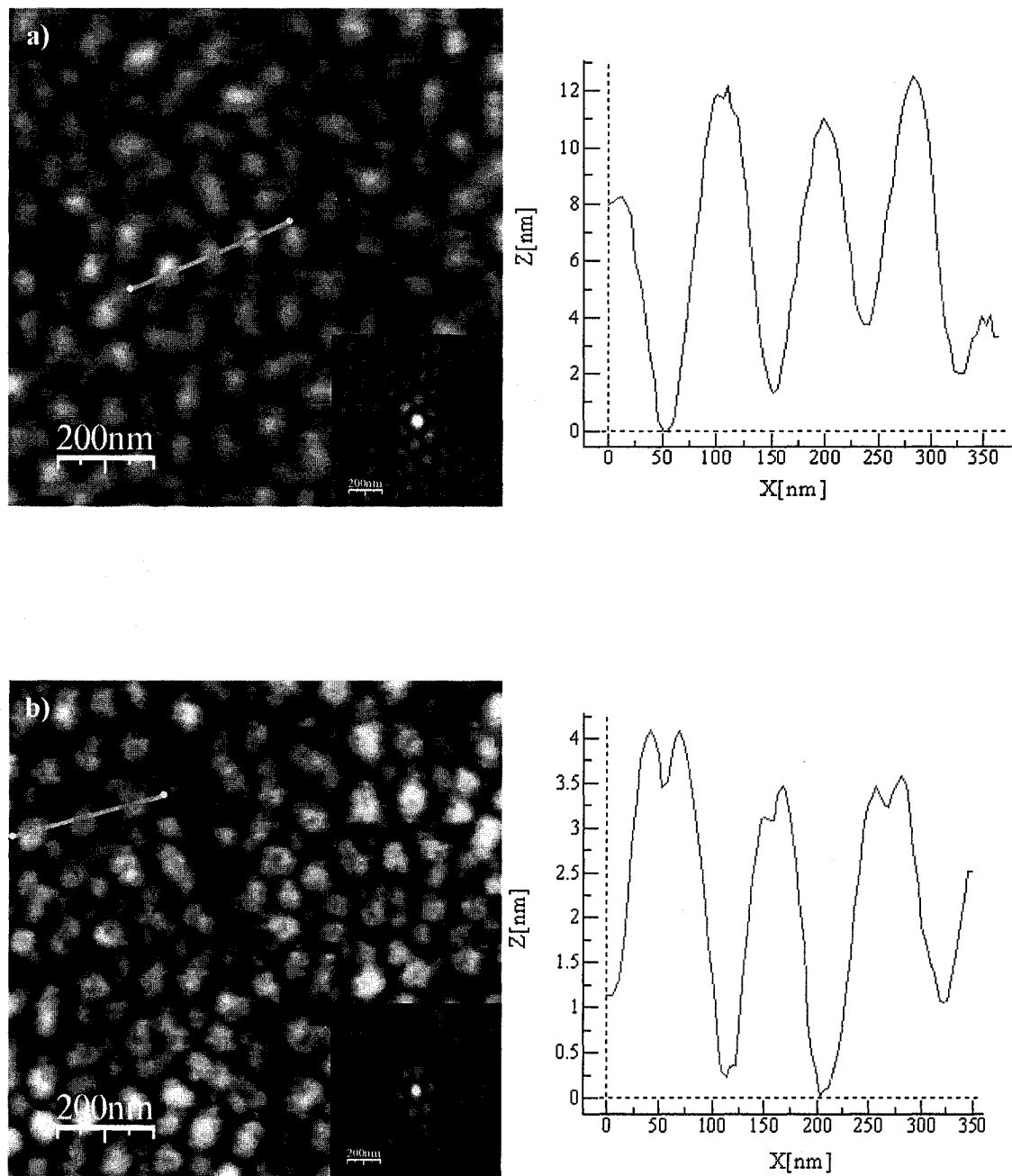


Figure 5-2: 1 μm x 1 μm AFM images of Au-Quartz 1 obtained with tapping mode imaging using a Si cantilever ($f_0 \sim 300$ kHz, Asylum Research) with the corresponding cross-section profile (right) and 2D self-correlation plot (inset); The sample was imaged before (a) and after (b) the gold was removed.

Table 5-1: Characteristics of Au-Quartz 1 sample. Standard deviations are in brackets.

| Sample | Radius ^a (nm) | Height (nm) | | | |
|-------------|-----------------------------|----------------------------|---|---|---|
| | | Au- Quartz ^b | Quartz ^c (Au- removed) | Height of Au Islands ^d | Depth Embedded in Quartz ^e |
| Au Quartz 1 | 22 (3) | 14.6 (3.4) | 3.1 (0.89) | 11.5 (3.5) | 0.9 (0.4) |

a. the FEGSEM-measured radius

b. the AFM-measured height of patterned features before the gold was removed

c. the AFM-measured height of the remaining quartz features after the gold was removed

d. the estimated height of the Au islands as per text

e. the AFM-measured height of the depressions left in quartz features after the gold was removed

5.1.3.1 Modeling the Surface Plasmon Resonance Response of Au Islands

The distinct colours produced by gold nanoparticles have been of interest for centuries. However, the ruby red pigment in stained glass in the 17th century was only recognized to arise from colloidal metallic gold by Faraday in 1857³⁵. Almost 50 years later, Gustav Mie presented a solution to Maxwell's equations which describes the extinction of light by spherical particles of arbitrary size³⁶. Mie's solution has remained relevant to a number

of scientific applications, and in particular has been applied to the field of metal nanoparticles. It is found to be sufficiently accurate in predicting optical properties of spherical particles if the material dielectric function is known. A number of approximations to Mie's solution are commonly employed to simplify the calculation, especially for more complex shapes such as the spheroids used in this work.

The absorption of light when absorbed by a metal particle results in the coherent oscillation of the conduction band electrons with the oscillating electric field component of the incident radiation. The resulting resonances, known as surface plasmons, occur for Au, Ag, and Cu in the UV-vis portion (300-900 nm) of the electromagnetic spectrum. Surface plasmon resonance is highly dependant on the size, shape, and chemical composition of the particles that give rise to this nanoscale phenomenon³⁷.

For the case of spherical particles that are sufficiently smaller than the wavelength of the absorbing light (about 25 nm for gold particles³⁸), the electric field of the light is considered to be constant. This allows for an electrostatic approximation of the interaction. This approximation, called the *quasistatic* approximation because it uses the frequency-dependent dielectric functions for the metals (the medium dielectric constant is considered to be constant in the UV-visible), only the dipolar resonance response of the

nanoparticle free electrons is considered, as higher-order multipolar resonances become negligible³⁷. Once the nanoparticle is sufficiently large, this is no longer the case. Quadrupolar resonance (and higher order poles) becomes increasingly more important than the dipolar contribution.

Although the exact solution to Maxwell's equations for spheroids is also known^{39,40}, the solution is so cumbersome that it is infrequently used. In addition, Voshchinnikov and Farafonov (VF)⁴¹ have shown, using a numerical implementation based on this theory, that the quadrupolar resonance mode becomes much less important as the aspect ratio of the spheroid is increased. The quasistatic approximation is thus often used for spheroidal particles when the major axis is much larger than what is allowed in the spherical case (~12 nm for gold).

A spheroid is a 3D surface generated by rotating an ellipse around one of its principal axes, resulting in a shape where two of the principle axes (a , b , c) are equal (Figure 5-3). This is a special case of the general ellipsoid, where $a \neq b \neq c$. This loss in symmetry leads to two distinct polarizations in the spheroidal case, and three polarizations in the ellipsoidal case, each of which give rise to a distinct plasmon resonance (manifested as an absorbance maximum). A resonance occurring along the major axis of the spheroid is called a longitudinal plasmon, whereas that occurring along the

minor axis is called the transversal plasmon. When $a > b = c$ (prolate spheroid), there are two transversal plasmon modes and one longitudinal plasmon mode. On the other hand when $a = b > c$ (oblate spheroid), there are two longitudinal plasmon modes and one transversal mode.

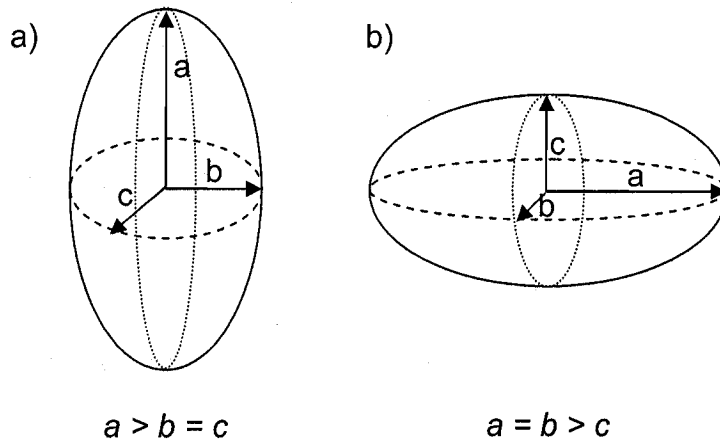


Figure 5-3: Prolate (a) and oblate (b) spheroids.

Using the quasistatic approximation, the extinction coefficient κ for N particles of volume V is determined using Equation 5-1.³⁸

$$\kappa = \frac{2\pi N V \epsilon_m^{3/2}}{3\lambda} \sum_j \frac{(1/P_j^2) \epsilon_2}{\left(\epsilon_1 + \frac{1-P_j}{P_j} \epsilon_m \right)^2 + \epsilon_2^2} \quad \text{Equation 5-1}$$

where ϵ_1 and ϵ_2 are the real and imaginary components to the dielectric function of the metal, ϵ_m is the real component of the dielectric constant of the medium, λ is the wavelength of light. P_j ($j = 1, 2, 3$) values are the depolarization factors for the three axes, bound by the sum rule³³:

$$\sum P_j = 1 \quad \text{Equation 5-2}$$

(prolate spheroid)

$$P_1 = \frac{1-e^2}{e^2} \left[\frac{1}{2e} \ln \left(\frac{1+e}{1-e} \right) - 1 \right] \quad \text{Equation 5-3}$$

$$P_2 = P_3 = \frac{1-P_1}{2} \quad \text{Equation 5-4}$$

$$e = \sqrt{1 - \frac{b^2}{a^2}} \quad \text{Equation 5-5}$$

(oblate spheroid)

$$P_1 = \frac{g(e)}{2e^2} \left[\frac{\pi}{2} - \tan^{-1} g(e) \right] - \frac{g^2(e)}{2} \quad \text{Equation 5-6}$$

$$P_3 = 1 - 2P_1 \quad \text{Equation 5-7}$$

$$g(e) = \sqrt{\frac{1-e^2}{e^2}} \quad \text{Equation 5-8}$$

$$e = \sqrt{1 - \frac{c^2}{a^2}} \quad \text{Equation 5-9}$$

Although a number of theoretical methods of averaging mixed component dielectric constants to obtain an *effective* medium dielectric constant exist⁴²⁻⁴⁶, a simple average has often served as a reasonable qualitative approximation in the literature^{31,37,47}. For a medium consisting of quartz ($n = 1.55$) on one side and air ($n = 1.00$) on the other side, the effective medium, ϵ_m , was approximated here by calculating a weighted average:

$$\epsilon_m = P_{\text{quartz}} \epsilon_{\text{quartz}} + (1 - P_{\text{quartz}}) \epsilon_{\text{air}} \quad \text{Equation 5-10}$$

$$n_m = \sqrt{\varepsilon_m} \quad \text{Equation 5-11}$$

where p_{quartz} is the ratio of the nanoparticle surface area in contact with the quartz substrate. This approximation is similar to that provided by Maxwell Garnett theory^{33,42}, except that it does not include a weighting factor associated with the spheroidal shape probability distribution function^a.

The extinction coefficient per nanoparticle for the gold islands patterned on quartz described above was modelled using Equation 5-6, using $p_{\text{quartz}} = 0.13$ (see Appendix 4 for the calculation of p_{quartz}). The input radius for the minor axis was estimated to be half of the total height of the gold islands ($11.5 / 2 = 5.75$ nm). Experimental values determined by Johnson and Christy⁴⁸ for the dielectric function of gold in the range of 400 nm - 900 nm were used in the calculation. The results are plotted in Figure 5-4, and the peak position is tabulated with the experimentally obtained peak position in Table 5-2.

^a The spheroidal shape probability distribution function arises in Maxwell Garnett theory due to the assumption of randomly oriented and shaped spheroids embedded in a homogeneous matrix³³, which we considered to be beyond the scope of this analysis. The excellent correspondence between the experimental and calculated resonance peak positions (Table 5-2) suggests that such a factor is not of key importance in the samples studied here. The approximation used here is based on the assumption that the nanoparticles present in these experiments have uniform orientation and shape within a given sample. Furthermore the geometrically-weighted (i.e. %contact area) average used here improves upon the commonly used approximation obtained from performing an (number) average dielectric constant (i.e. arising from 50% contact)³⁷ and is meant to provide us with a qualitative description of the effect of particle embedding in the substrate.

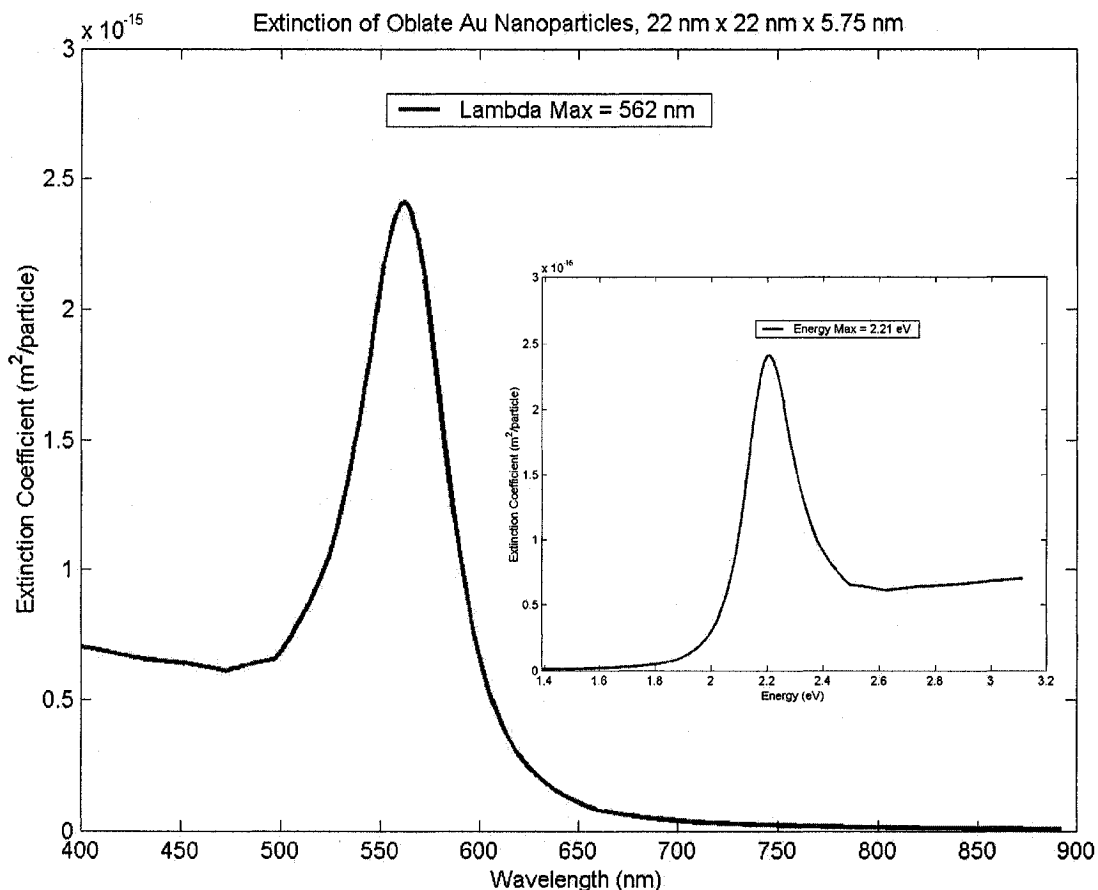


Figure 5-4: Calculated optical extinction coefficient of Au-Quartz 1(22 nm x 22 nm x 5.75 nm) as a function of wavelength and energy (inset). The effective medium (n=1.087) has a 13% contribution from quartz.

Table 5-2: Calculated and experimental extinction coefficients (κ) and peak widths (full width at half maximum, FWHM) of Au-Quartz 1.

| Calculated | | | | Experimental | | | |
|-------------------------|-------------------------------|---|--------------|-------------------------|-------------------------------|---|--------------|
| λ_{max} (nm) | κ (m ²) | κ (M ⁻¹ cm ⁻¹) | FWHM (nm) | λ_{max} (nm) | κ (m ²) | κ (M ⁻¹ cm ⁻¹) | FWHM (nm) |
| 562 | 2.4×10^{-15} | 1.5×10^{10} | 60 | 561 | 3.2×10^{-16} | 1.9×10^9 | 115 |

The total extinction of light by the gold island samples can then be calculated as:

$$\text{Extinction} = \kappa\alpha \quad \text{Equation 5-12}$$

where α is the areal density of the array (m^{-2}). The areal density for the pattern obtained from the PS-P2VP surface micellar film is 9.5×10^{13} features/ m^2 . An equivalent number density of gold islands is generated. Experimentally-determined extinction coefficients were calculated by determining the extinction from the measured peak heights in the annealed gold island samples (Table 5-2).

The transmission UV-vis measurements obtained for the gold island samples show the excitation of only one plasmon resonance mode given the observation of a single peak (Figure 5-1). This corresponds to the longitudinal resonance mode of the nanoparticles. The absence of the transversal mode excitation is due to the 90° angle of incidence used in the transmission measurement. This orientation restricts the polarization to only be along the major axis of the particles, given their orientation on the quartz substrate. In any case, the transverse mode does not appear in the calculated spectra in the range of 400-800 nm for nanoparticles of the dimensions prepared here (Figure 5-4).

The experimental results for λ_{\max} and κ agree well with the results predicted by the model. The discrepancy in peak widths and the magnitude of the extinction coefficient are attributable to the distribution in the size of the gold islands (both radius and height) as well as the uncertainty in the extent to which the gold islands are embedded in the quartz substrate. Figure 5-5 shows how sensitive both the resonance frequency (peak position) and extinction coefficient (peak height) are to small changes in the gold island height and effective medium. Extinction coefficients on the order of 10^9 - 10^{10} ($M^{-1}cm^{-1}$) are typically observed for oblate nanoparticles with similar aspect ratios to those measured here ($a/c \approx 3$)^{26,31,38}. The agreement in peak positions between the experimental results and the model indicates the absence of near-field coupling interactions. Near field interactions arise when the particle spacing is less than the particle diameter^{30,49}. This is not the case here (Figure 5-1b). On the other hand, the particles are spaced far enough to undergo far-field dipolar interactions. However such interactions require a nearly perfectly ordered array^{31,50}. This condition is not met in our sample, and as such far field effects are not expected to have an appreciable effect on the absorption of these arrays.

Upon annealing the gold island pattern, the measured transmission UV-vis extinction peak is considerably blue-shifted (approximately 30 nm),

and the peak width is significantly reduced. Both changes indicate a reduction of the aspect ratio, and that the particle size and shape have become more uniform. There may also be a loss of interparticle coupling mediated by the small nanoparticle “remnants” present in larger proportion before annealing had taken place. Such coupling can lead to a red-shifting of the peak position compared to isolated particles.^{30,49}

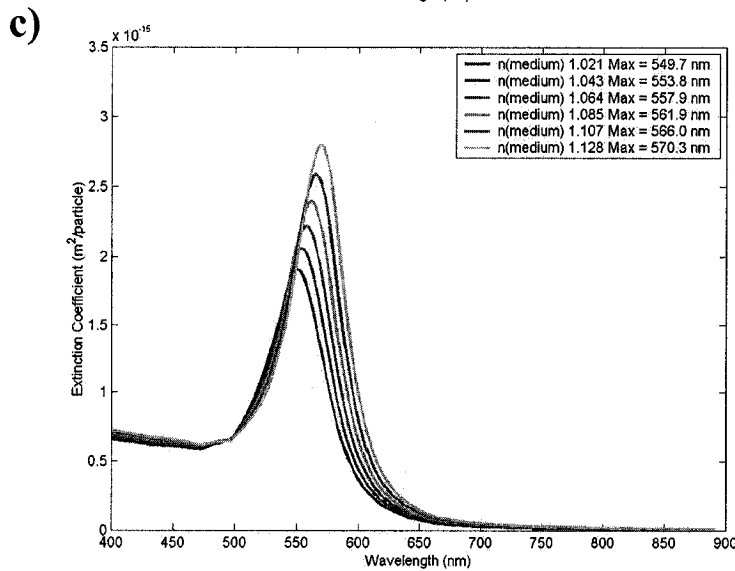
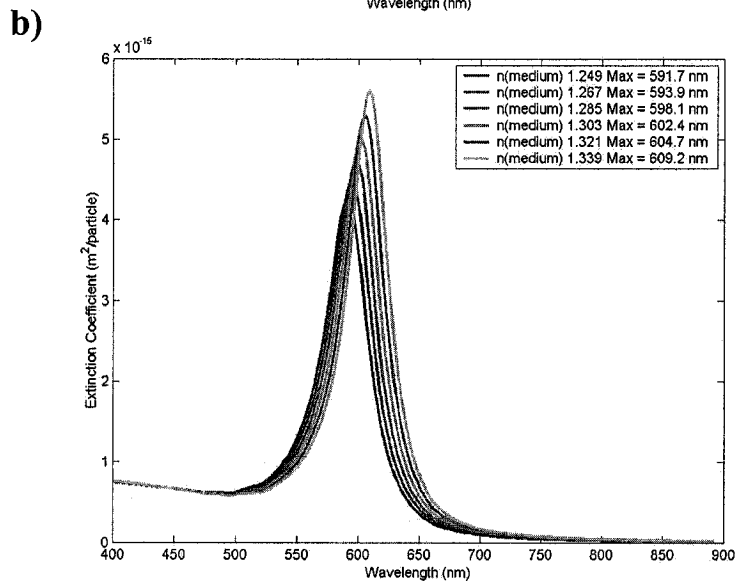
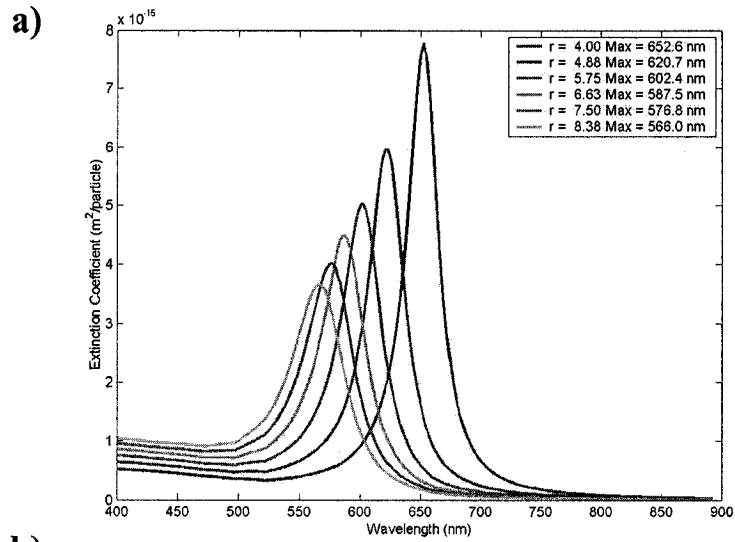


Figure 5-5: a) Effect of (small) changes in gold island height on peak height and position. b-c) Effect of (small) changes in refractive index of the effective medium when n_{quartz} ranges from 0.4 to 0.6 (b), and 0.03 to 0.23 (c). Note the different scale (on the y-axes) in (a) *cf.* (b) and (c).

5.2 Towards the design of a bio-/chemo-sensor:

The effect of the surrounding medium

5.2.1 Introduction

Surface plasmon resonance is very sensitive to changes in the dielectric medium. This property is used in surface plasmon resonance spectroscopy, and a number of nanoparticle sensing schemes^{27,51-56}. Dependence on the medium dielectric is especially large for the longitudinal mode of spheroidal particles and is enhanced with increasing aspect ratio³¹. This dependence on nanoparticle shape has been extensively explored by Van Duyne and coworkers using truncated tetrahedral nanoparticle arrays formed by the deposition of silver through a monolayer of polystyrene spheres deposited on glass surface (*nanosphere lithography*⁵⁷). The individual particles are highly uniform in dimensions. Particles made using nanosphere lithography typically are approximately 100 nm wide and 50 nm high⁵⁷. Optimization of the shapes and sizes, as well as the interparticle distance

dependence of the surface plasmon response is critical to the design of nanoparticle-derivatized surfaces for sensing applications. The criteria have been addressed by several groups using extended Mie theory^{31,58} as well as other electrodynamic models such as the discrete dipole approximation.⁵⁹⁻⁶¹

In this report, the extinction maximum of the gold island arrays formed on quartz described earlier was measured in several different media in order to demonstrate the capability of these surfaces to serve as optical sensors.

5.2.2 Experimental Section

Gold island samples were prepared on quartz slides using the methodology previously described (section 5.1.2). FEGSEM images of the substrate were used to determine the average radius (i.e., the longitudinal axis). AFM measurements of the substrate were made in order to measure the total height (nanoparticle height + quartz post height). The substrate was cleaned in a UV-ozone chamber (BioForce Inc. USA) for 1 hour, rinsed well with ethanol and water (MilliPore, 18M Ω), dried under a stream of nitrogen, and placed in a custom-made flow-through liquid cell. Ethanol ($n = 1.3614$), methanol ($n = 1.3288$), acetone ($n = 1.3588$), cyclohexane ($n = 1.4262$), and toluene ($n = 1.4961$) were used as received (Fischer Scientific, ACS grade in each case). The solvents were introduced to the cell in varying order in order to ensure that solvent exchange at the gold surface was complete in each

case. Measurements under nitrogen were performed first by purging with N₂ (g) for at least 5 mins. All measurements were performed in triplicate.

5.2.3 Results and Discussion

Since a direct measurement of the nanoparticle height and degree of contact with the quartz substrate cannot be made without removing the gold (in other words, destroying the sample), the model described above was used to determine both parameters. The peak position of the gold island arrays measured in a nitrogen atmosphere and the FEGSEM-determined diameter of the major axis were used to infer the value of the minor axis (i.e. nanoparticle height/2), assuming p_{quartz} is approximately 0.5. Figure 5-6 shows FEGSEM images of the gold island samples used in this experiment. The corresponding UV-vis spectra (obtained under nitrogen) are found in Figure 5-7. Figure 5-8 shows the calculated spectra used to estimate the minor axis length, and the estimated dimensions of the gold islands are listed in Table 5-3.

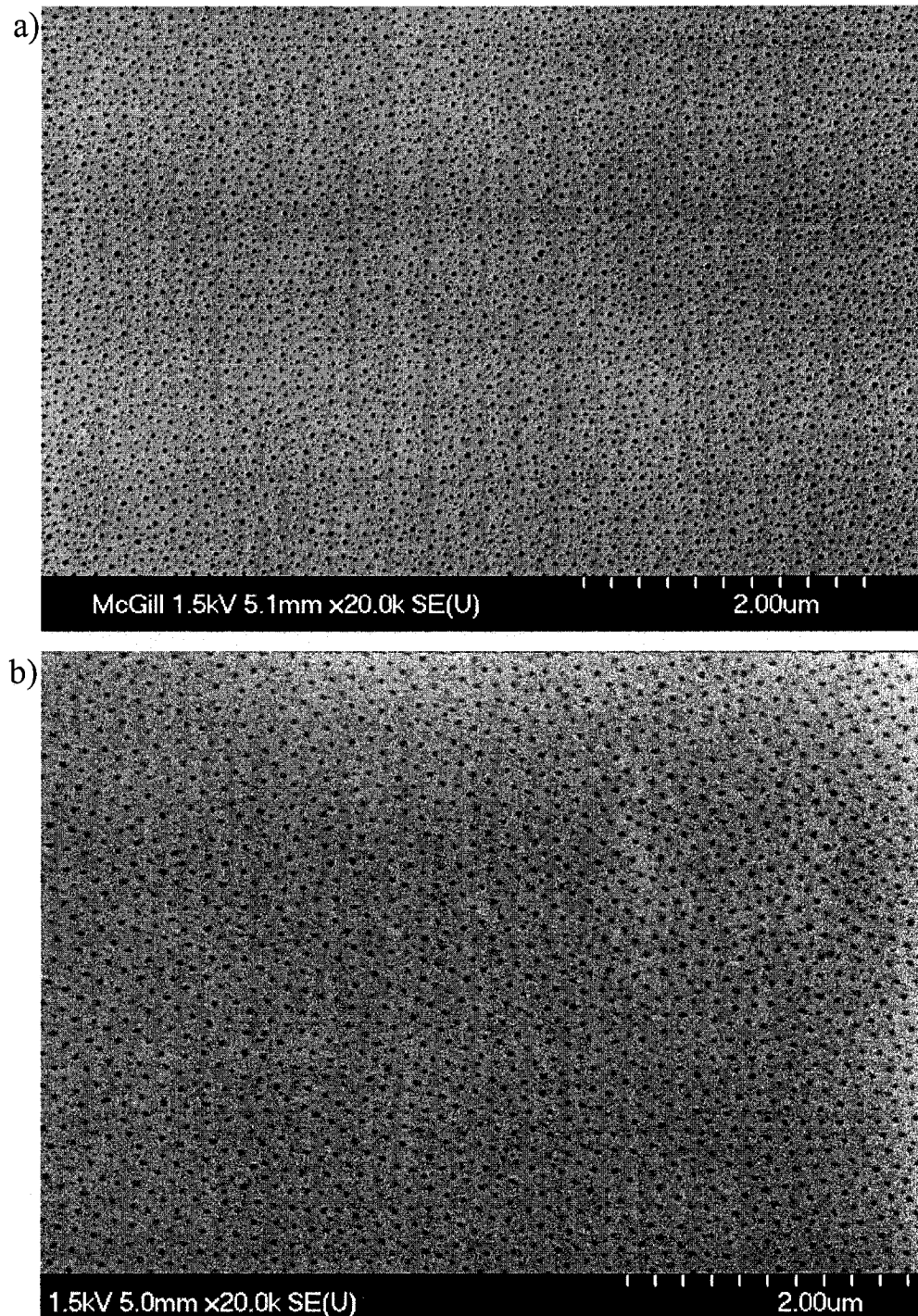


Figure 5-6: FEGSEM (Hitachi S-4700) image of Au-Quartz 2 (a) and Au-Quartz 3(b). Secondary electron images were obtained at 1.5kV, 10 μ A, 5mm working distance, using the upper detector.

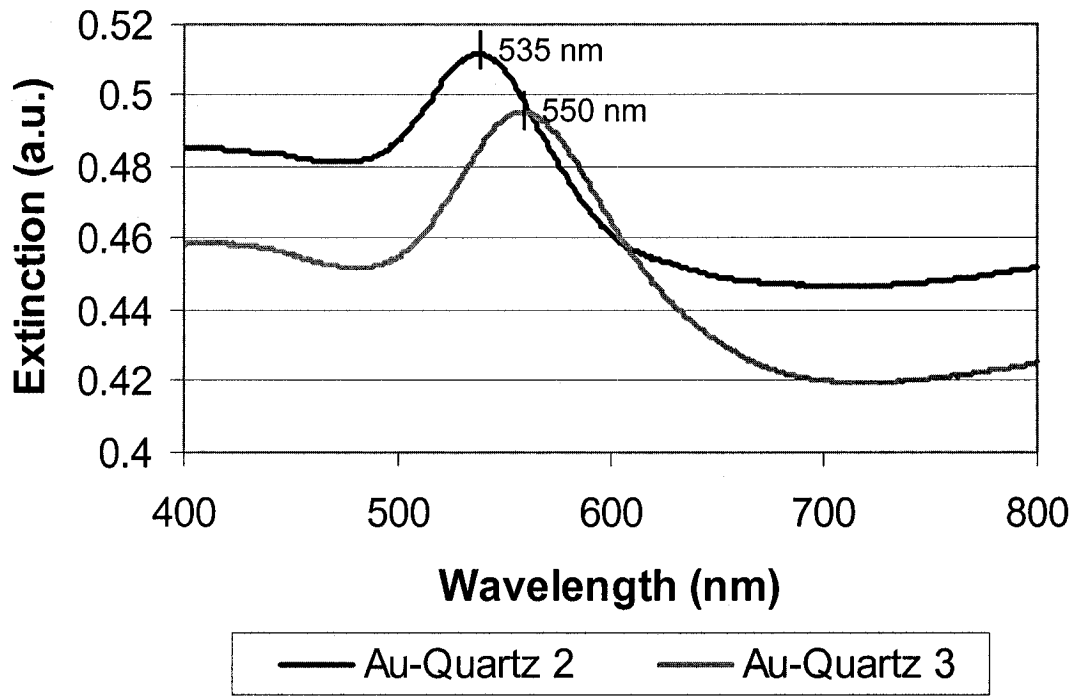


Figure 5-7: Extinction spectra of Au-Quartz 2 and Au-Quartz 3 obtained under a nitrogen atmosphere.

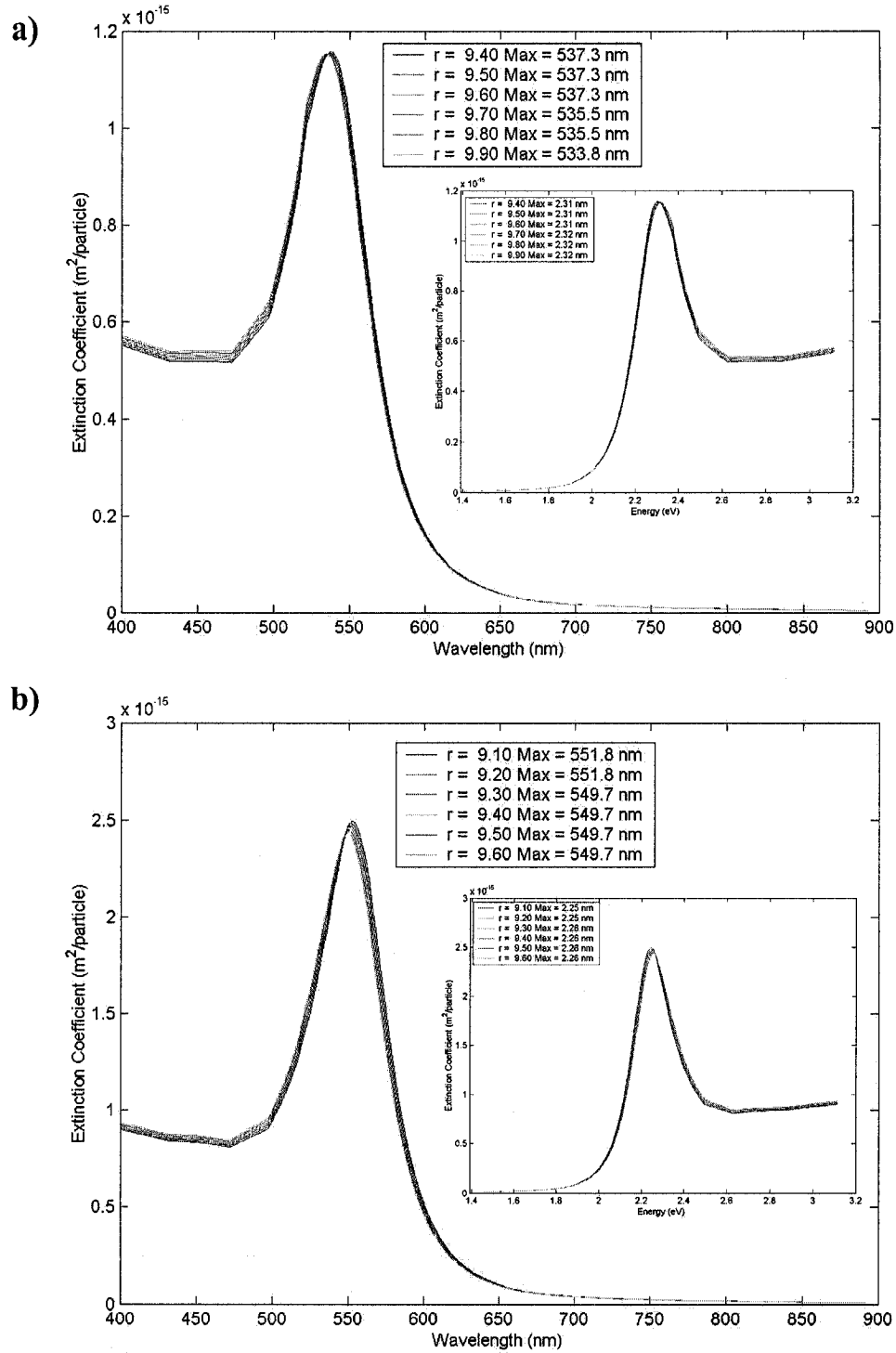


Figure 5-8: Calculated spectrum of (a) Au-Quartz 2 and (b) Au-Quartz 3 as a function of minor axis length, in an effective medium n_m of 1.304 ($p_{\text{quartz}} = 0.5$). Energy plots are included as insets.

Table 5-3: Measured and calculated dimensions of gold islands in Au-Quartz

2.

| Sample | Radius ^a (nm) | Total Height ^b (nm) | Height ^c (nm) | p_{quartz}^d | n_m^e | Aspect Ratio ^f (a/c) |
|-------------|-----------------------------|-----------------------------------|-----------------------------|-----------------------|---------|---|
| Au-Quartz 2 | 16 (3)* | 21 (2) | 19.7 | 0.500 | 1.304 | 1.7 |
| | | | 18.8 | 0.450 | 1.277 | 1.7 |
| Au-Quartz 3 | 20 (3) | 21 (2) | 18.5 | 0.500 | 1.304 | 2.2 |
| | | | 20.6 | 0.600 | 1.357 | 1.9 |

a: FEGSEM-measured radius. Standard deviations are in brackets.

b: AFM-measured average height of Au islands on quartz posts. Standard deviations are in brackets.

c: Estimated Au island height.

c-f: Top row corresponds to the estimate assuming $p_{\text{quartz}} = 0.5$. Bottom row corresponds to estimate made after iterative adjustments to the gold island height and p_{quartz} were made.

The UV-vis peak maxima shifted as a function of the solvent. The peak positions were determined from the raw data and are plotted in Figure 5-9 along with the peak maxima determined by modelling the gold spheroids in the same media, still assuming $p_{\text{quartz}} = 0.5$.

* A bimodal distribution of nanoparticle sizes is in fact determined for this sample (see Figure 5-6) consisting of large gold islands attributed to the pattern, and small gold "remnants" in between. The contribution to the absorbance from the small gold remnants is ignored in this treatment since the plasmon absorbance is dominated by larger islands.

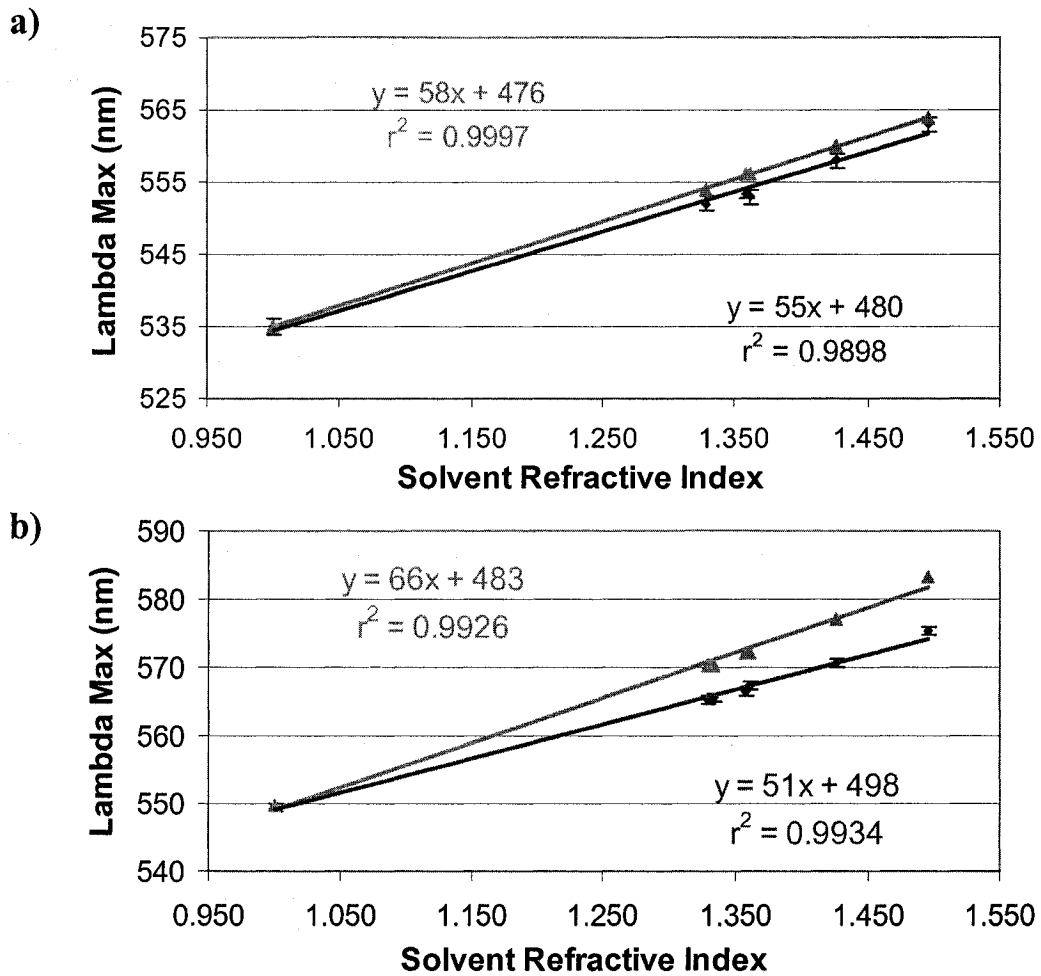


Figure 5-9: Comparison between the experimentally obtained data (blue, circles) and the calculated response (pink, triangles) of Au-Quartz 2 (top) and Au-Quartz 3 (bottom) to media of varying refractive index. The error bars depict \pm one standard deviation (of 3 replicate measurements).

It is clear from Figure 5-9 that the nanoparticle surface plasmon resonance response toward changes in the refractive index of the medium

(i.e. the solvent) is systematically less than predicted. Furthermore, the more oblate nanoparticles used in the sample Au-Quartz 3 exhibit less sensitivity (51 nm/RIU compared to 55 nm/RIU) towards changes in the medium. This is contrary to both theory predictions as well as several reports in the literature, which show increasing sensitivity with increasing aspect ratio^{31,38,58,62,63}. This discrepancy might arise from the detailed structure of the gold islands generated using this methodology. The gold islands are partially embedded, but to an unknown extent, in the quartz substrate. This embedding apparently occurs during the pattern transfer (ion-milling) process and is likely due to a redeposition of quartz, especially where shadowed by the features. This can be observed directly in the form of the craters which remain when the gold is removed for imaging (see Figure 5-2b). The degree to which the gold islands are in contact with the quartz substrate (and therefore not susceptible to changes in the bulk refractive index) is likely different from one sample to the next. Given this, an iterative approach was used to estimate both the degree to which quartz contributes to the effective medium, and the corresponding height of the islands required to approximate the measured peak position. Increasing the contribution of the quartz to the effective medium constant has the effect of red-shifting the plasmon resonance. This in turn was compensated for by reducing the aspect ratio (increasing the

height) of the islands in order to blue shift the resonance back to the vicinity of the resonance peak. As already mentioned, reducing the aspect ratio of the nanoparticles also reduces their sensitivity toward solvent refractive index changes. Therefore, small incremental variations were made to the nanoparticle height and degree of embedding in the quartz until a "best fit" was obtained between the experimental slope and the modelled nanoparticle response. The heights and contributions of quartz to the effective medium constants are listed in Table 5-3. Figure 5-10 shows the final response of the gold island samples with respect to these corrected effective medium constants.

The results plotted in Figure 5-10 are now consistent with both the quasistatic approximation to Mie theory as well as literature examples where higher aspect ratio nanoparticles show greater sensitivity toward refractive index changes^{31,38,62,63}. The sample Au-Quartz 2 is sensing a larger range of effective medium refractive indices in this experiment than Au-Quartz 3 because the gold islands in the latter sample are more deeply embedded in the quartz. Embedding the nanoparticles into the quartz substrate has the effect of limiting the exposure of the nanoparticle to the medium, thus lessening the weighting of the surrounding media on the effective medium refractive index. The result is a loss of sensitivity arising from the reduction of

nanoparticle exposure to the surrounding medium. Figure 5-11 shows this effect by simulating the sensitivity* of oblate nanoparticles embedded to different degrees in the quartz substrate for the gold island aspect ratios studied in this experiment.

Overall, the gold islands show good sensitivity towards the changing medium. The sensitivities obtained were 55 nm/RIU and 51 nm/RIU for gold islands with aspect ratios of approximately 1.7 and 1.9 respectively. These values are in good agreement with the 60 nm/RIU and 100 nm/RIU for gold disks on glass slides measured by Hanarp *et al.*,³¹ with aspect ratios of 1.0 and 3.7 respectively. The sensitivity of nanoparticle arrays towards changes in the bulk surrounding medium can be further optimized by using differently shaped nanoparticles (such as arrays of truncated tetrahedral nanoparticles instead of oblate spheroids⁶⁴) or using silver instead of gold⁶⁴.

* The sensitivity is calculated here as the slope for a plot of λ_{\max} vs. solvent refractive index, in units of nm/refractive index unit (RIU).

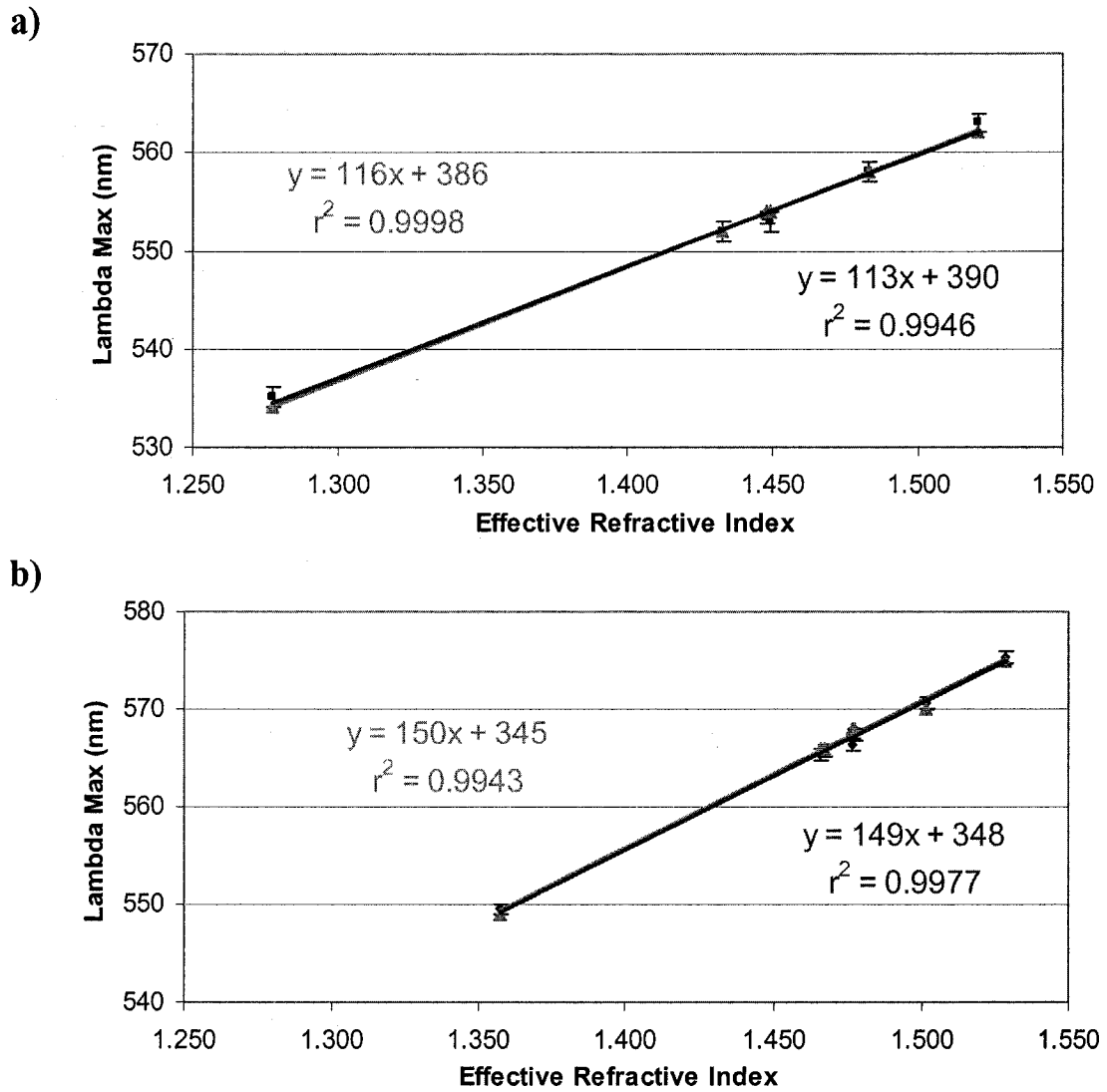


Figure 5-10: Effective medium-corrected responses of Au Quartz 2 (a) and Au Quartz 3 (b). Experimental data are shown in blue (circles), calculated data are shown in pink (triangles).

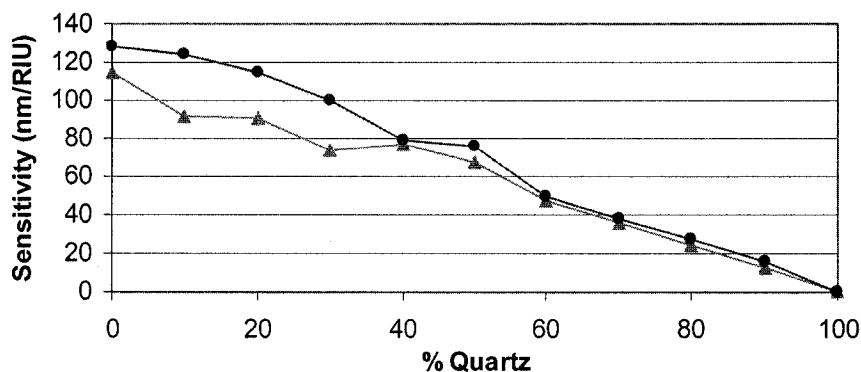


Figure 5-11: The effect of embedding the gold nanoparticles to different extents into the quartz substrate on their sensitivity toward refractive index changes of the surrounding medium. Nanoparticles with aspect ratios of 1.7 and 1.9 are shown in pink (triangles) and blue (circles) respectively.

5.2.3.1 Effect of Monolayer Coverage

Given the sensitivity of nanoparticle plasmon resonance to the surrounding medium, there is great potential to develop a sensor based on the specific adsorption (often through a self-assembled monolayer) of an analyte to the metal surface. In order to demonstrate the sensitivity of the gold islands to short range changes in the medium due to coverage by a molecular monolayer, Au-Quartz 2 and 3 were incubated in 1 mM ethanolic solutions of hexadecanethiol for 19 hours. The UV-vis spectra were measured in nitrogen before and after monolayer formation (shown in Figure 5-12). The peak shifts are summarized in Table 5-4.

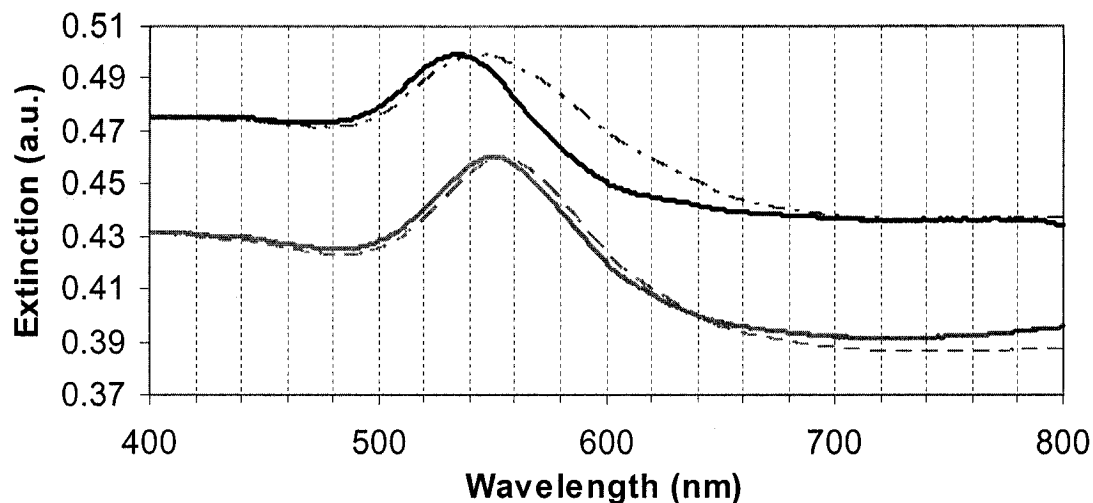


Figure 5-12: Extinction spectra of Au-Quartz 2 (blue, top) and Au-Quartz 3 (pink, bottom), before (solid line) and after (dashed line) $n\text{-C}_{16}\text{H}_{33}\text{SH}$ monolayer formation.

Table 5-4: Effect of alkylthiol adsorption on surface plasmon peak position.

Standard deviations are in brackets.

| Sample | λ_{max} (nm) (bare) | λ_{max} (nm) (plus $n\text{-C}_{16}\text{H}_{33}\text{SH}$) | $\Delta\lambda_{\text{max}}$ (nm) |
|-------------|---------------------------------------|--|-----------------------------------|
| Au-Quartz 2 | 534 (1) | 544 (2) | 10 (2) |
| Au-Quartz 3 | 550 (0) | 555 (1) | 5 (1) |

These peak shifts are comparable to the 6 nm shift observed by Takei *et al.*²⁷ where octadecanethiol was adsorbed onto cap-shape gold nanoparticles, and

the 13 nm resonance shift observed by Haes *et al.*⁶⁴ for truncated tetrahedral gold nanoparticles with an aspect ratio of 1.3. Haes *et al.* also showed that the peak shift associated with oblate nanoparticles is significantly less (~10 nm for silver nanoparticles) than that for truncated tetrahedral nanoparticles. Interestingly, the less oblate gold islands in Au-Quartz 2 give rise to twice the peak shift associated with Au-Quartz 3. Such a large difference in response cannot be accounted for solely by the same effect seen in Figure 5-9, where different effective media parameters affect the overall sensitivity of the nanoparticle surface plasmon resonance.

The short-range effect on the nanoparticle resonance has been recently addressed experimentally and theoretically with a full electrodynamic description by Haes *et al.*⁶⁰. In this case it was also observed that the higher aspect ratio nanoparticles showed less sensitivity toward thiol absorption⁶⁰. Using the discrete dipole approximation developed by Schatz *et al.*⁶², Haes *et al.* show the magnitude of the induced electric field decreases faster with distance from the surface of the nanoparticle around “hot” spots (areas of high induced electric field) than it does around “cold” spots. In effect, they suggest that hot spots contribute more to the average sensitivity for small distances from the surface. On the other hand, it is the cold spots that predominantly contribute to the average sensitivity for large distances

(approximately >15 nm) from the surface. Additionally, it was determined that as the aspect ratio of the nanoparticle was increased by 28%, the magnitude of the electric field at the hot spots of the nanoparticles decreased by 20%, resulting in an overall 14% reduction in peak shift. One of the major factors contributing to this effect was the increased contribution of the substrate to the effective medium dielectric constant for the higher aspect ratio nanoparticles. An increased substrate interaction was found to further decrease the magnitude of the electric field in the vicinity of the hot spots. The magnitude of the electric field (E) due to dipolar resonance along the longitudinal axis has been calculated by Schatz et al. for an oblate spheroid of aspect ratio of 2 (Figure 5-13).⁶⁵ Given the configuration of the gold islands studied in this experiment, the potential hot spots are especially susceptible to becoming partially buried in the quartz substrate during the ion-milling process. This would lead to a pronounced reduction of efficiency of the short-range field of the nanoparticle. The results presented in Table 5-3 clearly suggest that Au-Quartz 3 has more contact with the quartz substrate than does Au-Quartz 2, and it correspondingly shows less sensitivity towards alkylthiol adsorption.

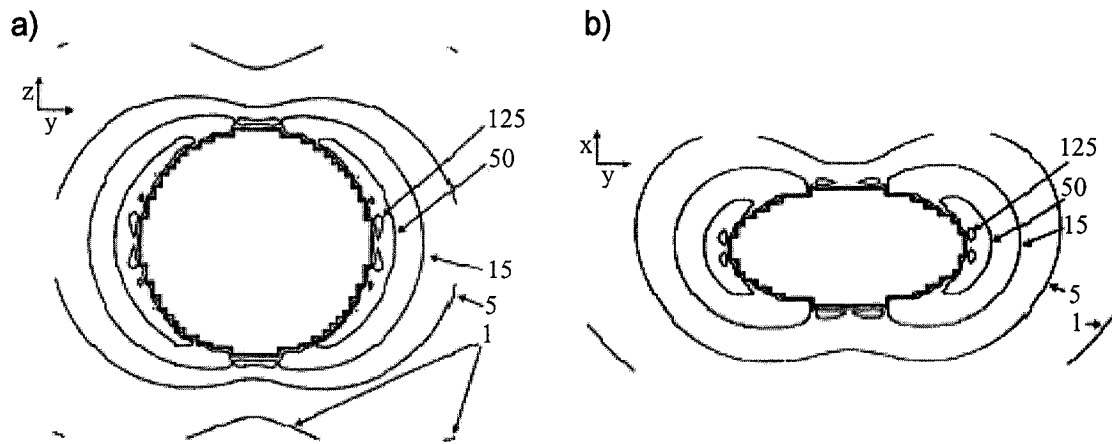


Figure 5-13: Top view (a) and side view (b) of $|E|^2$ for an oblate spheroid with an aspect ratio of 2. Incident polarization is along the y -axis (longitudinal axis), and the numbers correspond to the magnification of the incident field. (Figure adapted from reference 65).

5.3 Conclusions

The extinction of UV-visible light by gold island arrays was measured and found to have very good agreement with calculations made in the quasistatic limit for gold oblate spheroids. The sensitivity of gold island arrays toward different surrounding media, as well as alkythiol adsorption, was also measured and was in good agreement with related literature examples. Gold islands with larger aspect ratios were found to be more sensitive toward long-range changes in the refractive index and less sensitive toward alkythiol adsorption than gold islands with smaller aspect ratios. Particular attention

was paid to the effect of substrate interaction and nanoparticle embedding in the substrate in order to maximize the short and long range sensitivity to the surrounding medium.

References

1. Morales, A. M.; Lieber, C. M. *Science* **1998**, *279*, 208-211.
2. Cuenya, B. R.; Baeck, S.-H.; Jaramillo, T. F.; McFarland, E. W. *J. Am. Chem. Soc.* **2003**, *125*, 12928-12934.
3. Gucci, L.; Petoe, G.; Beck, A.; Frey, K.; Geszti, O.; Molnar, G.; Daroczi, C. *J. Am. Chem. Soc.* **2003**, *125*, 4332-4337.
4. Kumar, R.; Ghosh, A.; Patra, C. R.; Mukherjee, P.; Sastry, M. *Nanotechnology in Catalysis* **2004**, *1*, 111-136.
5. Esumi, K.; Houdatsu, H.; Yoshimura, T. *Langmuir* **2004**, *20*, 2536-2538.
6. Balogh, L. P.; Nigavekar, S. S.; Cook, A. C.; Minc, L.; Khan, M. K. *PharmaChem* **2003**, *2*, 94-99.
7. West, J. L.; Halas, N. J. *Ann. Rev. Biomedical Eng.* **2003**, *5*, 285-292, 4 plates.
8. Yang, P.-H.; Sun, X.; Chiu, J.-F.; Sun, H.; He, Q.-Y. *Bioconjugate Chem.* **2005**, *16*, 494-496.
9. Radt, B.; Smith, T. A.; Caruso, F. *Adv. Mater.* **2004**, *16*, 2184-2189.
10. Maye, M. M.; Lim, I. I. S.; Luo, J.; Rab, Z.; Rabinovich, D.; Liu, T.; Zhong, C.-J. *J. Am. Chem. Soc.* **2005**, *127*, 1519-1529.
11. Tan, W. B.; Zhang, Y. *Int. J. Nanoscience* **2004**, *3*, 685-689.
12. Lamarre, J. M.; Yu, Z.; Harkati, C.; Roorda, S.; Martinu, L. *Thin Solid Films* **2005**, *479*, 232-237.
13. Zhuo, Y.; Yuan, R.; Chai, Y.; Tang, D.; Zhang, Y.; Wang, N.; Li, X.; Zhu, Q. *Electrochem. Commun.* **2005**, *7*, 355-360.
14. Esumi, K.; Matsumoto, T.; Seto, Y.; Yoshimura, T. *J. Colloid Interface Sci.* **2005**, *284*, 199-203.
15. Ito, M.; Tsukatani, T.; Fujihara, H. *J. Mater. Chem.* **2005**, *15*, 960-964.
16. Hsu, S.-h.; Chou, C.-W.; Tseng, S.-M. *Macromol. Mater. Eng.* **2004**, *289*, 1096-1101.

17. Jiang, C.; Markutsya, S.; Pikus, Y.; Tsukruk, V. V. *Nat. Mater.* **2004**, *3*, 721-728.
18. Genov, D. A.; Sarychev, A. K.; Shalaev, V. M.; Wei, A. *Nano Lett.* **2004**, *4*, 153-158.
19. Wei, A.; Kim, B.; Sadtler, B.; Tripp, S. L. *ChemPhysChem* **2001**, *2*, 743-745.
20. Schatz, G. C.; Van Duyne, R. P. In *Handbook of Vibrational Spectroscopy*, Chalmers, J. M., Griffiths, P. R., Eds.; John Wiley: Chichester, 2002.
21. Maier, S. A.; Brongersma, M. L.; Kik, P. G.; Atwater, H. A. *Phys. Rev. B* **2002**, *65*, 193408/1-193408/4.
22. Wei, Q. H.; Su, K. H.; Durant, S.; Zhang, X. *Nano Lett.* **2004**, *4*, 1067-1071.
23. Quinten, M.; Leitner, A.; Krenn, J. R.; Aussenegg, F. R. *Opt. Lett.* **1998**, *23*, 1331-1333.
24. Haes, A. J.; Van Duyne, R. P. *J. Am. Chem. Soc.* **2002**, *124*, 10596-10604.
25. Rosi, N. L.; Mirkin, C. A. *Chem. Rev.* **2005**, *105*, 1547-1562.
26. Hutter, E.; Pileni, M.-P. *J. Phys. Chem. B* **2003**, *107*, 6497-6499.
27. Himmelhaus, M.; Takei, H. *Sens. Actuators, B* **2000**, *B63*, 24-30.
28. Nath, N.; Chilkoti, A. *Anal. Chem.* **2002**, *74*, 504-509.
29. Zhang, H. L.; Evans, S. D.; Henderson, J. R.; Miles, R. E.; Shen, T. H. *Nanotechnology* **2002**, *13*, 439-444.
30. Atay, T.; Song, J.-H.; Nurmikko, A. V. *Nano Lett.* **2004**, *4*, 1627-1631.
31. Hanarp, P.; Kaell, M.; Sutherland, D. S. *J. Phys. Chem. B* **2003**, *107*, 5768-5772.
32. Haynes, C. L.; McFarland, A. D.; Zhao, L.; Van Duyne, R. P.; Schatz, G. C.; Gunnarsson, L.; Prikulis, J.; Kasemo, B.; Kaell, M. *J. Phys. Chem. B* **2003**, *107*, 7337-7342.

33. Bohren, C. F.; Huffman, D. R. *Absorption and Scattering of Light by Small Particles*; John Wiley & Sons, Inc.: New York, 1983.
34. Reproducible measurements in nitrogen were obtained after repeated cycling through the UV/Ozone and rinsing process.
35. Faraday, M. *Philos. Trans.* **1857**, *147*, 145.
36. Mie, G. *Ann. Phys.* **1908**, *25*, 377-445.
37. Kreibig, U.; Vollmer, M. *Optical Properties of Metal Clusters*; Springer: Berlin, 1995.
38. Link, S.; El-Sayed, M. A. *J. Phys. Chem. B* **1999**, *103*, 8410-8426.
39. Asano, S. *Appl. Opt.* **1979**, *18*, 712-723.
40. Asano, S.; Yamamoto, G. *Appl. Opt.* **1975**, *14*, 29-49.
41. Voshchinnikov, N. V.; Farafonov, V. G. *Astrophys. Space Sci.* **1993**, *204*, 19-86.
42. Maxwell Garnett, J. C. *Philos. Trans. R. Soc.* **1904**, *A203*, 385-420.
43. Bruggeman, D. A. G. *Ann. Phys. (Leipzig)* **1935**, *24*, 636-679.
44. Genzel, L.; Martin, T. P. *Surf. Sci.* **1972**, *34*, 33-49.
45. Barker, A. S. *Phys. Rev.* **1973**, *B7*, 2507-2520.
46. Bohren, C. F.; Wickramasinghe, N. C. *Astrophys. Space Sci.* **1977**, *50*, 461-472.
47. Gotschy, W.; Vonmetz, K.; Leitner, A.; Aussenegg, F. R. *Appl. Phys. B.* **1996**, *63*, 381-384.
48. Johnson, P. B.; Christy, R. W. *Phys. Rev. B* **1972**, *6*, 4370-9.
49. Malynych, S.; Chumanov, G. *J. Am. Chem. Soc.* **2003**, *125*, 2896-2898.
50. Lamprecht, B.; Schider, G.; Lechner, R. T.; Ditlbacher, H.; Krenn, J. R.; Leitner, A.; Aussenegg, F. R. *Phys. Rev. Lett.* **2000**, *84*, 4721-4724.
51. Taton, T. A.; Mirkin, C. A.; Letsinger, R. L. *Science* **2000**, *289*, 1757-1760.
52. Malinsky, M. D.; Kelly, K. L.; Schatz, G. C.; Van Duyne, R. P. *J. Am. Chem. Soc.* **2001**, *123*, 1471-1482.

53. Yguerabide, J.; Yguerabide, E. E. *Anal. Biochem.* **1998**, *262*, 157-176.
54. Yguerabide, J.; Yguerabide, E. E. *Anal. Biochem.* **1998**, *262*, 137-156.
55. Storhoff, J. J.; Lazarides, A. A.; Mucic, R. C.; Mirkin, C. A.; Letsinger, R. L.; Schatz, G. C. *J. Am. Chem. Soc.* **2000**, *122*, 4640-4650.
56. Henglein, A.; Meisel, D. *J. Phys. Chem. B* **1998**, *102*, 8364-8366.
57. Hulteen, J. C.; Treichel, D. A.; Smith, M. T.; Duval, M. L.; Jensen, T. R.; Van Duyne, R. P. *J. Phys. Chem. B* **1999**, *103*, 3854-3863.
58. Xu, H.; Kall, M. *Sens. Actuators, B* **2002**, *B87*, 244-249.
59. Kelly, K. L.; Jensen, T. R.; Lazarides, A. A.; Schatz, G. C. *Metal Nanoparticles* **2002**, 89-118.
60. Haes, A. J.; Zou, S.; Schatz, G. C.; Van Duyne, R. P. *J. Phys. Chem. B* **2004**, *108*, 109-116.
61. Zhao, L.; Kelly, K. L.; Schatz, G. C. *J. Phys. Chem. B* **2003**, *107*, 7343-7350.
62. Kelly, K. L.; Coronado, E.; Zhao, L. L.; Schatz, G. C. *J. Phys. Chem. B* **2003**, *107*, 668-677.
63. Jensen, T. R.; Malinsky, M. D.; Haynes, C. L.; Van Duyne, R. P. *J. Phys. Chem. B* **2000**, *104*, 10549-10556.
64. Haes, A. J.; Zou, S.; Schatz, G. C.; Van Duyne, R. P. *J. Phys. Chem. B* **2004**, *108*, 6961-6968.
65. Jensen, T.; Kelly, L.; Lazarides, A.; Schatz, G. C. *J. Cluster Sci.* **1999**, *10*, 295-317.

Chapter 6

Conclusions, Original Contributions to Knowledge, and Ideas for Future Work

6.1 Overview and Conclusions

This section will summarize the conclusions of each Chapter, as well as those drawn from the Thesis as a whole.

Chapter 2: Monolayer films of surface micelle arrays, derived from polystyrene-*b*-poly(2-vinylpyridine) self-assembled at the air-water interface, were used as sacrificial masks for the transfer of patterned nanoscale topology into surfaces. From this study, we conclude that:

1. Argon ion-milling of the polymer film-coated substrates results in a high-fidelity transfer of topological features to the substrate. The methodology is applicable to many substrates, given that they are sufficiently smooth ($\sim 1\text{nm}$ rms roughness over $1\ \mu\text{m}^2$), and present a similar ion-milling rate compared to the polymer film.
2. 180 s of ion-milling is required to remove the majority of the polymer film ($\sim 90\%$), to the bulk Si, Au, and SiO_2 substrate.

3. Friction force imaging of the nanopatterned substrates reveals striking contrast between the patterned features and the flat substrate. The friction contrast is believed to arise from nanoscale roughness introduced from the ion-milling process and curvature of the features, *not chemical contrast*, which is the common interpretation of LFM-measured friction contrast.

Chapter 3: Monolayer films of surface micelle arrays were explored as sacrificial masks for the creation of patterned gold islands (nanoparticles) on a variety of substrates. From this study, we conclude that:

1. Argon ion-milling of the polymer film-coated substrates results in a high-fidelity transfer of topological features to the substrate. The methodology is believed to be applicable to many substrate/film combinations, given that both are sufficiently smooth ($\sim 1\text{nm}$ rms roughness over $1\ \mu\text{m}^2$), and particularly if the film presents a faster ion-milling rate compared to the polymer film or substrate.
2. Contrast observed in the FEGSEM imaging of distinct gold islands is opposite that of continuous, nanopatterned gold films and can be used to track the formation of distinct gold islands.

3. In the case of a Si/SiO_x substrate, the gold islands are formed, and slightly embedded in a “nano-pillar” of Si/SiO_x, whereas in the case of a mica substrate, they are formed directly on the substrate. This is the likely result of the exceptionally low ion-milling rate observed for mica.

Chapter 4: The contact angle made between small drops of water and nanopatterned surfaces was measured and compared to measurements made on flat counterparts. We conclude that:

1. The observed contact angle is the result of complete wetting of the nanostructured interface by water (Wenzel-type wetting).
2. Wenzel-type and not Cassie-type wetting is the preferred configuration associated with the topology and surface energies (chemical compositions) explored in this experiment.
3. The current phenomenological model predicts that increasing the height of the nanopatterned features to ~ 180 nm in a gold island pattern derivatized with octadecanethiol will make the Cassie-type wetting situation equally favourable to the Wenzel-type situation.

Chapter 5: The extinction of light by gold nanoparticles generated using the block copolymer patterning methodology was explored with respect to the

quasistatic approximation to Mie theory, the effect of different solvent media, and the effect of adsorption of an alkylthiol monolayer. We conclude that:

1. The quasistatic approximation is effective in predicting peak positions of extinction maxima associated with the surface plasmon resonance of isolated, quasi-ordered gold island arrays.

2. The substrate has a significant effect on the optical properties of gold nanoparticles made using this methodology due to fact that they are partially embedded in the substrate during the pattern transfer process.

This can have significant implications on the sensitivity of the nanoparticle surface plasmon resonance towards long-range and short-range changes in the effective medium.

As a whole, this Thesis has explored issues pertaining to making and measuring nanostructured surfaces using the block copolymer patterning methodology, and characterizing the properties of the resulting patterns. It was found that the methodology can reliably create high-fidelity surface patterns which can have interesting surface wettability and optical properties. However, deliberate exploration of these properties requires secondary elaboration of the pattern aspect ratio either *via* selective chemistry, or using

more chemically selective pattern transfer method (such as reactive ion beam etching).

6.2 Original Contributions to Knowledge

1. An original methodology for patterning topology on a surface using block copolymer surface micelle arrays is described. The methodology readily generates 5 nm thick circular features of 50 nm diameter, with a center-to-center spacing of 110 nm, and can be changed with a change in block length of the block copolymer starting material.
2. An original methodology for creating nanoparticle arrays on surfaces is described.
3. Characterisation of these unique nanopatterned surfaces by lateral force microscopy, field emission (gun) scanning electron microscopy (FEGSEM), and contact angle measurements were obtained for the first time.
4. Optical characterisation of uniquely patterned gold nanoparticle arrays was obtained for the first time.

6.3 Ideas for Future Work

1. Increasing the Aspect Ratio of the Surface Features

Increasing the aspect ratio of the a) the mask and b) the final structures are both of vital importance in using the block copolymer patterning methodology in-depth studies of wetting/dewetting of films of water, polymers, metals, etc. for secondary pattern decoration. Several efforts have been made to this end throughout the duration of this doctoral project: chemical etching using KOH and single crystal silicon wafers, chemical vapour deposition using SiCl_4 and H_2 (g) at elevated temperatures on gold island-patterned substrates (where gold is believed to act as a catalyst toward Si whisker nucleation), and some (minimal) reactive ion etching (CF_4 , Cl_2 , I_2) through the polymer mask, as well as through gold islands as a mask for silicon. The latter two methods have been met with some success so far. In the former, silicon whiskers have been grown to long lengths (μm 's) but with diameters corresponding to that of the gold islands (~ 30 nm). However, the challenge still remains to create silicon whiskers anisotropically *upwards* (epitaxially) from the substrate. Moreover, there are significant challenges in creating a reproducible synthesis of these whiskers. In the latter, the use of RIE to selectively etch silicon over gold has been demonstrated, and is expected to eventually yield maximum etch depths of ~ 50 nm for a 30nm diameter gold nanoparticle mask. However, RIE or other chemical etching mechanisms, combined with the block copolymer mask has yet to be

explored, in the case of the block copolymer masks used here (PS-P2VP) and others (PS-PEO, PS-PMMA, etc.) this may provide an alternative route for patterning features with greater aspect ratios than obtained in this work.

2. Surface plasmon resonance studies

The exploration of the effects of applied potential to the gold islands/nanoparticles, especially with immersion in highly polarizable media, and control over interparticle spacing *via* the choice of a shorter P2VP block length to < 30 nm will present an intriguing system for studying the mediation of short-range electronic coupling. Preliminary work with amorphous gold islands on indium tin oxide (ITO)^a looked at the effect of applied potential on the localized surface plasmon resonance frequency and sensitivity to localized dielectric changes in the surrounding medium. Applying -1V to these surfaces (with respect to a Ag/AgCl electrode) in sodium fluoride solution resulted in a 15 (2) nm blue shift. However, a proper spectroelectrochemical cell is required in order to perform further experiments and eliminate reactions with oxygen under a broad range of applied potentials.

^a "Amorphous gold islands" result from the evaporation of a thin (~4-5 nm), discontinuous layer of Au onto ITO substrates.

Appendix 1:

Supplementary Information for Chapter 2

1.1 Langmuir films of PS-*b*-P2VP

The interfacial properties of polystyrene-*b*-poly(2-vinylpyridine) at the air-water interface was explored in depth by Zhu et al.¹⁻⁶

A typical surface pressure-area isotherm is shown below of PS₅₁₀-*b*-P2VP₄₈₀ obtained at 23°C, spread from a 0.5mg/ml chloroform solution (see Chapter 2 for details).

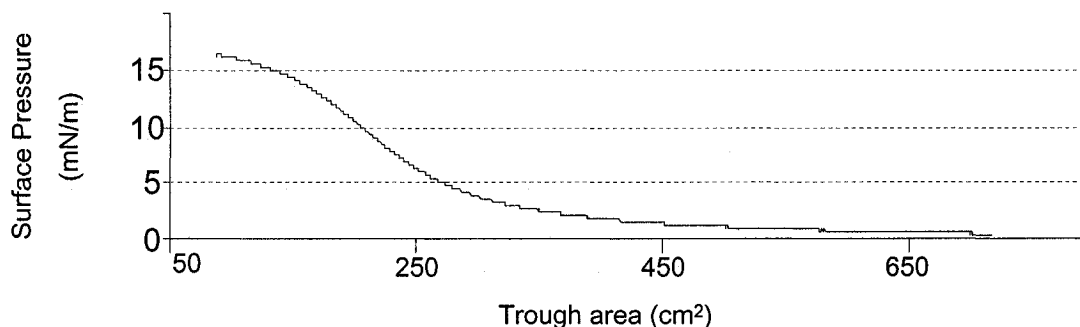


Figure A-1: A typical Pressure-Area isotherm for PS-P2VP spread at the air-water interface.

Langmuir-Blodgett deposition of these films was performed at 2 mN/m. At this pressure it is believed that the P2VP corona of adjacent surface micelles are in slight contact with one another, however compression and/or interdigitation of the PVP chains is considered to be minimal¹.

1.2 The Effect of Different Substrate Properties on the Feasibility of Pattern Transfer

1.2.1 Substrate Roughness

Because the aspect ratio of the surface micelles made from polystyrene-*b*-poly(2-vinylpyridine) is relatively small (i.e. 1:10), and a chemically *unselective* pattern-transfer method is used, roughness in the substrate that one wishes to pattern is probably the main factor limiting this methodology. To demonstrate, AFM images of gold substrates prepared in different ways are provided in Figure A-2. The most common method of preparation is thermal evaporation. Gold is evaporated and deposited onto a substrate (located about 12 inches above the source) whereupon it nucleates and grows into a continuous film^a. Figure 1 shows two substrates (Si/SiO_x and mica) onto which ~ 200 nm of gold was deposited. A PS-P2VP film was subsequently deposited using the Langmuir-Blodgett technique. The gold evaporated onto Si/SiO_x has a rough morphology (~ 1.5 nm rms roughness over 1 μm²) due to grains of gold which are comparable in size (~30-50 nm) to the surface micelle pattern.

^a Evaporation was typically done at a rate of 1.4 Å/s, start from a base pressure of ~9x10⁻⁷ torr.

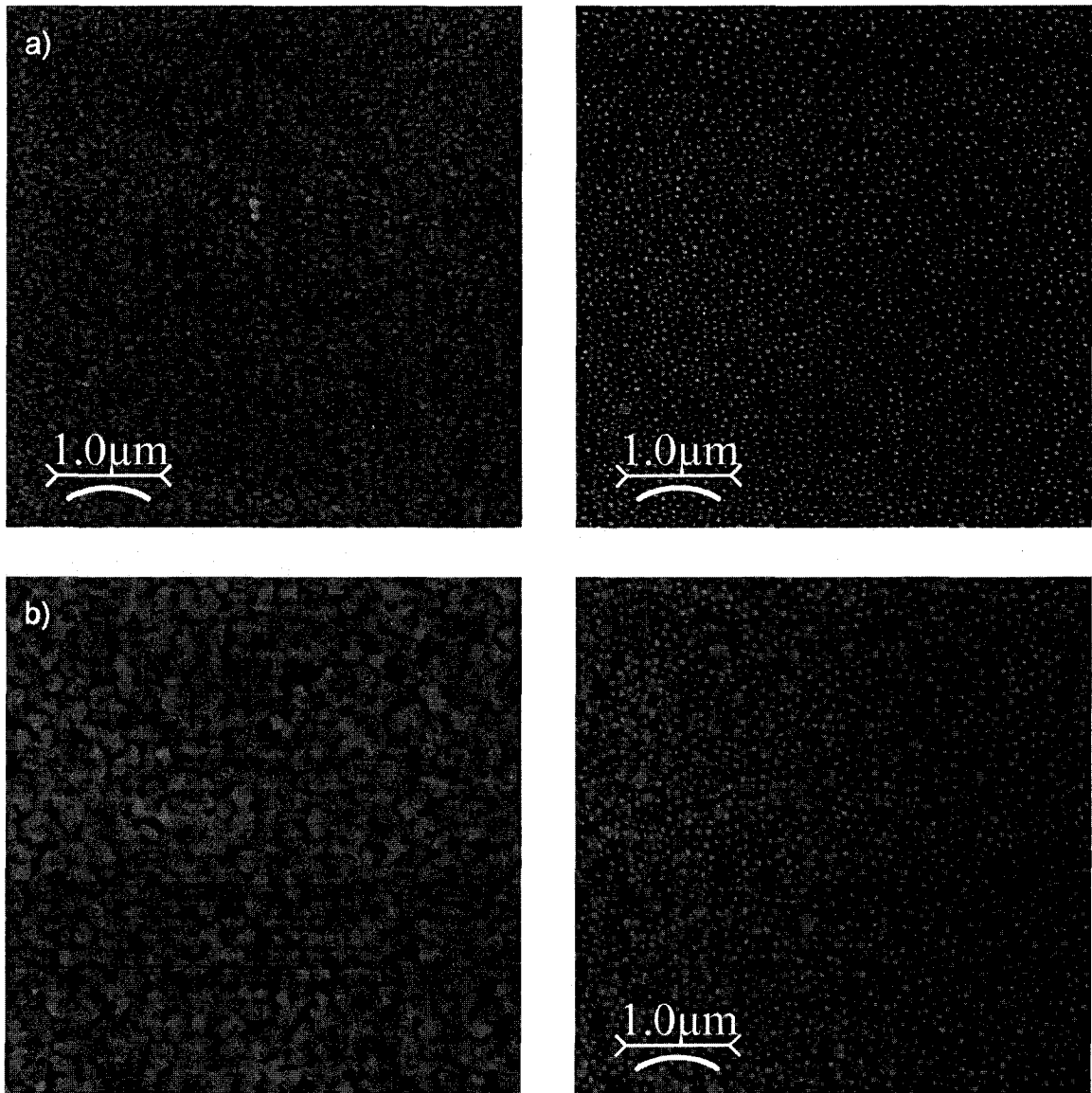


Figure A-2: 5 μm x 5 μm AFM (topography) images of gold evaporated on a) Si/SiO_x and b) mica with (right) and without (left) block copolymer film coating.

Once superimposed, the topology of the surface micelle film is not discernible from this type of gold substrate. An unselective ion-milling process will give in turn give rise to a similar topology as seen in Figure A-2a. Unlike Si/SiO_x,

gold evaporated onto mica grows in large flat grains, although the RMS roughness is 1.22 nm over 1 μm^2 , due to the voids in between adjacent grains. Since the grains of gold on mica are large and flat the topology of the surface micelle pattern is easily identified and remains discernable after ion-milling.

Sputter-deposited gold was also found to be suitably smooth to pattern, as was seen in Chapter 3. The best gold substrate found was made by evaporating a gold film onto Si/SiO_x, gluing the exposed gold surface to another substrate such as a glass slide, and then separating the gold film from the Si/SiO_x “template”, exposing a flat gold surface (Figure A-3a).

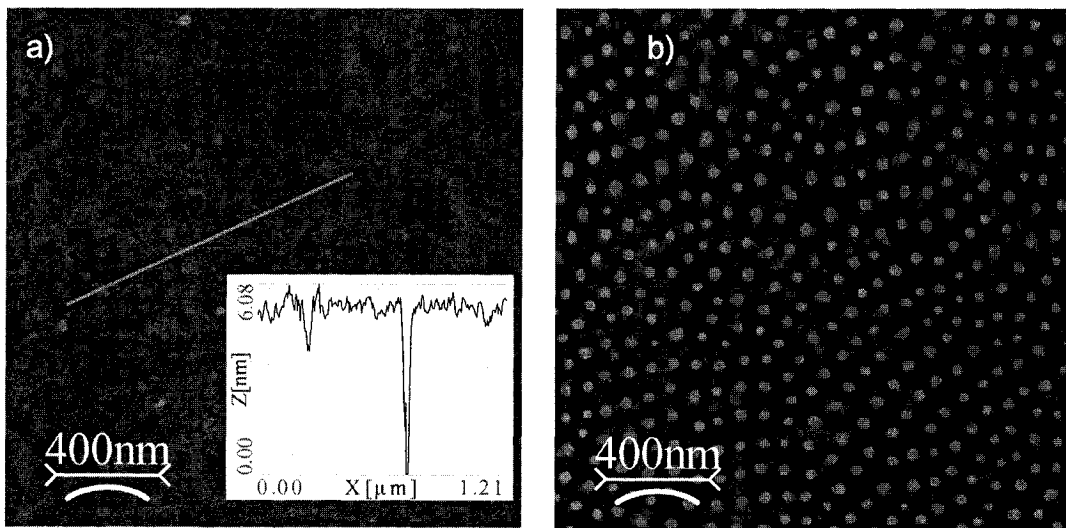


Figure A-3: AFM (topography) images of template-stripped gold surface before (a) and after (b) nanopatterning. Cross-section line scan for line drawn in (a) is shown in inset.

1.2.2 Hydrophobic and Hydrophilic Substrates

Another factor limiting the generality of this pattern transfer methodology is the substrate related to the purposes of the Langmuir-Blodgett (LB) deposition of the polymer film. Extremely hydrophilic substrates that chemically dissolve or react with water are not suitable for LB films as they must be submerged in the aqueous phase until film transfer begins (typically around 1 hour). Extremely hydrophobic substrates pose a problem of a different sort for LB deposition. In order for film transfer to be successful, the film must be able to wet/adhere to the substrate. In the LB technique, the components of the film in contact with the aqueous phase (the most hydrophilic components) are the components of the film which are in direct contact with the substrate. If the film does not wet the substrate, contact instabilities arise, and the film may slip across the substrate until it adheres to another spot. This slip-stick phenomenon is believed to have occurred for the transfer of PS-P2VP at the air-water interface to a highly ordered pyrolytic graphite (HOPG) substrate (Figure A-4). One way to circumvent these problems could be the Langmuir-Schaeffer deposition in which a substrate is lowered onto the film in the horizontal position (parallel to the subphase) until contact with the film is made. This deposition method is, however, more difficult to control.

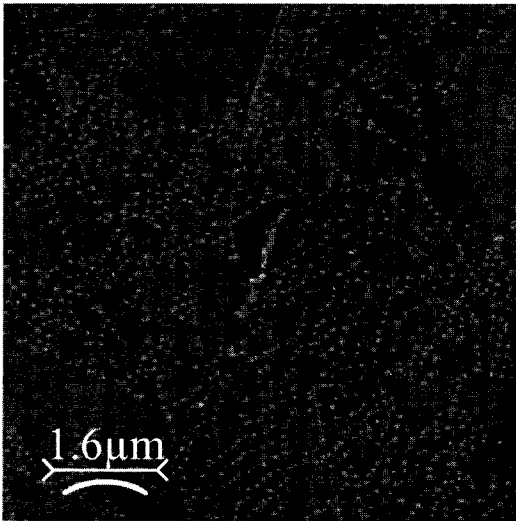


Figure A-4: AFM (topography) image of an LB-deposited film of PS-P2VP surface micelles onto HOPG.

1.2.3 Refractory Substrates

Refractory substrates (materials that can withstand extremely high temperatures) also restrict the generality of this nanopatterning methodology by being resistant to the ion-milling pattern transfer step. Ion-milling of these materials is extremely slow compared to that of the polymer resist. As in the case of mica, minimal pattern transfer occurs because the polymer film is milled away before the mica is removed (Figure A-5).

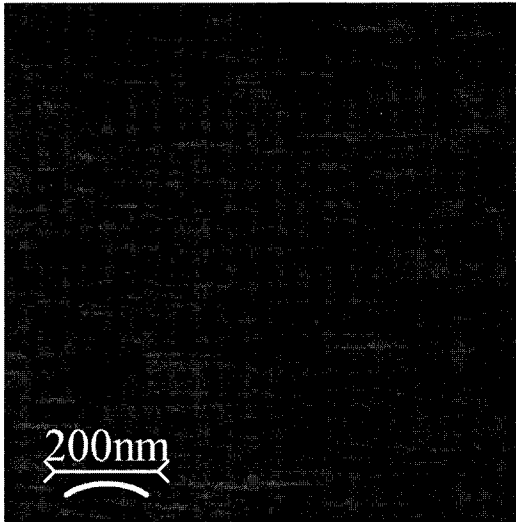


Figure A-5: AFM image (height ranges from 0-5 nm) of mica after ion-milling (180 s) to remove the PS-P2VP polymer film for pattern-transfer.

Because argon ion-milling occurs mainly through a physical process, introducing chemical selectivity to the pattern transfer step, by using reactive ions or a chemical etch, is one way to circumvent the problem that refractory materials present to this methodology. Alternatively, using higher aspect ratio (thicker) films of surface micelle arrays, where the micelle core is considerably thicker than 5 nm, would also alleviate the problem, albeit to a lesser degree.

References

1. Zhu, J.; Lennox, R. B.; Eisenberg, A. *Langmuir* 1991, 7, 1579-84.
2. Zhu, J.; Eisenberg, A.; Lennox, R. B. *J. Am. Chem. Soc.* 1991, 113, 5583-8.
3. Zhu, J.; Eisenberg, A.; Lennox, R. B. *Macromolecules* 1992, 25, 6556-62.
4. Zhu, J.; Eisenberg, A.; Lennox, R. B. *Macromolecules* 1992, 25, 6547-55.
5. Zhu, J.; Hanley, S.; Eisenberg, A.; Lennox, R. B. *Makromol. Chem.* 1992, 53, 211-20.
6. Zhu, J.; Lennox, R. B.; Eisenberg, A. *J. Phys. Chem.* 1992, 96, 4727-30.

Appendix 2:

Further Details Concerning Making Gold Island Arrays

2.1 Elemental Analysis of Gold Island Arrays

Energy-dispersive x-ray spectroscopy (EDS or EDX) was used to detect the (qualitative) presence of Au in the gold island arrays on Si/SiO_x.

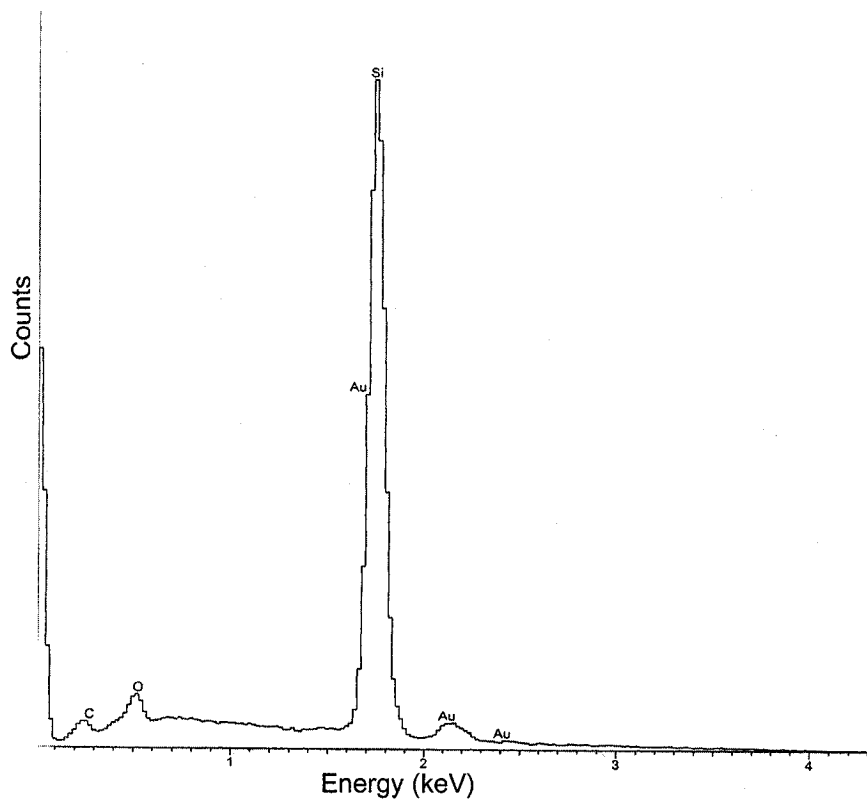


Figure A-6: EDS spectrum of gold islands patterned on Si/SiO_x. Spectrum was obtained on the Hitachi S-4700 FEGSEM, using a beam energy of 15 kV, and obtained after 7000 counts.

As shown in Figure A-6, Au is definitively shown to be on the surface of the ion-milled and imaged samples. This is verification that the images are indeed of Au islands.

2.2 Surface Resistance during Pattern Transfer

During the pattern transfer process (argon ion-milling) associated with fabrication of gold island arrays (Chapter 3), the surface resistance was measured in order to correlate resistance changes with the removal of gold in between the patterned features.

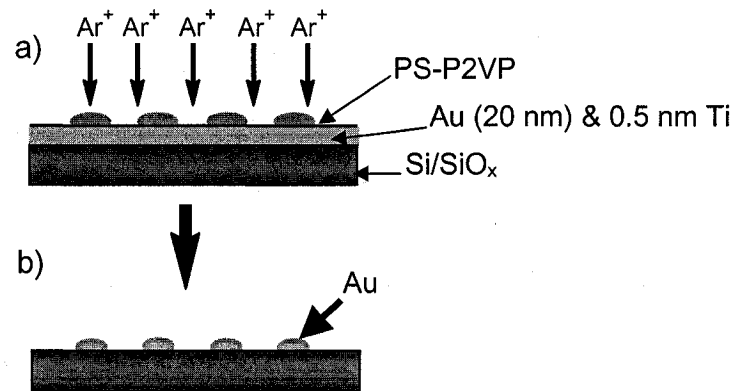


Figure A-7: Schematic cross-section view of the pattern-transfer methodology. a) film of surface micelles covering a substrate consisting of a thin gold film adhered to Si/SiO_x with a 0.5 nm Ti layer. Ar⁺-milling removes material from the surface, transferring the topology of the mask. b) Ar⁺-milling is stopped once the gold located between PS-masked domains has been removed, leaving an array of Au islands on Si/SiO_x.

The resistance across the surface of a silicon wafer (n-doped) coated with a thin (~20 nm) gold film and the block copolymer surface micellar film, was tracked as a function of ion-milling time. Measurements were made using a multimeter (Fluke 175) by gently touching the probes, spaced ~0.5 cm apart, to the surface within 30 s of removal from vacuum. The uncertainty was estimated by taking at least 3 measurements at different spots on the same sample. FEGSEM images were obtained for other ion-milled samples whose similar resistance values span the range measured.

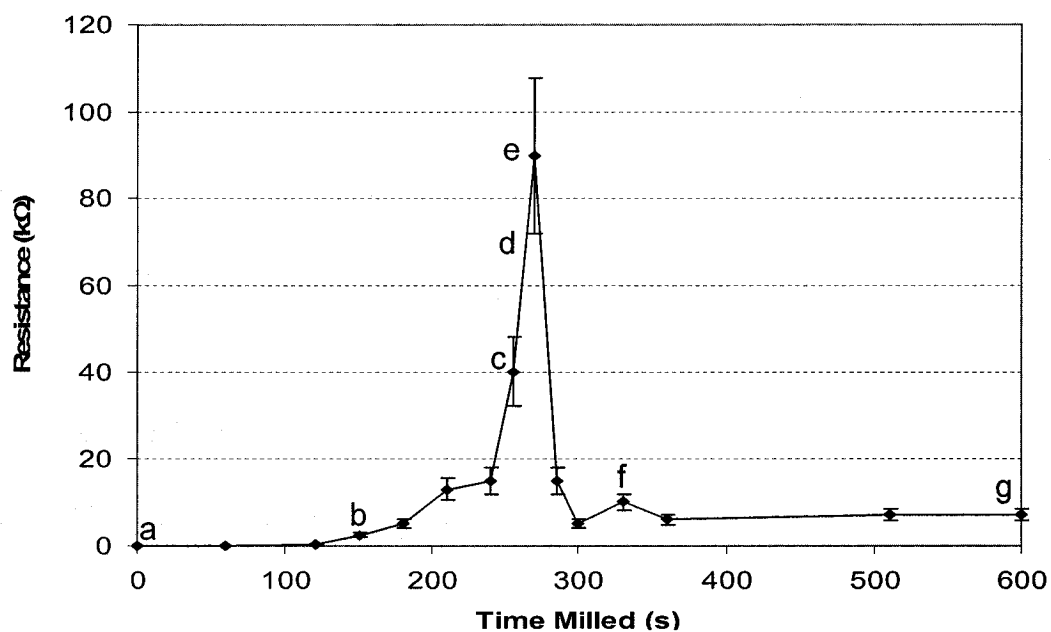


Figure A-8: Variation of the resistance across the surface of a sample with exposure to the Ar⁺-milling conditions. The sample (silicon wafer) was initially coated (0s) with a thin gold film and block copolymer sacrificial mask (see Figure A-7a). a-g refer to the images shown in Figure A-9.

Appendix 2

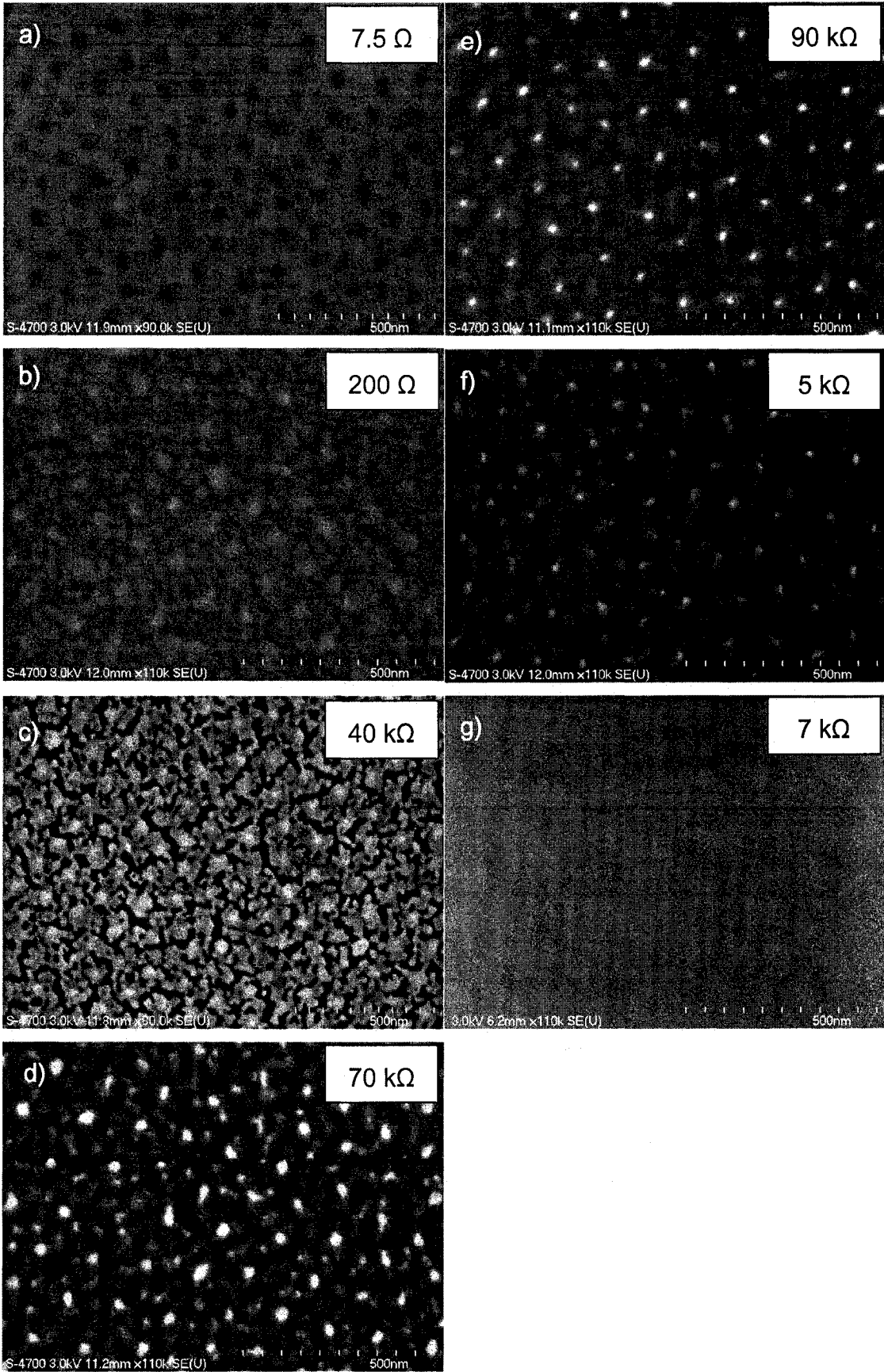


Figure A-9: FEGSEM secondary electron images of the progressive ion-milling of a block copolymer/Au-coated silicon wafer. Inset: measured resistance for each sample.

One can see in Figure A-8 and Figure A-9 that there is a correlation between the surface resistance and the ion-milling time. At $t = 0$ s the resistance is very low and corresponds to that of a gold film. It is likely that because the block copolymer film is so thin, the method used to measure the surface resistance is insensitive to such a thin film. Once the ion-milling is initiated, the resistance increases slowly as more and more of the gold film is etched, developing cracks in the film. The morphology of the gold film, consisting of small and randomly oriented crystalline Au domains, is thought to determine the crack formation. Ion-milling is known to exaggerate surface roughness by virtue of faster milling rates at edges and grain boundaries. After about 3 minutes of ion-milling, the resistance rises quickly during which time the measurement also becomes increasingly noisy. At the point where there are large voids in the gold film (*ca.* 40 k Ω measured resistance), the film is still mostly continuous. At this point, electrons can likely choose percolation paths through the gold film. However, continued etching leads to a continued rise in the resistance to ~ 90 k Ω , at which point the FEGSEM image (Figure A-9e)

shows an array of distinct gold islands. The high resistance measured here is puzzling given that the resistance of the silicon substrate is $<10\text{ k}\Omega$. One possibility is that at $90\text{ k}\Omega$, the native oxide layer (SiO_x), present on the silicon wafer before coated with Au, while very thin (typically 2-5 nm) is sufficiently insulating to create a barrier to current flow. Additional ion-milling after this point results in removal of more Au and SiO_x , making it easier to pass current through the silicon substrate.

Unfortunately, the large uncertainty in the resistance, particularly at high resistance, and slightly varying thicknesses of the gold film across samples, makes this resistance measurement a poor protocol to monitor the ion-milling process. A more stable measurement, such as a 4-point probe method, performed *in situ*, is needed in order to do real-time monitoring of the pattern transfer process.

2.3 Making Au Islands on ITO

Chapter 3 describes the generation of Au island arrays on both Si/ SiO_x and mica substrates, and Chapter 5 describes the synthesis of Au island patterns on quartz. Indium tin oxide (ITO) has also been successfully implemented in this methodology in order to make substrates suitable for spectroelectrochemical studies. Thin films of ITO are commonly used for such studies as they are mostly transparent in the UV-visible spectrum, and

they are conducting. Cleaning of ITO films on glass substrates (150-200nm thick, Delta Technologies Inc.) was performed in the conventional way (by immersing in recently boiled, hot 50:50 chloroform/ethanol solution followed by 2 mins bath sonication). 0.5 nm Ti was sputter-deposited onto a thin gold film (~20 nm), onto which the LB polystyrene-*b*-poly-2-vinylpyridine surface micellar film was deposited. The substrates were then ion-milled at 6.5 kV, 3.5 $\mu\text{A}/\text{cm}^2$ (rocked at 40°/s from 0-50° from surface normal, 60 rpm rotation) for ~300 s, until distinct Au islands were observed by FEGSEM imaging (Figure A-10).

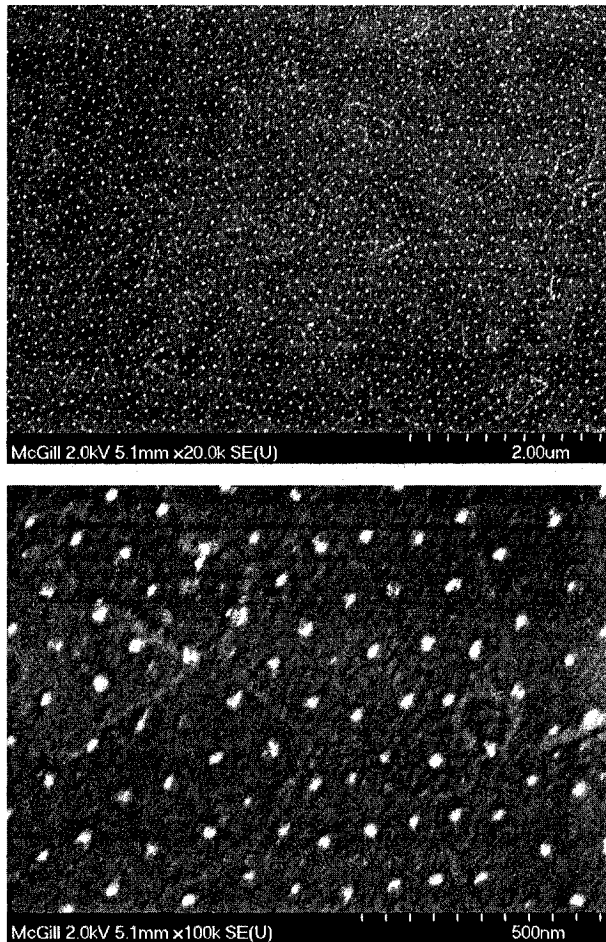


Figure A-10: FEGSEM images (top at 20,000X, bottom at 100,000X magnification) of pattern-transfer after 330s of Ar⁺-milling to result in gold islands on ITO substrate.

Transmission mode UV-vis spectroscopy (Cary5000, Varian) was performed on these substrates. Curiously, these gold islands do not show an observable peak in the UV-vis transmission mode spectra (Figure A-11), unlike the gold islands on quartz. Unlike the quartz substrates, ITO-glass substrates have non-negligible absorption in the UV-vis. Additionally,

different ITO film thicknesses between sample and reference (milled or unmilled ITO-glass substrate) are a consequence of the pattern-transfer process (ion-milling) and make accurate blank-subtraction difficult to obtain. This effect, coupled with the low gold island concentration (leading to low extinction) may result in the inability to detect the surface plasmon resonance response of these nanoparticles.

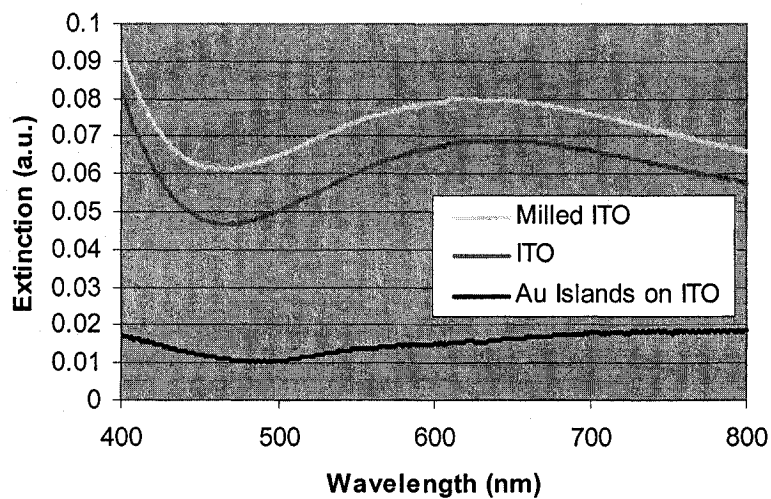


Figure A-11: Transmission UV-vis spectra for Au islands on ITO (spectrum shown in blue has been blank-subtracted using an ion-milled ITO substrate as a blank). A milled ITO (yellow) and unmilled ITO substrate (pink) is also shown.

Appendix 3: Calculation of r and f (Chapter 4)

The contact ratios, r and f , were calculated in order to estimate the apparent contact angles defined by Wenzel (equation 1) or Cassie (equation 2).

$$\cos \theta_w = r \cos \theta \quad \text{Equation 1}$$

$$\cos \theta_c = \sum f_i \cos \theta_i \quad \text{Equation 2}$$

where r is the ratio of the total area in contact with the liquid to the projected area and f is the fraction of the area of the solid in contact with the drop to the projected area. The shape of the nanostructures was approximated using cylinders of the same radius and height as measured by AFM (Table 4-1).

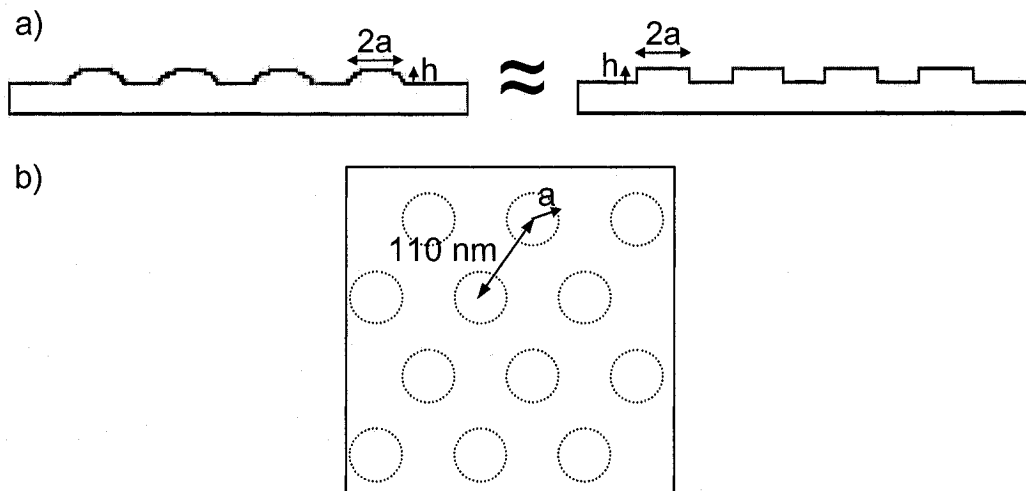


Figure A-12: Schematic of the side profile (a) and top view (b) of the nanostructured surfaces studied in Chapter 4.

Given that the areal density of the pattern is $\sim 1 \times 10^{14}$ features/m², r and f were then calculated as follows.

$$r = \frac{\text{Total Surface Area}}{\text{Projected Area}} = \frac{10^{14} (SA) + (1 - 10^{14} \pi a^2)}{1m^2} \quad \text{Equation 3}$$

$$f = \frac{\text{Surface Area in Contact}}{\text{Projected Area}} = \frac{10^{14} \pi a^2}{1m^2} \quad \text{Equation 4}$$

$$SA = 2\pi ah + \pi a^2 \quad \text{Equation 5}$$

where a is the feature radius (m), h is the feature height (m), and SA is the surface area of a cylinder.

For example, for the patterned Si/SiO_x sample described in Table 4.1, ($h = 4.0$ nm, $a = 28$ nm), the calculation is as follows.

$$\begin{aligned} SA &= 2\pi(28 \times 10^{-9} m)(4.0 \times 10^{-9} m) + \pi(28 \times 10^{-9} m)^2 \\ &= 3.17 \times 10^{-15} m^2 \end{aligned}$$

$$r = \frac{10^{14} (3.17 \times 10^{-15} m^2) + [1 - 10^{14} \pi (28 \times 10^{-9} m)^2]}{1m^2} = 1.07$$

$$f = \frac{10^{14} \pi (28 \times 10^{-9} m)^2}{1m^2} = 0.25$$

Appendix 4: Calculation of p_{quartz} (Chapter 5)

The fraction of surface area of an oblate gold nanoparticle in contact with its quartz substrate is p_{quartz} . The surface area of an oblate spheroid can be calculated as a surface of revolution; i.e. by rotating an ellipse around its minor axis.

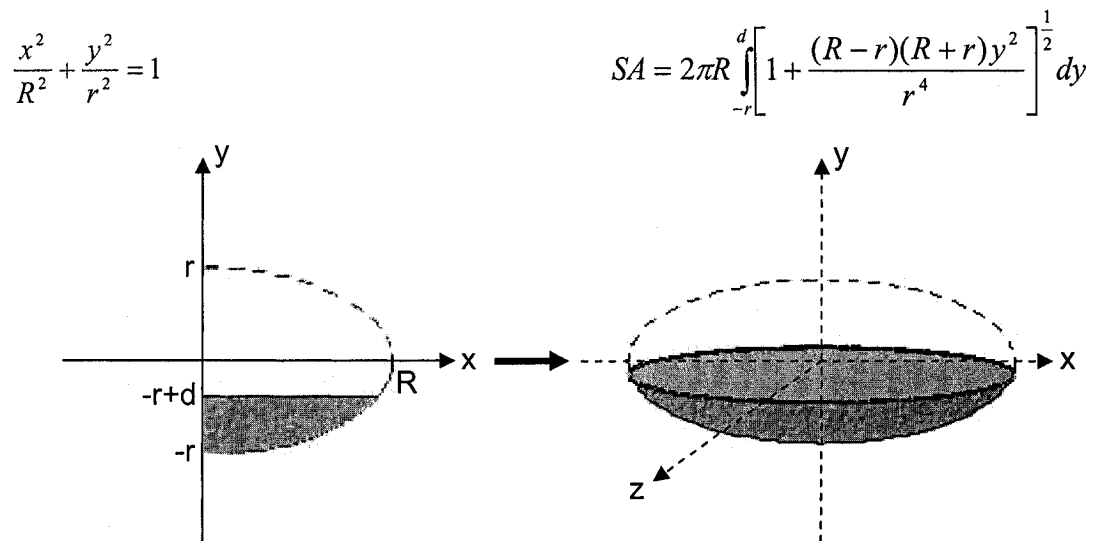


Figure A-13: The surface of revolution (an ellipse, where $R > r$) used to generate an oblate spheroid surface from $-r$ to d (the depth embedded in the quartz substrate).

The surface area of the spheroid in contact with the substrate simplifies to:

$$SA = 2\pi R [A(-r + d) - A(-r)] \quad \text{Equation 6}$$

$$A(y) = \frac{1}{2} y \sqrt{1 + ky^2} + \frac{\ln(\sqrt{k}y + \sqrt{1 + ky^2})}{2\sqrt{k}} \quad \text{Equation 7}$$

$$k = \frac{(R-r)(R+r)}{r^4} \quad \text{Equation 8}$$

The ratio, p_{quartz} , is then the ratio of the surface area in contact with the substrate to the total surface area.

$$p_{\text{quartz}} = \frac{2\pi R[A(-r+d) - A(-r)]}{2\pi R[A(r) - A(-r)]} = \frac{A(-r+d) - A(-r)}{A(r) - A(-r)} \quad \text{Equation 9}$$

For example, for the sample "Au-Quartz 1" studied in Chapter 5, with a major axis of 22 nm, minor axis of 5.75 nm, and embedded 0.9 nm into the substrate, p_{quartz} is calculated as follows.

$$p_{\text{quartz}} = \frac{A(-5.75 + 0.9) - A(-5.75)}{A(5.75) - A(-5.75)} = \frac{441}{3475} = 0.13$$

Appendix 5: Calculation of Extinction for Oblate Spheroids in the Quasistatic Approximation

The following Matlab program was written to calculate and plot the extinction coefficient for oblate metal nanoparticles using the quasistatic approximation to Mie theory. The results of these calculations were used to produce the plots shown in Chapter 5.

5.1 Matlab program for Calculation of Extinction Coefficients of Oblate Gold Spheroids

```
% Computation of Mie Efficiencies for oblate spheroids in the quasistatic
% approximation given complex dielectric function for the gold (epsilon1 and
% epsilon2), the corresponding wavelengths in the UV-VIS range, the real
% component to the refractive index of the medium, and size parameters for
the % major and minor axes.
% see Bohren and Huffman (1983), p. 141.
% Result: extinction coefficient per nanoparticle (kappa),
% Written for Matlab, by Vicki Meli, 25/02/2004.
```

```
clear all
```

```
close all
```

```

R=input('What is the radius of the major axes (nm)?');

Radius=R*10^(-9);    %converts to meters

r=input('What is the minor axis radius (nm)?');

radius=r*10^(-9);

Real_refractive_index_of_medium=input('What is the refractive index of the
medium?');

Epsilonm=Real_refractive_index_of_medium^2;

AR=Radius/radius;    %aspect ratio

Ecc=sqrt(1-AR^(-2));  %Eccentricity

G=((1-Ecc^2)/Ecc^2)^0.5;

N=1;    %Number of spheroids

V=(4/3)*pi*(Radius^2)*radius;  %Volume of spheroid

P1=(G/(2*Ecc^2)) * ((pi/2)-atan(G))-(G^2)/2;    %polarization factors

P2=P1;

P3=1-2*P1;

```

```
lambda=[ ];
```

```
epsilon1=[ ];
```

```
epsilon2=[ ];
```

```
Ext=[ ];
```

```
load lambda.dat
```

```
load epsilon1.dat
```

```
load epsilon2.dat
```

```
for s=1:225
```

```

    S=((epsilon2(s)/P1^2)/((epsilon1(s)
    +
    ((1-
    P1)*Epsilonm/P1))^2+epsilon2(s)^2)) + ((epsilon2(s)/P2^2) / ((epsilon1(s) +
    ((1-P2)*Epsilonm/P2))^2+epsilon2(s)^2)) +((epsilon2(s)/P3^2) / ((epsilon1(s) +
    ((1-P3)*Epsilonm/P3))^2+epsilon2(s)^2));
```

```
    Kappa=(2*pi*N*V*Epsilonm^1.5)/(3*lambda(s))*S;
```

```
    Ext=[Ext, Kappa];
```

```
end
```

```
PEAKMAX=[ ];
```

```
Lambda=lambda'.*10^9;
```

```
[C,l]=max(Ext);  
  
PeakMax = Lambda(l);  
  
PEAKMAX = [PEAKMAX; ' Lambda Max = ' num2str(PeakMax, '%3.1f') ' nm'];  
  
  
plot(Lambda, Ext)  
  
xlabel('Wavelength (nm)')  
  
ylabel('Extinction Coefficient (m^2/particle)')  
  
title(['Extinction of Oblate Au Nanoparticles, ' num2str(R) ' nm x ' num2str(R) '  
nm x ' num2str(r) ' nm'])  
  
legend([PEAKMAX,'n(medium)='  
num2str(Real_refractive_index_of_medium,'%2.3f')]);  
  
hold on  
  
  
  
  
v=axis;  
  
v(1)=400;  
  
axis(v);
```